Investigation of foam generation, propagation and rheology in fractures

Alquaimi, Bander

DOI
10.4233/uuid:9f560388-49fd-48ba-8929-9744f549e1bc

Publication date
2017

Document Version
Final published version

Citation (APA)
Alquaimi, B. (2017). *Investigation of foam generation, propagation and rheology in fractures*. [Dissertation (TU Delft), Delft University of Technology]. https://doi.org/10.4233/uuid:9f560388-49fd-48ba-8929-9744f549e1bc

Important note
To cite this publication, please use the final published version (if applicable).
Please check the document version above.

INVESTIGATION OF FOAM GENERATION, PROPAGATION AND RHEOLOGY IN FRACTURES

INVESTIGATION OF FOAM GENERATION, PROPAGATION AND RHEOLOGY IN FRACTURES

Proefschrift

ter verkrijging van de graad van doctor
aan de Technische Universiteit Delft,
op gezag van de Rector Magnificus prof. ir. K. C. A. M. Luyben,
voorzitter van het College voor Promoties,
in het openbaar te verdedigen op dinsdag 21 november 2017 om 12:00 uur

door

Bander Ibrahim ALQUAIMI

Master of Science in Petroleum and Natural Gas Engineering
West Virginia University, Verenigde Staten
geboren te Riyad, Saoudi-Arabië.

Dit proefschrift is goedgekeurd door de promotor:

Prof. dr. W. R. Rossen

Samenstelling promotiecommissie:

Rector Magnificus,	voorzitter
Prof. dr. W. R. Rossen,	Technische Universiteit Delft, promotor

Onafhankelijke leden:

Prof. dr. M. Ferno,	University of Bergen Norway,
Dr. D. V. Voskov,	Technische Universiteit Delft,
Dr. A. Barnhoorn,	Technische Universiteit Delft,
Prof. dr. H. J. Bertin,	University of Bordeaux France,
Prof. dr. G. Bertotti,	Technische Universiteit Delft,
Prof. dr. ir. P. L. J. Zitha,	Technische Universiteit Delft,

keywords: Capillary number, flow in fractures, capillarity in fractures, fracture desaturation curves, in-situ foam generation, foam in fractures, mobility control in fractures, pre-generated foam flow, foam propagation.

Cover design by Fkrah_Des

Printed by Gildeprint, The Netherlands

ISBN : 978-94-6233-823-4

An electronic version of this dissertation is available at

http://repository.tudelft.nl

To

My lovely mother and father

Haya, Bailasan, Ibrahim and my sisters

CONTENTS

LIST OF FIGURES

LIST OF TABLES

1

INTRODUCTION

1

1.1. NATURALLY FRACTURED RESERVOIRS

A naturally fractured reservoir (NFR) is defined as a reservoir in which naturally occurring fractures either have, or are predicted to have, a significant effect on reservoir fluid flow, either in the form of increased reservoir permeability and/or porosity or increased permeability anisotropy (Nelson, 2001). Aguilera (1995) defined a naturally fractured reservoir as a reservoir which contains fractures created by natural forces. NFRs are found in many countries around the globe, in almost every lithology (Aguilera, 1995; Narr et al., 2006). These reservoirs can be carbonates, sandstone, or shale in the case of unconventional or basement reservoirs (van Golf-Racht, 1982). Montgomery and Morgan (1998) investigated fracture occurrence in both sandstone & carbonate formations. The result shows that fractures exist in both, with a high percentage of fractures in brittle rocks such as wackestone and packstone compared to shale formations.

NFRs have been explored and exploited globally for groundwater, geothermal energy, hydrocarbon production, coalbed methane production, and nuclear waste sequestration (Ramspott et al., 1979; Persoff and Pruess, 1995; Wu, 2015). The Middle East contains approximately 47% of the world's oil reserves (British Petroleum, 2016). Many of these reserves are in naturally fractured carbonate reservoirs (Minne and Gartner, 1979; Cosentino et al., 2001; Phelps and Strauss, 2002). NFRs show a wide range of behaviors because of variations in fracture density, connectivity and extent of the fracture network, and fracture-matrix interaction.

Aguilera (1995) classified NFRs into three types, from the point of view of storativity (types A, B, C). In a reservoir of Type A, there is high storage capacity in the matrix and low storage in the fractures. In a reservoir of Type B, there is approximately equal storage capacity in the matrix and fractures. In a reservoir of Type C, all the storage capacity is in the fractures. Aguilera (1999) presented some estimates of recovery factors from each type. The recovery factor varies considerably depending on the type of the NFR. Nelson (2001) presented another classification of NFRs based on porosity and permeability. The classification includes four types. Type 1: fractures provide essential porosity and permeability. Type 2: fractures provide essential permeability. Type 3: fractures provide a permeability assist. Type 4: fractures create only permeability anisotropy. Each type requires different production and management strategies. There are major differences in the process of primary recovery in the different types, and the best enhanced oil recovery (EOR) strategy would also be type dependent.

Recognizing these reservoirs is a learning process that evolves during the exploration, development and production of the reservoir. Integrating production behavior, drilling observations, geological indications and geophysical data leads to declaring a reservoir to be an NFR (Narr et al., 2006). In a carbonate NFR, for instance, the reservoir is characterized by production anomalies, absence of a transition zone, uniform fluid properties with depth, and high production gas/oil and water/oil ratios (Dominguez, 1992).

1.2. NATURAL FRACTURE

A natural fracture is a macroscopic, quasi-planar discontinuity that results from stresses that exceed the rupture strength of the rock. It is also defined as a mechanical discontinuity or parting caused by brittle failure (Narr et al., 2006). Fractures are generally classified as mode I or mode II, i.e., opening-mode or sheared fractures. Nelson (2001) classified natural fractures based on their scale. Tectonic fractures are larger than other fractures by an order of 9-10. These fractures can be fault-related or fold-related. The second largest in scale are the regional fractures. These fractures show little change in orientation and show no evidence of offset across the fracture plane. The third type is contractional fractures, which are created by tension or extension stresses associated with general-bulk volume reduction throughout the rock. Lastly are the surface-related fractures, which are developed during unloading, release of stored stress and strain. They occur while formations are brought up to the surface of the earth, so they are important for outcrop studies.

To understand the impact of these naturally-occurring fractures on fluid flow, one must characterize these fractures. The fractures are characterized based on their location in the reservoir, azimuth, length and height, dip angle, aperture, density and intensity, and fracture morphology. The fractures are commonly described as open, partially open or closed (filled with minerals) (van Golf-Racht, 1982; Dominguez, 1992; Nelson, 2001; Narr et al., 2006). Fractures also have rough walls and variable apertures, as well as asperities where the two opposing fracture walls are in contact with each other (van Golf-Racht, 1982; Brown, 1987; Odling, 1994; Olsson and Barton, 2001). The roughness scale can be as small as grain size upto much larger scales. Barton and Choubey (1977) proposed an empirical law to predict the shear strength of a rock joint. They defined a parameter called joint roughness coefficient (JRC). The JRC ranges from 0 to 20 from smooth to very-rough rock joints. It is a function of peak shear strength, normal stress, joint compressive strength, and friction angle. Figure 1.1 shows an example of fracture joint roughness. The images are labelled from 1 to 10 from smooth to very rough, respectively (Barton and Choubey, 1977). There is a vast literature on natural fractures and naturally fractured reservoirs. Our purpose is to briefly introduce some of their features which are relevant to our investigation.

1.3. FLUID FLOW IN FRACTURES

Understanding and predicting the entire behavior of NFRs requires understanding the flow in a single fracture (Rossen and Kumar, 1992). The study of single- and multiphase flow in a single fracture started as early as the 1960s. A number of studies over the last four decades have examined fracture relative permeability and capillary pressure. The pioneering study of flow in fractures concluded that fracture relative permeability is a straight-line relationship (Romm, 1966). This is a case-specific relationship that applies if capillary pressure inside the fracture is insignificant compared to gravity and viscous forces. However, when capillarity in a fracture is significant, the relative permeability deviates from linearity. These findings were from mathematical modeling and laboratory experiments (Pruess and Tsang, 1990; Fourar et al., 1992; Rossen and Kumar,

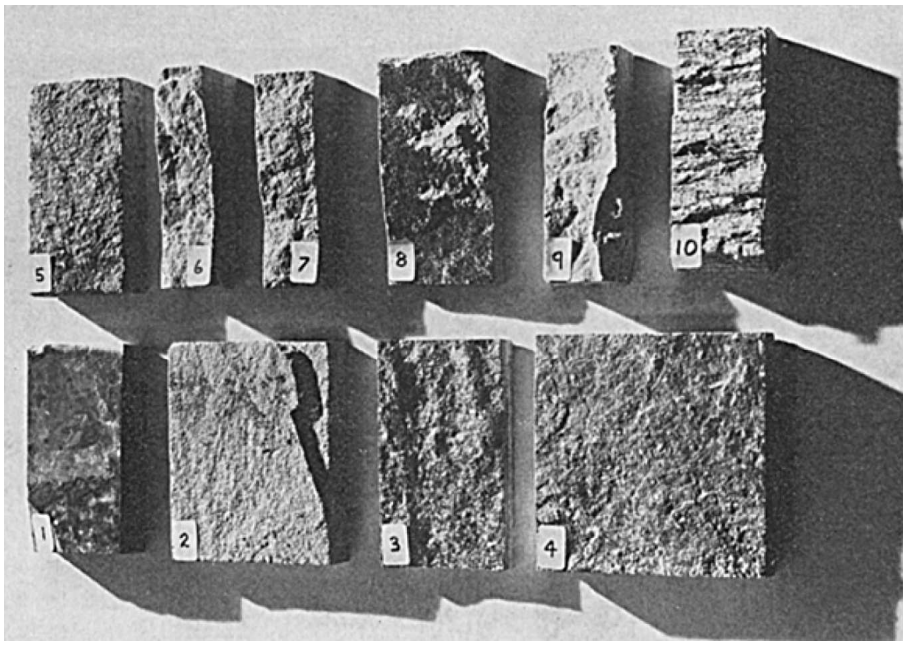

Figure 1.1: Examples of fracture-joint roughness. The images are labelled from 1 to 10 from smooth to very rough, respectively. The figure is from Barton and Choubey (1977).

1992; Pieters and Graves, 1994; Persoff and Pruess, 1995; Maloney and Doggett, 1997; Izadi et al., 2012; Lian and Cheng, 2012). The fracture relative-permeability experiments were performed on Hele-Shaw cells, parallel glass plates and fractured cores (Pieters and Graves, 1994; Persoff and Pruess, 1995; Lian and Cheng, 2012).

Capillarity in a fracture is dependent on aperture variation, interfacial tension and contact angle (Pruess and Tsang, 1990). Aperture variation is a function of the roughness scale of the fracture. Therefore, a fracture can be represented as a two-dimensional network of locations of wide and narrow apertures (Tsang, 1984; Brown and Scholz, 1985; Wang and Narasimhan, 1985; Brown et al., 1986; Schrauf and Evans, 1986; Pyrak-Nolte et al., 1988; Morrow et al., 1990; Rossen and Kumar, 1992; Odling and Roden, 1997; Hughes and Blunt, 2001). Thus, fractures can be considered as 2D analogs of the 3D networks of throats and bodies that compose the pore network of rock matrix (Rossen and Kumar, 1992; Hughes and Blunt, 2001) .

1.4. GAS INJECTION IN NFRS

A statistical review of the overall ultimate recoveries of 100 NFRs indicates that the recovery of NFRs is somewhat lower than those of many conventional reservoirs (Allan and Sun, 2003). Because fracture conductivity is much larger than matrix permeability, fractures act as channels for rapid water or gas breakthrough, leading to poor volumetric sweep efficiency (Schechter et al., 1996). Thus, considerable oil reserves are not recov-

ered because of the nature of these reservoirs, which is a strong motivation for considering EOR.

Gas is injected, as an EOR method, in petroleum reservoirs to achieve an incremental increase in recovery (Pope, 1980; Kantzas et al., 1988; Malik and Islam, 2000; Rao, 2001; Sheng, 2015). The process of gas injection is implemented to reduce residual oil saturation, reduce oil viscosity, swell oil volume, or improve oil recovery by gravity drainage (Rodríguez et al., 2001; Tiwari and Kumar, 2001; Sanchez Bujanos et al., 2005; Kalra and Wu, 2014). The gas-injection process involves the immiscible or miscible injection of carbon dioxide, hydrocarbon and nitrogen gases. As of 2010, worldwide gas-injection projects represent 40.8 % of overall EOR projects. 86 % of these gas-injection projects are immiscible injections (see Figure 1.2) (Al Adasani and Bai, 2011).

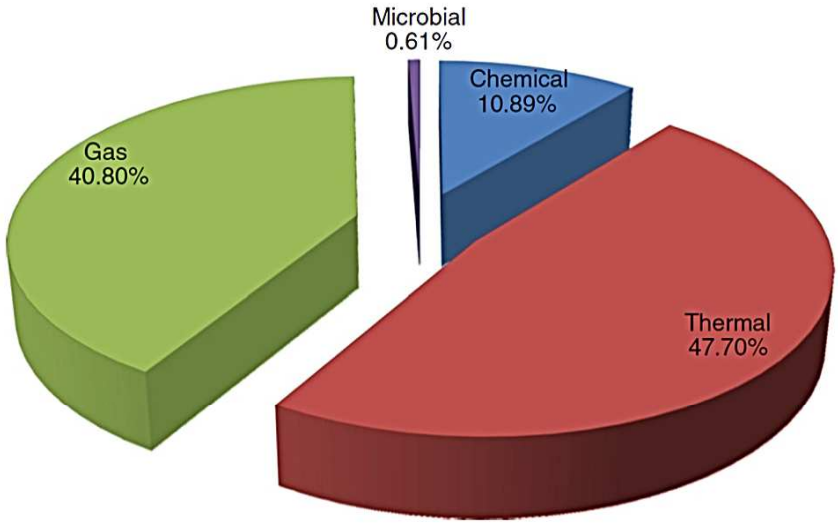

Figure 1.2: 2010 worldwide EOR project categories. The gas injection category represents 40.8 %, which is the second largest after thermal. The figure is from Al Adasani and Bai (2011) who adapted the data from many sources.

A review of all North Sea EOR projects shows that 95% of the projects from 1975 to 2006 involved gas injection (Awan et al., 2006). The first gas injection in the North Sea started using hydrocarbon gas injection in 1975 (Jakobsson and Christian, 1994; Hermansen et al., 1997). Gas can have good microscopic displacement efficiency; however, the process at the reservoir scale suffers from gravity override, viscous instability and worsened channelling, due to the density and viscosity differences of gas compared to in-situ fluids (Lake et al., 1986). Different injection methods have been used to mitigate these challenges, including water alternating gas (WAG), simultaneous WAG, and foam

1

assisted WAG, often called surfactant alternating gas (SAG). WAG injection is a major EOR method implemented in the North Sea (Awan et al., 2006).

1.5. FOAM INJECTION

Foam is a dispersion of gas in water, stabilized by surfactants (Lake et al., 1986). The gas bubbles are separated by thin liquid films called lamellae (Bikerman, 2013). A strong foam is one that has small bubbles, and therfore many lamellae separating gas bubbles, and a low mobility. A weak foam has larger bubbles, fewer lamellae and higher mobility. Foam is also described by its texture. Fine-textured foams have very small bubbles and coarse-textured foam has large bubbles. Foam greatly reduces gas mobility for gas EOR projects. It substantially increases both the effective viscosity of gas and gas trapping. As foam viscosity increases, the viscous resistance to flow in the fracture increases, leading to a flow of gas into the matrix and hence enhancing the recovery of oil (Haugen et al., 2014).

Foam for EOR was first proposed by Bond and Holbrook (1958). There have been many studies and some field trials to understand foam flow in porous media since 1958 (Fried, 1961; Bernard and Holm, 1964; Raza and Marsden, 1965; Kamal and Marsden Jr, 1973; Bernard et al., 1980; Hirasaki and Lawson, 1985; Khatib et al., 1988; Osterloh and Jante, 1992; Rossen, 1996). Foam is injected into porous media for in-depth gas-mobility control, blocking and diversion, and to control the gas-oil ratio. Turta and Singhal (2002) provided a thorough review of foam field-application tests. Eson and Cooke (1989) provided a review of steam foam field applications. Friedmann et al. (1997) reported a successful foam injection in NFRs in the Rangely Weber Sand Unit to reduce excessive CO_2 breakthrough through fractures. They used gelled foam to stabilize the lamellae and be able to reduce flow through the fractures. Ocampo-Florez et al. (2014) reported another field-pilot test in the NFR of the Cupiagua field, where gas recycling was significantly reduced in the field because of foam injection.

Significant progress has been achieved in understanding foam flow in porous media in the absence of natural fractures. However, the knowledge about foam flow in fractures is far less complete. The following is a literature review on foam flow in single or multiple fractures.

Kovscek et al. (1995) investigated nitrogen, water and aqueous foam flow through two transparent replicas of natural rough-walled rock fractures with hydraulic apertures of roughly 30 μm and 100 μm, respectively. Radial-flow tests were done on these fractures, with an outer radius of 12 cm. The total flow rate of nitrogen ranged from 1-100 standard cm^3/min, which is equivalent to 0.0014-0.147 m/s at the outer radius. The pressure drop was recorded across the whole sample. Foam reduced gas mobility in the model fracture by a factor of 100-540 over a range of foam qualities from 60 to 99%. In-situ foam generation was reported and described in terms of a capillary snap-off mechanism similar to that in matrix porous media.

Yan et al. (2006) experimentally investigated foam sweep efficiency, using pre-generated

foam, in model fractures that were either single or parallel double (side-by-side) smooth slits. The slit consisted of two parallel glass plates, where the gap in between represents the aperture and the gasket thickness between the plates sets the aperture of the fracture. The apertures were 100, 200 and 300 μm for the single slit and a combination of 100/200 or 50/150 μm for the double slit. The double-slit model fracture was created by adding another thin glass sheet in between to create a narrower part of the slit. The total superficial velocities ranged from 0.001 to 0.20 m/s and the foam qualities ranged from 0.0 to 90%. Yan et al. concluded that pre-generated foam can greatly improve the sweep efficiency in the double-slit fracture system.

Skoreyko et al. (2011) developed a new foam model from laboratory and field data for a fractured reservoir. High- and low-permeability fractures were created in 12-cm-long core samples of 2.0 md Indiana limestone. Each core was sawn into two halves, from inlet to outlet, and artificial vugs were drilled on both sides of the fracture surface. The high-permeability fracture was created by increasing the number of vugs, with some vugs overlapping. The fracture aperture was 1340 μm, set by placement of metal balls between rock faces. Surfactant solution and gas were co-injected into these fractured samples. The total superficial velocities ranged from 1.7×10^{-4} to 5.1×10^{-4} m/s with foam qualities of 25, 50 and 75%. The authors developed a model to match laboratory core-flood data and the field-pilot tests. The study did not observe foam generation directly but reported an increase in pressure drop indicating foam generation.

Haugen et al. (2012) conducted laboratory experiments using foam to reduce fracture transmissivity and improve the matrix sweep in fractured, low-permeability, oil-wet limestone rock. The experiments were done on 8.0-cm-long core plugs sawn, from inlet to outlet, by a circular saw and on a 14-cm-long fracture network cut using a band saw on a rectangular block. The fracture was held open by a 1000-μm spacer. The sawn core plug was confined in a core holder. The sawn block was coated with epoxy resin on four sides of the block and two opposing sides were used to fit fluid inlet and outlet ports. The injected foam qualities used were 90 and 92%. The total superficial velocities were around 1.0×10^{-4} and 4.2×10^{-4} m/s for the core and the block, respectively. Both pre- and in-situ-generated foams were tested. The results of the laboratory experiments showed an increase in oil recovery for the pre-generated foam, while no foam generation was observed in the cores or blocks of smooth-walled fractures and hence no incremental oil was gained if foam was not pre-generated.

Buchgraber et al. (2012) experimentally investigated the behavior of pre-generated foam flow in micromodels at various foam qualities and fluid velocities. The experiments were conducted in channels etched on 2×5 cm silicon chips. The first experiment used parallel smooth channels with apertures of 40 and 30 μm. The second experiment was conducted by injecting foam into a medium comprising smooth, adjacent square regions with apertures of 20 and 40 μm arranged in a checkerboard pattern. The third experiment was done on a uniform-aperture channel with a rough face. The gas superficial velocity ranged from 7.23×10^{-6} to 0.0057 m/s and the liquid superficial velocity ranged from 2.89×10^{-5} to 0.0017 m/s. Buchgraber et al. concluded that foam reduced gas mobil-

ity in these idealized uniform-aperture fractures, where foam was pre-generated. Foam generation by snap-off was observed at the step changes between 20- and 40-μm apertures.

Haugen et al. (2014) experimentally studied supercritical CO_2, pre-generated CO_2-foam, and N_2-foam injections in fractured samples. The goal of the study was to investigate the effect of pre-generated foam on oil recovery by reducing the flow through the fracture and thereby diverting flow to the matrix. The study used 13 core plugs, which were cut along the core length using a diamond-coated circular saw. The permeability of the fractured cores ranged from 319 to 2020 md. The fractured core plugs, with different fracture permeabilities, were reassembled and placed in a core holder with overburden pressure. Foam was injected into the fractured core plugs. A constant foam quality of 90% was used in most of the tests. The results showed that gas and surfactant contributed to oil recovery during CO_2-foam injection under oil-wet conditions, compared to pure CO_2. The study did not investigate in-situ foam generation.

Steinsbø et al. (2015) extended the study of Haugen et al. (2014). Miscible CO_2 and CO_2-foam laboratory tests were performed to study enhanced oil recovery in fractured core samples. In this study, the cores were fractured using a band saw, which creates relatively smooth fractures. The cores were assembled using spacers between the core halves to maintain the fractures open at a uniform fracture aperture of 1000 μm. The tests were conducted on two cores. In the first, a fracture ran from inlet to outlet. The second core was assembled from three sections with a break between each. The first 2-cm inlet section is unfractured and ends in a fracture across the core, perpendicular to flow. This section, in effect, acts as a foam generator for fractures downstream. The second, 4-cm-long section, had a vertically oriented fracture. The last 4 cm of the core had a horizontally oriented fracture. The three sections were assembled in a hassler core holder. Foam was pre-generated in all these tests using a sand-pack or the unfractured section of the core. The total superficial velocities used were 3.34×10^{-5}, 0.0003, and 0.0006 m/s. The tested foam qualities were 80 and 90%. Steinsbø et al. concluded that foam increased the oil production rate and final recovery in all the experiments due to the increase in viscosity in the fracture, leading to more CO_2 invasion into the matrix.

Gauteplass et al. (2015) experimentally studied foam generation in 5×5 cm micromodels with an etching depth of 25 μm. The micromodel had upstream and downstream distribution channels which were considered as fractures because of their permeability contrast with the etched part of the model. Foam was pre-generated using sandstone or a metallic sieve in all the experiments. The total superficial velocity used was approximately 0.0009 m/s and foam quality ranged from 75 to 95%. Foam texture changes by snap-off were observed at the permeability discontinuities between the distribution channel and the etched part of the model (i.e., going abruptly from a wide to a narrow aperture). They concluded that foam becomes finer as it flows across a permeability contrast.

Fernø et al. (2016) experimentally investigated the generation of foam within a heteroge-

neous rock slab 31.2 cm long. A ball-peen hammer was used to fracture a marble block which was then reassembled in a frame. The fracture aperture of the network was estimated to be 100-150 μm. The pressure drop was measured across the whole sample. The tested foam qualities ranged from 60 to 95%. The total superficial velocities used were 0.0003, 0.001, 0.0017 and 0.0028 m/s. The study found foam generation by snap-off as gas flowed from fractures into vugs. Ferno et al. concluded that foam significantly improved the sweep of the fractures and delayed gas breakthrough compared with pure gas injection. A shear-thinning behavior was observed during coinjection of gas and surfactant solution over the tested range of foam qualities.

Most of these studies discuss the behavior and benefits of pre-generated foam in a fracture. Only two studies address foam generation, in a 12-cm-diameter disk-shaped fracture and 31.2-cm-long fracture with some vugs (Kovscek et al., 1995; Fernø et al., 2016). In these tests, the pressure drop was measured across the whole sample with little information about pressure gradient or foam texture as a function of position.

1.6. SCOPE OF THE DISSERTATION

Foam is not a single phase but rather two phases flowing simultaneously. During two-phase flow, there is a competition between the viscous and capillary forces. This competition results in the trapping of gas; therefore, we proposed and experimentally validated a new capillary number for trapping and mobilization of the nonweting phase in fractures. The goal is to define fracture geometrical parameters that are responsible for the trapping of the nonwetting phase. We investigated in-situ foam generation in a variety of fractures. Fractures encountered in NFRs are different in their magnitude of aperture, aperture variation and the length scale over which the aperture varies. Once foam is generated, we investigated foam propagation and the rate of generation/destruction of foam lamellae. This is crucial for successful foam projects, since fractures at a reservoir scale can extend to hundreds of meters and span the whole reservoir thickness. We systematically varied the aperture to study its impact on in-situ foam generation and propagation. Similarly, we investigated the effect of fracture wall roughness on foam properties. We record pressure gradient throughout the whole fracture to track foam generation. We use image analysis to compare foam texture with pressure gradient. We study foam rheology over ranges of gas fractional flow and total superficial velocities.

We designed an experimental research program to achieve our research objectives. First, we investigated several methods of representing natural fractures in the laboratory to conduct flow experiments. The first option was to saw the core, from inlet to outlet, and to put the two halves together, with a spacer in between, in a core holder (Skoreyko et al., 2011; Haugen et al., 2012; Izadi et al., 2012; Skoreyko et al., 2012; Haugen et al., 2014; Steinsbø et al., 2015). We eliminated this option because a band saw creates a relatively smooth fracture (Figure 1.3). One cannot observe foam generation mechanisms and foam texture in rock. Silicon micromodels are used as an approximation to flow in fractures (Buchgraber et al., 2012; Gauteplass et al., 2015). However, they are limited in size and often feature abrupt changes in otherwise relatively smooth faces. Figure 1.4 shows a 5×3 cm micromodel. This option is not attractive for our purposes because it

has a limited size, roughness scale and a lack of inner pressure measurements.

A third option is to design fracture apparatus made of glass plates. Model fractures made of glass plates have been used to study foam and two-phase flow in fractures (Pruess and Tsang, 1990; Fourar et al., 1992; Pieters and Graves, 1994; Chen et al., 2004a,b; Yan et al., 2006; Qian et al., 2011). We decided to design and fabricate model fractures from glass plates because they suit the following design criteria:

- Provide visual ability to monitor foam generation and foam texture.
- Have a large size, to check foam propagation and stability over a significant distance.
- Provide the ability to fabricate a different roughness scale on the glass surface.
- Provide several pressure measurements along the fracture to relate texture to pressure gradient.
- Provide water-wetting surfaces.
- Provide the ability to include a distribution channel for gas and liquid to collect before they enter the fracture.

We have selected five distinctive roughened-glass samples to perform our research. The roughness scale varies significantly among the sample both laterally and vertically as discussed later in this dissertation.

1.7. THESIS OUTLINE

This dissertation contains several articles which are either published or have been submitted for publication in peer-reviewed journals. Below is an executive summary of the chapters included in this dissertation.

1.7.1. CHAPTER 2: CAPILLARY DESATURATION CURVE FOR RESIDUAL NONWETTING PHASE IN NATURAL FRACTURES

In this chapter, we propose a new capillary number for flow in fractures starting with a force balance on a trapped ganglion in a fracture. The new definition is validated with laboratory experiments using five distinctive model fractures. Capillary desaturation curves (CDCs) were generated experimentally using water-air forced imbibition. The residual saturation-capillary number relationship obtained from different fractures, which vary in aperture and roughness, can be represented approximately by a single curve in terms of the new definition of the capillary number. They do not fit a single trend using the conventional definition of the capillary number.

1.7.2. CHAPTER 3: STUDY OF FOAM GENERATION AND PROPAGATION IN A FULLY CHARACTERIZED PHYSICAL-MODEL FRACTURE

This chapter focuses on contributing to the understanding of foam generation and propagation in a fracture. We investigate foam-generation mechanisms and the propagation

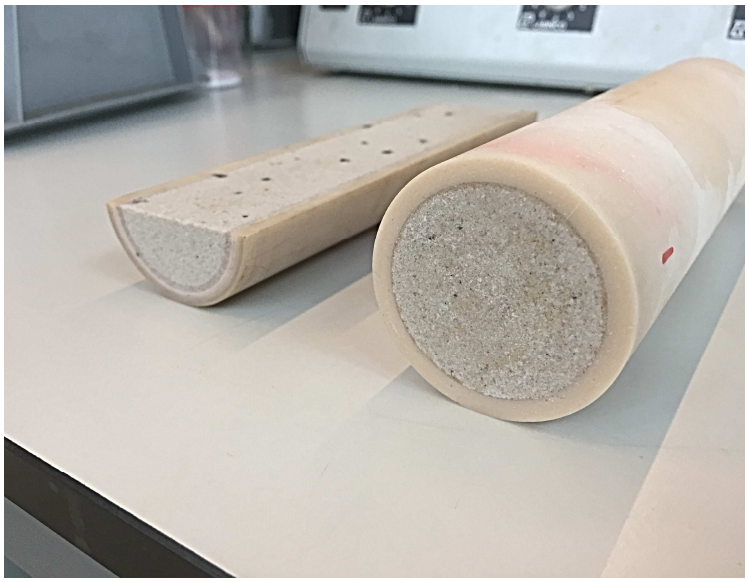

Figure 1.3: A core sawed using a band saw which creates a uniform and relatively smooth fracture surface. This option was eliminated because the fracture surface is relatively smooth, and because foam texture and foam generation mechanisms cannot be observed in rock.

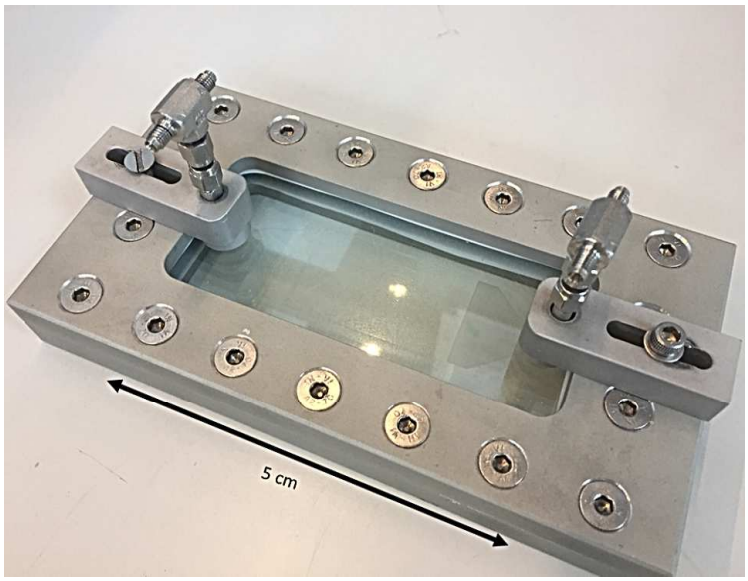

Figure 1.4: A micromodel system for visually monitoring the flow. This option is not attractive for our purposes because it is of limited size, roughness scale and has no inner pressure measurments.

of pre-generated foam. Gas mobility was greatly reduced as a result of in-situ foam generation. Foam was generated predominantly by capillary snap-off and lamella division. Fracture wall roughness played an important role in foam generation. In the case of pre-generated foam, two very distinct bubble sizes were injected: fine-textured bubbles much smaller than the roughness scale and coarse-textured foam with bubbles much larger than the roughness scale. The first case did not show any significant change in bubble size as foam propagated through the model fracture, while in the second case the fracture played a role in reducing bubble size.

1.7.3. CHAPTER 4: CHARACTERIZING FOAM FLOW IN FRACTURES FOR ENHANCED OIL RECOVERY

In this chapter, we study foam rheology in a single fracture. This investigation is conducted by varying superficial velocities of gas and surfactant solution. We find in this model fracture the same two foam-flow regimes central to the understanding of foam in nonfractured porous media: a low-quality regime where pressure gradient is independent of liquid velocity and a high-quality regime where pressure gradient is independent of gas velocity. However, the mechanisms thought to be behind the two flow regimes in nonfractured porous media do not appear in our model fracture. Foam is not at the limit of stability in the high-quality regime. Mobility in the high-quality regime instead reflects reduced and fluctuating foam generation at high foam quality.

1.7.4. CHAPTER 5: FOAM GENERATION AND RHEOLOGY IN A VARIETY OF PHYSICAL MODEL FRACTURES

This chapter aims towards investigating foam-generation mechanisms in five fully characterized fractures with different apertures and correlation lengths of the apertures. We study the rheology of the in-situ generated foam by varying superficial velocities of gas and surfactant solution. We compare the measured pressure gradient against the fracture attributes, aperture and roughness scale. We also compare foam texture as a function of position as the generated foam propagates through the fracture. The determined mobility reduction depends on fracture attributes. Fracture wall roughness plays an important role in foam generation and hence the mobility reduction.

Note from the author: This dissertation includes published papers in peer-reviewed journals and scientific conferences. Consequently, the reader may find similar texts and sentences in some parts of the dissertation.

2

CAPILLARY DESATURATION CURVE FOR THE RESIDUAL NONWETTING PHASE IN NATURAL FRACTURES

THE displacement of the nonwetting phase by a wetting phase is characterized by the capillary number. Different forms of capillary number have been used in the literature for flow in porous media. A capillary number for a single rock fracture has been defined in the literature using the mean aperture to characterize the trapping and mobilization in a fracture. We propose a new capillary-number definition for fractures that incorporates geometrical characterization of the fracture, based on a force balance on a trapped ganglion. The new definition is validated with laboratory experiments using five distinctive model fractures. The model fractures are made of glass plates, with a wide variety of hydraulic apertures, degrees of roughness and correlation lengths of the roughness. The fracture surfaces were characterized in detail and statistically analyzed. The aperture distribution of each model fracture was represented as a two-dimensional network of pore bodies connected by throats. The hydraulic aperture of each model fracture was measured experimentally. Capillary desaturation curves (CDCs) were generated experimentally using water-air in forced imbibition. The transparent nature of the system permits us to determine the residual air saturation as a function of pressure gradient from the captured images. The residual nonwetting saturation-capillary number relationship obtained from different fractures varying in aperture and roughness can be represented approximately by a single curve in terms of the new definition of the capillary number. They do not fit a single trend using the conventional definition of the capillary number.

This chapter is based on, (1) AlQuaimi, B. I., and Rossen, W. R. (2017), New capillary number definition for displacement of residual nonwetting phase in natural fractures, Geophys. Res. Lett., 44, doi:10.1002/2017GL073211. (2) AlQuaimi, B. I., and Rossen, W. R. (2017). Capillary Desaturation Curve for the Residual Nonwetting Phase in Natural Fractures. Accepted for publication in the SPE Journal.

2.1. INTRODUCTION

2.1.1. NATURAL FRACTURES

Most underground reservoirs have some degree of fracturing caused by different earth stresses. Natural fractures can be present in almost every lithology, with different characteristics in terms of their conductivity, storage capacity and the degree of wall roughness (van Golf-Racht, 1982). The reservoir is considered a Naturally Fractured Reservoir (NFR) if fractures are predicted to have a significant impact on reservoir fluid flow dynamics (Nelson, 2001). NFRs have been explored and exploited globally for geothermal energy, petroleum production, coalbed methane production, and nuclear waste sequestration (Ramspott et al., 1979; Persoff and Pruess, 1995). Understanding and predicting the entire behavior of NFRs requires understanding the flow in a single fracture (Rossen and Kumar, 1992). A single fracture has rough walls and a variable aperture, as well as asperities where the two opposing fracture walls are in contact with each other (Olsson and Barton, 2001). Therefore, it can be represented as a two-dimensional network of locations of wide and narrow apertures (Tsang, 1984; Brown and Scholz, 1985; Wang and Narasimhan, 1985; Brown et al., 1986; Schrauf and Evans, 1986; Pyrak-Nolte et al., 1988; Morrow et al., 1990; Rossen and Kumar, 1992; Odling and Roden, 1997; Hughes and Blunt, 2001). Thus, fractures can be considered as 2D analogs of the 3D networks of throats and bodies that compose the pore network of rock matrix (Rossen and Kumar, 1992; Hughes and Blunt, 2001). During the two-phase flow in a fracture, there is a similar competition between the viscous and capillary forces as in a rock matrix, which can be represented by a capillary number. However, the capillary number in the rock is not adequate to describe the mobilization of the nonwetting phase in fractures, as is shown in this chapter.

2.1.2. ROCK MATRIX CAPILLARY NUMBER

In two-phase immiscible displacement, the competition or interplay between the viscous forces and capillary forces determines the mobilization of the trapped nonwetting phase. The capillary number was first described based on the results of several flooding experiments by Moore and Slobod (1955) in a variety of porous media. The relationship was called the Viscap concept (Equation (2.1)); the term Viscap stands for viscosity and capillary pressure:

$$N_{ca} \equiv \frac{v\mu}{\gamma \cos\theta} \tag{2.1}$$

where v is the superficial velocity, μ is the viscosity of the displacing fluid,γ is the interfacial tension, and θ is the contact angle. Another form of the capillary number uses the permeability of the matrix (Reed and Healy, 1977):

$$N_{ca} \equiv \frac{k|\nabla P|}{\gamma \cos\theta} \tag{2.2}$$

where k is permeability, $|\nabla P|$ is the magnitude of the pressure gradient, θ is the contact angle, and γ is the interfacial tension. One can derive Equation (2.2) from a force balance on a trapped nonwetting ganglion, assuming that pore-throat radius and pore length each scale with the square root of permeability (Sheng, 2010). This assumption is

reasonable for geometrically similar porous media like packings of beads or sand. A historical review of different forms of capillary number is presented by Taber (1981). Many of these expressions of the capillary number are equivalent (Chatzis and Morrow, 1984). The major difference between different forms of capillary number is that some include the porosity and others include relative permeability.

2.2. FRACTURE CAPILLARY NUMBER

A number of studies over the last four decades have examined fracture relative permeability and capillary pressure. The pioneering study of flow in fractures concluded that fracture relative permeability is a straight-line relationship (Romm, 1966). This is a case-specific relationship that applies if capillary pressure inside the fracture is insignificant compared to gravity and viscous forces. However, when capillarity in a fracture is significant, the relative permeability deviates from linearity (Pruess and Tsang, 1990; Fourar et al., 1992; Rossen and Kumar, 1992; Maloney and Doggett, 1997; Pieters and Graves, 1994; Izadi et al., 2012). If gravity and viscous forces are not dominant, the capillary number describes the mobilization of the nonwetting phase. Hughes and Blunt (2001) studied multiphase flow in a single fracture using a pore-network model. They generated a model of the fracture from published aperture data, and the capillary number for this model was defined as

$$N_{ca} \equiv \frac{Q\mu_w}{\overline{d}bN_y\gamma} \tag{2.3}$$

where Q is the volumetric flow rate, μ_w is the displacing fluid viscosity (water in this case), $\overline{d}$ is the mean aperture, b is the resolution (width of the pixels), N_y is the number of pixels perpendicular to flow across the fracture, and γ is the interfacial tension. (We have changed their nomenclature for consistency with our derivation below.) This definition is obtained from Equation (2.1) by replacing the superficial (Darcy) velocity with the volumetric flow rate Q divided by cross-sectional area ($\overline{d}bNy$). The derivation of the capillary number for rock from a force balance on a trapped ganglion assumes that permeability scales with the product of pore-throat radius and pore-body length. This assumption is questionable for fractures, where fracture permeability could be the same for a slit with smooth walls and no trapping and for a fracture with large variations in aperture and significant trapping.

We present a derivation of the capillary number for a fracture based on force balance on a trapped nonwetting ganglion. The variation of aperture d is the geometric parameter that is responsible for trapping nonwetting phase in the fracture. Capillary pressure across a curved interface where the aperture is d is

$$P_c = \frac{2\gamma\cos\theta}{d} \tag{2.4}$$

Equation (2.4) assumes that the length scale along which aperture varies in the fracture plane is much greater than the aperture itself; thus interfaces are nearly cylindrical rather than spherical. We provide justification below. The principle radii of curvature of the interface between the wetting and nonwetting phases are thus $r_1 = d\,cos\,\theta/2$ and $r_2 \cong \infty$

(Pruess and Tsang, 1990). Consider a fracture with some degree of roughness where a trapped ganglion is on the verge of forward displacement, as shown in the schematic of Figure 2.1. Figure 2.1 shows the flow direction and the characteristic pore-throat and

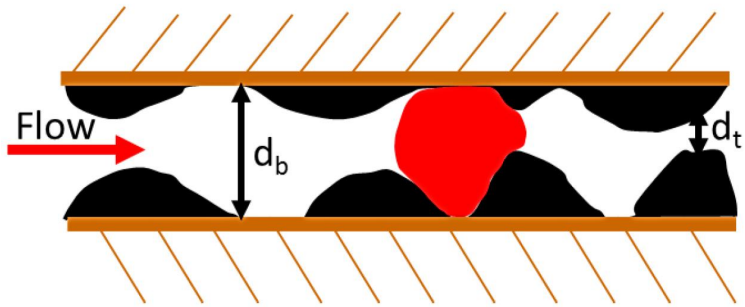

Figure 2.1: Schematic of a rough fracture with a trapped ganglion. The aperture of the fracture is greatly exaggerated in this figure compared to the distance along the fracture.

pore-body apertures. The aperture is exaggerated in this figure. As noted, the curvature across the fracture is much greater than that along the fracture; therefore the maximum capillary pressure during the passage through the throat can be written as

$$P_c = \frac{2\gamma\cos\theta}{d_t} \tag{2.5}$$

where d_t is the minimum aperture i.e. aperture at the throat. The capillary-pressure difference across the interfaces of a ganglion, with its leading edge penetrating a throat and its trailing edge in a pore body, is given by

$$\Delta P_c = \left(\frac{2\gamma}{d_t} - \frac{2\gamma}{d_b}\right)\cos\theta \tag{2.6}$$

where d_b is the aperture at the body. The pressure difference across the ganglion, of length of L_g, must be greater than this pressure difference if the ganglion is to be mobilized:

$$\nabla P L_g > \left(\frac{2\gamma}{d_t} - \frac{2\gamma}{d_b}\right)\cos\theta = \frac{2\gamma}{d_t}\left(1 - \left(\frac{d_t}{d_b}\right)\right)\cos\theta \tag{2.7}$$

One can regroup terms in Equation (2.7) to restate the criterion for mobilization in terms of a dimensionless capillary number:

$$\frac{\nabla P L_g d_t}{2\gamma\left(1 - \left(\frac{d_t}{d_b}\right)\right)\cos\theta} \equiv N_{ca} > 1 \tag{2.8}$$

The permeability of a fracture, approximated as a smooth rectangular slit, can also be written as a function of the hydraulic aperture (van Golf-Racht, 1982; Tsang, 1992; Zimmerman and Bodvarsson, 1996):

$$Q = \frac{1}{12}\frac{|\nabla P|\, w {d_H}^3}{\mu}; \quad k_f \equiv \frac{{d_H}^2}{12} \tag{2.9}$$

where Q is the volumetric flow rate, $|\nabla P|$ the magnitude of pressure gradient, w is the width perpendicular to flow, μ is the viscosity and d_H is the hydraulic aperture. Equation (2.9) is in effect a definition of the hydraulic aperture d_H. Introducing permeability k_f into Equation (2.8), and noting its relation to d_H, yields

$$\frac{L_g d_t}{1-\left(\frac{d_t}{d_b}\right)\cos\theta} \equiv (d_H)^2 \left(\frac{d_t}{d_H}\right)\left(\frac{L_g}{d_t}\right)\left(\frac{d_t}{d_H}\right)\frac{1}{1-\left(\frac{d_t}{d_b}\right)\cos\theta} \tag{2.10}$$

$$N_{ca} \equiv \left(\frac{\nabla P k_f}{\gamma\cos\theta}\right)\left[\left(\frac{12}{2}\right)\left(\frac{d_t}{d_H}\right)^2\left(\frac{L_g}{d_t}\right)\frac{1}{1-\left(\frac{d_t}{d_b}\right)}\right] \tag{2.11}$$

The first part of this definition of the capillary number is identical to Equation (2.2), i.e. that traditionally used for porous media. The second part accounts for the effect of fracture roughness: the narrowness of the "throats," the distance between throats, and the contrast in aperture between pore throats and bodies. The term in brackets is a geometric factor; Yeganeh et al. (2016) identified a similar factor in the capillary number for rock matrix. To be useful, the terms in this definition must be derivable from a consideration of the fracture itself, without, for instance, needing to conduct a two-phase flow experiment (Tsang, 1984; Brown and Scholz, 1985; Wang and Narasimhan, 1985; Brown et al., 1986; Schrauf and Evans, 1986; Pyrak-Nolte et al., 1988; Morrow et al., 1990; Johns et al., 1993; Hakami and Larsson, 1996; Odling and Roden, 1997; Oron and Berkowitz, 1998; Hughes and Blunt, 2001; Karpyn et al., 2007; Lang et al., 2015, 2016). We describe how to derive these parameters in the next section.

2.3. DESIGN OF MODEL FRACTURE

Five different physical-model fractures were designed for capillary-desaturation experiments to test the new expression for the capillary number. In the literature, different experimental approaches are presented, including splitting the core into two halves, which are then re-assembled with a spacer in between (Haugen et al., 2012; Skoreyko et al., 2012). However, one cannot directly observe the flow inside a rock sample. Microfluidic devices are used to represent flow in fractures (Buchgraber et al., 2012; Gauteplass et al., 2015). Microfluidic devices have distinct, usually rectangular, channels, which do not represent an aperture that varies continuous over space. A third option is to design a fracture apparatus made of glass plates. Model fractures based on glass plates have been used to study flow in fractures (Fourar et al., 1992; Pieters and Graves, 1994; Chen et al., 2004a,b; Yan et al., 2006; Qian et al., 2011). The transparent nature of the glass provides the ability to observe the flow and to determine the saturation during the experiment. The variety of commercially available roughened glass makes it possible to test a wide range of types and scales of roughness. Therefore, we designed five different model fractures using glass plates fabricated in collaboration with Trace Elemental Instruments (Delft, The Netherlands).

The size of the fractures are 30×10 cm and each consists of a roughened plate that represents fracture wall roughness and a top plate that is smooth, to allow direct observation

of the flow and measurement of saturation. Here, as in other studies (Pieters and Graves, 1994; Chen et al., 2004a,b), area fraction is used as an approximation to fracture saturation. Five different roughened-glass samples were selected for this study, with a wide variety of degrees of roughness. Each roughened plate includes four ports, two to measure the pressure difference and two as flow inlet and outlet. The gap between the top plate and the rough surface represents the fracture aperture. The two glass plates are glued together using Araldite® 2014 (Polyestershoppen B.V., Moordrecht, The Netherlands) which is a two-component epoxy adhesive that has a tensile strength of 26 MPa at 23 °C. The glue was found not to have any adverse effect on interfacial tension. The plates are mounted using two wooden bars to hold the plates firmly and prevent the glass from bowing outwards during the flow.

2.3.1. GEOMETRIC CHARACTERIZATION OF MODEL FRACTURES

The five roughened glass samples were profiled to quantify the spatial and vertical variation in the height of the surface of each sample. The Chromatic Profiler (Precitec Optronik GmbH, Philips Innovation Services, Eindhoven, The Netherlands) has a height resolution of 0.5 µm and scanning window of 50×50 µm. The device uses a lens system with chromatic aberration, and reflected color is a measure for height. A randomly selected patch of area of 4.0×4.0 cm was used for the measurement. Light scattering makes it impossible for the optical profilers to determine the height at some locations. It accurately captures height at positions with relatively shallow small slopes, but not at positions with a very steep slope. Fortunately, the regions captured include the maxima, minima and saddle points in height, i.e., the most significant locations for our purposes. The instrument restores the missing data using spline interpolation. We limited the restoring algorithm to 5 iterations to avoid creating spurious maxima and minima in our measurements. We scanned two separate 4.0×4.0 cm patches in the same sample to confirm that we had obtained a representative measurement for the whole surface. Figure 2.2 shows the results of the two areas measured in Sample 1.

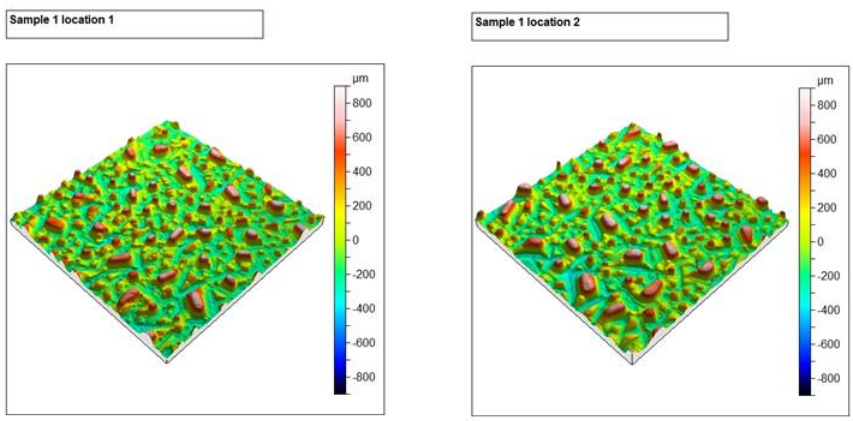

Figure 2.2: Chromatic Profiler height data. The left image shows patch 1 and the right image shows patch 2.

Additionally, the descriptive statistics of each patch were calculated along with the height values obtained from the Chromatic Profiler. The shape of the height data histograms of the two areas are similar (Figure 2.3), which indicates that although the surface features are random they are statistically similar.

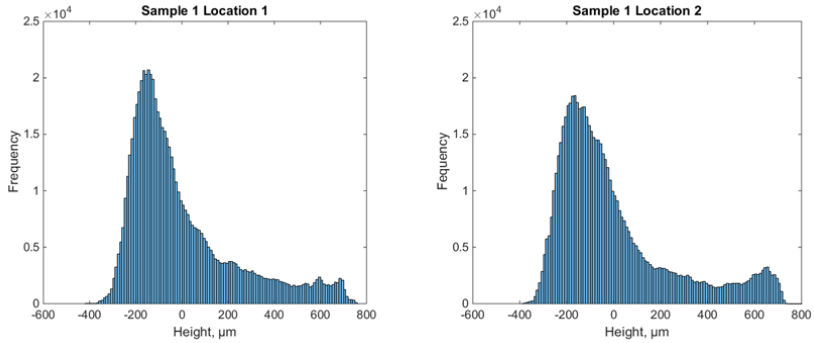

Figure 2.3: Histogram of the height data of Sample 1. The left plot shows patch 1 and the right plot shows patch 2.

Some descriptive statistics of the two measurements are shown in Table 2.1. S_a and S_q are the arithmetic and root-mean-square deviation from average height. They are within 5% of each other at two randomly selected patches. S_a and S_q are calculated using equations 2.12 and 2.13, respectively, where A is the area of a pixel and z is the height.

$$S_a = \frac{1}{A}\int\int_A |z(x,y)|dxdy \tag{2.12}$$

$$S_q = \sqrt{\frac{1}{A}\int\int_A z^2(x,y)dxdy} \tag{2.13}$$

Table 2.1: Sample 1 height statistics and roughness values

Parameter	Location 1	Location 2
Mode	-189	-188
Median	-77	-77
S_a equation 2.12	189	180
S_q equation 2.13	247	233

From this analysis, we conclude that the 4.0×4.0 cm patch is adequate to represent the

roughness of the whole surface. The remaining four samples were scanned using NPFLEX^{TM} White Light Interferometer Optical Profiling (Philips Innovation Services, Eindhoven, The Netherlands), which has an accuracy of 0.1 nm to 3 nm depending on the measuring technique, and the data processing was performed with MountainsMap® 6.2 (Digital Surf, Besancon, France). The white light interferometer was used because the Chromatic Profiler provided unsatisfactory results in terms of both coverage and the expected height data. Two samples out of four were coated by depositing a layer of silver 150 nm thick to enhance the reflection. Sample 2 is the regular pattern and hence the measurement was performed on 1.0×1.0 cm of the glass and a lateral resolution of 3.6 µm. Figure 2.4 shows the 3D surface topography of Sample 2. Figures 2.5, 2.6 and 2.7 show the 3D surface topography for samples 3, 4, and 5, respectively. The surface height differs substantially among the samples. The zero value is an arbitrary height which is defined as the average height after levelling. Table 2.2 summarizes all the sample-height statistics and roughness values.

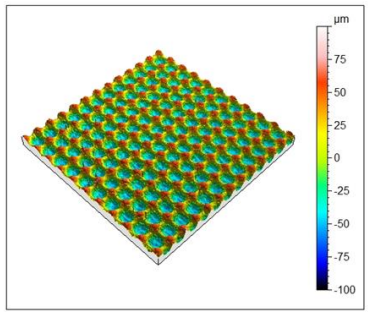

Figure 2.4: Sample 2 3D surface topography.

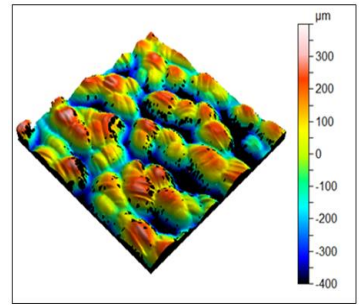

Figure 2.5: Sample 3 3D surface topography.

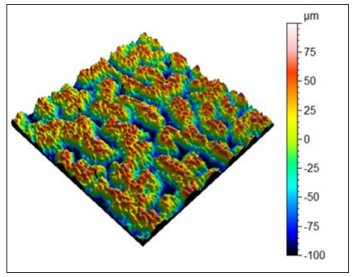

Figure 2.6: Sample 4 3D surface topography

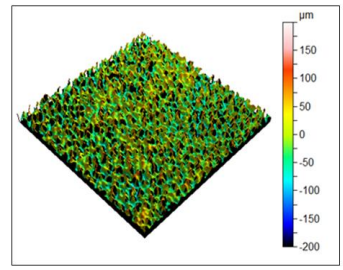

Figure 2.7: Sample 5 3D surface topography.

2.3.2. FRACTURE 2D FLOW NETWORK

Mobilizing or trapping a ganglion of the dispersed phase depends on both the aperture at the restriction in flow and the length of the ganglion. A fracture can be considered as

Table 2.2: Summary of all the sample height statistics and roughness values

Parameter	Sample 1	Sample 2	Sample 3	Sample 4	Sample 5
Mode	-189	-42	94.2	22.7	-31.7
Median	-77	-0.5	21.7	7.5	-6.9
S_a Equation (2.12)	189	29.1	131	36	35
S_q Equation (2.13)	247	33.7	157	44	42

a two-dimensional network of pore bodies (maxima in aperture) connected by throats (saddle points between pore bodies). Several methods are available in the literature to extract a realistic pore network of matrix rock samples, as described by Rabbani et al. (2014). The method we use is based on a simple concept using flood fill and image slicing. A MatLab® (The MathWorks Inc., Eindhoven, The Netherlands) code was developed to highlight all the areas with height less than a certain threshold and then produce images at every 5 μm increment in height for the very rough samples and increments of 10 μm for the less rough ones. An isolated, deep region represents a pore body. When two regions join upon increasing height, the connection between them is a pore throat. The sequence of images are loaded into ImageJ, an open-source Java image-processing program, to identify the pore throats and draw the pore-body boundaries. The pore-body depth is the deepest point surrounded by at least two throats. Appendix A shows histograms of pore-throat and pore-body heights. The constrictions to flow are not local maxima in height, but saddle points between them. The pore-throat and pore-body identifications were superimposed on the 3D topographic images of all the samples to generate the 2D networks. Appendix A shows pore-throat and pore-body locations on the fracture topography. Appendix A shows the 2D networks of pores constructed in this way. The lines are drawn around the pore bodies and connecting the pore throats of each pore. In some cases, we exclude shallow saddle points within a pore body and count them as part of the larger pore body. The 2D network was also used to estimate the characteristic length of a pore body, which is necessary for our definition of the capillary number in Equation (2.11). The length is measured in two directions for all the pore bodies and then an average value is used in the analysis. Semi-variogram analysis was also conducted to quantify the special variation of the roughness. The correlation length for the aperture is an alternate measure of ganglion length, as shown below. Appendix B shows the semi-variogram analysis of our model fractures. The distance between two consecutive peaks or troughs in the semi-variogram is the correlation distance.

2.4. EXPERIMENTAL DESIGN

The 30.0×10.0 cm-long model fracture consists of two glass plates, a clear glass plate on the top and a rough glass plate on the bottom glued together at the edges with adhesive. Two wooden holders are screwed on the fracture to prevent the glass from bowing outwards which could cause the aperture to vary. The bottom glass plate has injec-

tion and production ports, and two pressure ports with a distance of 16 cm in between. A pressure-difference sensor is connected to the model fracture, to provide pressure readings across an area of 16.0×10.0 cm. The sensors are silicon on-chip, signal conditioned and temperature compensated. These MPXV5010DP and MPXV5050DP transducers (Freescale Semiconductor Inc, Muenchen, Germany) , have a range of 0 to 10 kPa and 0 to 50 kPa, respectively, with a maximum error of 5.0% from 0°C to 85°C temperature. The sensors are connected to a data-acquisition unit and a computer, where pressure is recorded every one second. Water is injected through the standard infusion PHD pump Model-703005 (Harvard Apparatus, Holliston, United States). Flow rates are stated to be accurate within 0.35%, with reproducibility within 0.05%. This pump is equipped with micro-stepping techniques to further reduce flow pulsation. The pumping rate ranges from 0.0001 µl/hr to 220 ml/min. A high-definition camera is placed on top of the fracture to capture images at different stages during the experiment. A compact backlight (model CVI STAR-BL-110/110-WH-24V; Stemmer® Imaging, Zutphen, The Netherlands) provides constant and even illumination. Uniform light is needed to produce noise-free images which are used to obtain the saturation at different pressure gradients. The whole setup is placed in a 60×60×150 cm box to isolate the system from external lights, as shown in Figure 2.8. The setup is used first for measuring the hydraulic aperture, based on single-phase water flow, followed by capillary-desaturation experiments.

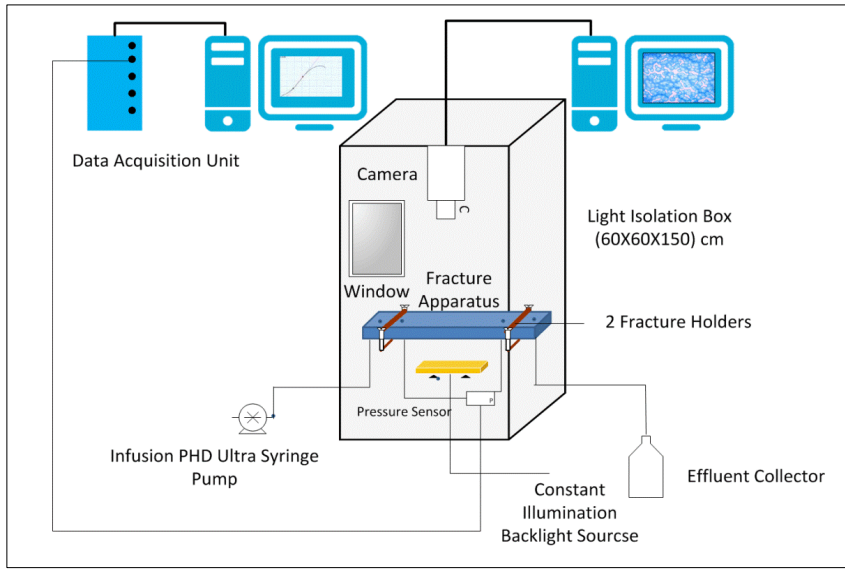

Figure 2.8: Experimental setup layout.

2.4.1. DETERMINATION OF HYDRAULIC APERTURE

To determine aperture from the height data, one must estimate the gap between the flat upper glass plate and the peaks in the roughened plate. Fluid flow through a single fracture has been described approximately by Equation (2.9) (Witherspoon et al., 1980; Hakami and Larsson, 1996); this equation assumes that the fracture comprises two smooth, parallel plates. The hydraulic aperture values were measured experimentally by injecting water and measuring the pressure gradient.

The hydraulic aperture values and the distribution of the height values were used with the effective medium approximation (EMA) to estimate the gap distance (dz) between the highest point of the rough plate and the flat top plate. If dz is zero, then the two plates are estimated to be in contact at the peaks of the roughened plate. This was estimated by comparing the hydraulic aperture from the experiments to that estimated using EMA and aperture distribution:

$$\int_0^\infty n(d)\frac{g_m - g(d)}{g(d) + \left(\frac{Z}{2} - 1\right) g_m}\mathrm{d}d = 0 \tag{2.14}$$

where $n(d)$ is the area fraction from the histogram of each surface, $g(d)$ is the conductivity (d^3) of aperture d at a particular location, Z is the coordination number of the network, and g_m is the effective conductivity of the medium , i.e. ${d_H}^3$. The value of Z was selected to be 4. This value was used previously to study single- and two-phase flow in a fracture (Rossen and Kumar, 1992). The distance dz was adjusted until Equation (2.14) was satisfied with $g_m = {d_H}^3$. The experiments starts with a small water flow rate and the rate is increased to obtain several pressure measurements. The flow experiments for our model fractures showed a linear relationship between Q and $|\nabla P|$, which indicates that the inertial forces were negligible and there was no change in aperture during flow.

This linear relationship is used in Equation (2.9) to obtain the hydraulic aperture. Appendix C shows the relation between flow rate and pressure gradient. The sensor was not able to record any pressure gradient in Sample 1 using water flow. Therefore, a 70 wt.% glycerol (49770 Sigma-Aldrich®; Sigma-Aldrich Chemie B.V, Zwijndrecht, The Netherlands) solution was used, after measuring its viscosity using an Anton Paar Rheometer (Anton Paar GmbH, Oslo, Norway). The viscosity of the solution was 0.0251 Pa s. Table 2.3, column 1 gives the values of the hydraulic aperture. The hydraulic-aperture values and the distribution of the height values were used using the EMA (Equation (2.14)) to estimate dz, as given in column 2 (Table 2.3).

We take the characteristic pore-throat aperture d_t in Equation (2.11) to be the aperture at the percolation threshold of this network. This is the height at which the fluid forms a continuous path across the patch in a specific direction. The flood-fill images were used to determine the percolation threshold. Appendix C illustrates the percolation threshold for each sample. We take the average pore-body aperture for d_b, and the average length of the pores (L_p) to be L_g. A simpler approach, and equally accurate, is to take the correlation length (L_{cor}) of the aperture distribution for L_g. Individual ganglia may differ in

Table 2.3: A summary of the geometric parameters and the geometric factor of the model fractures

Sample	d_H, μ m	d_z, μ m	d_b, μ m	d_t, μ m	L_p, μ m	L_{cor}, μ m	Geometric factor
Sample 1	660	0	1118	808	2661	2754	106.8
Sample 2	79	8	138	68	819	795	108.3
Sample 3	324	54	847	437	5156	4800	258.5
Sample 4	116	45	255	145	4415	5100	661.7
Sample 5	102	0	198	118	2421	2240	407.7

length from L_p or L_{cor}, but on average they are expected to scale with either measure, as in 3D porous media (Larson et al., 1981; Chatzis et al., 1983; Mayer and Miller, 1992). Table 3 summarizes the values of the characteristic pore-throat aperture (d_t), characteristic pore-body aperture (d_b), and the pore-body length estimated using pore-network analysis (L_p) and the semi-variogram (L_{cor}). The difference in length of the pore body between the two different procedures is modest. The pore-body length that is used in the calculation in the capillary number below is the one derived from the pore-network analysis. Table 2.3 also shows that the ratio (d_t/L_p) ranges from approximately 3 (Sample 1) to approximately 30 (Sample 4). The width of a throat in the fracture plane scales with (but is somewhat smaller than) L_p; this indicates that for all the fractures except for Sample 1 our assumption in Equatin (2.6) that interface curvature across the fracture aperture is much greater than that within the fracture plane is very good.

Numerous studies characterizing aperture variation and fracture-wall roughness could be used to generate such a representation (Tsang, 1984; Brown and Scholz, 1985; Wang and Narasimhan, 1985; Brown et al., 1986; Schrauf and Evans, 1986; Pyrak-Nolte et al., 1988; Morrow et al., 1990; Johns et al., 1993; Hakami and Larsson, 1996; Odling and Roden, 1997; Oron and Berkowitz, 1998; Hughes and Blunt, 2001; Karpyn et al., 2007; Lang et al., 2015, 2016)

2.5. CAPILLARY-DESATURATION EXPERIMENT

Water-air forced-imbibition experiments are conducted with dyed water to enhance the contrast between the air and water. The dye was Methylene Blue (Fluka Chemie AG, Buchs, Switzerland), with a concentration of 0.001 wt.% . The surface tension of the dyed water was 70.0 mN/m, as measured by KSV Sigma Tensiometer (Dyne Testing Ltd, Staffordshire, United Kingdom). We assume cos θ = 1 (perfectly wetting by water) in the calculations below, but at any case it is constant throughout the experiments. In these experiments, the procedure is as follows. The model fracture parts are thoroughly cleaned using ethanol before fabrication. The injected water is demineralized to avoid mineral precipitation. The syringe and tubes are changed for each model fracture experiment. Water is injected at 0.5 ml/min, in horizontal flow, until no further change in

saturation is observed. The rate is increased and an image is taken when two conditions are satisfied: first, no further change in saturation is observed, and, second, the pressure is stable for at least 15 min. Successive images are taken with incremental increases in injection rate until low residual saturation is achieved. The images are loaded into the image-processing software ImageJ to determine the saturation at each pressure gradient.

The hydraulic aperture of samples 1 and 3 are the largest, as shown in Table 2.3; therefore, no measurable pressure gradient was recorded with water in Sample 1, and insignificant pressure gradient in Sample 3. A glycerol mixture was therefore used instead. Methylene Blue-dyed water and glycerol appeared to be unstable to phase separation. Thus, a glycerol-based food coloring was used for these samples instead of Methylene Blue. The new mixture was stable and this dye has only a minor effect on the surface tension, as shown in Table 2.4. Precipitation was checked by measuring the surface tension and observing the sample appearance after the mixing and 24 hr afterwards.

Table 2.4: Surface tension measurement of glycerol mixture

Mixture	γ, mN/m	Comment
Glycerol (water 30 % + Methylene Blue)	64 to 52	Not stable over ½ hr
Glycerol (water 30 %)	66.3	Recently mixed
Glycerol (water 30 %)	66.2	Idle for 24 hrs
Glycerol (water 30 % + glycerol dye)	65.9	Recently mixed
Glycerol (water 30 % + glycerol dye)	65.6	Idle for 24 hrs

2.5.1. RESULTS

Appendix D shows the unprocessed and processed images of all the desaturation tests. An example of the unprocessed and the processed images is shown in figures 2.9 and 2.10. We developed two procedures for the analysis of the images: image thresholding to detect the boundary of the ganglion and the built-in finding-edges option in ImageJ. The difference between these two procedures is used as estimated error in the analysis of the saturation (Figure 2.11; Y-axis). The estimated error in N_{ca} (Figure 2.11; X-axis) reflects fluctuations in the measurements of the pressure sensor. Figure 2.11 shows the relation between air saturation normalized to initial saturation and pressure gradient. In a few cases at relatively low pressure gradient, gas trapped upstream was displaced into the region we monitored and became trapped there; thus in a few cases normalized saturation increases before it declines with increasing pressure gradient. The pressure gradient $|\nabla P|$ required to mobilize ganglia and the rate of change of saturation differ among the samples. The aperture size and the length scale along which the aperture varies explain the difference in pressure gradient required to mobilize ganglia in the five model fractures. Figure 2.12 shows the capillary-desaturation curve of the five samples plotted against the conventional capillary number (Equation (2.2)) plotted in a semi-log scale

(Larson et al., 1981; Lake et al., 1986; Sheng, 2015). The scatter is less than in Figure 2.11, but still the trend varies by at least an order of magnitude in N_{ca}. Using the experimental data along with the geometric factor we determined for the individual model fractures (Equation (2.11)), the relationship can be represented approximately by a single curve (Figure 2.12). The trends for four of the samples overlie each other, and Sample 2 differs from the others by much less than an order of magnitude. The new capillary number falls in a higher range due to the geometric factor. The new definition derived from a force balance on a ganglion trapped in a fracture better represents the mobilization of the nonwetting discontinuous phase in the fracture, by using the geometric parameters for the fracture. As noted, means exist to measure the parameters required for this geometric factor. Alternatively, it may be possible to develop heuristics to relate fractures of different types (shear or open fractures) or in different geological formations to these parameters, much as N_{ca} correlations in rock are adjusted for different formations (Larson et al., 1981; Lake et al., 1986).

2.6. CONCLUSIONS

- A new definition of capillary number for fractures was defined from a force balance on a trapped ganglion in a fracture.
- Three geometric parameters were identified to describe features governing mobilization. These parameters can be determined from analysis of a map of the fracture aperture along the fracture, with no two-phase flow data.
- A 2D pore-network representation of each fracture was generated from the map of the aperture using flood-fill and image-slicing techniques.
- Experimental desaturation experiments were conducted to quantify the relationship between the trapped ganglions and the pressure gradient relationship.
- The new definition of capillary number was tested in the experimental data and showed its suitability to describe the mobilization of trapped nonwetting phase in fractures.

Figure 2.9: Capiliary-desaturation experiment of Sample 4 (unprocessed Images)

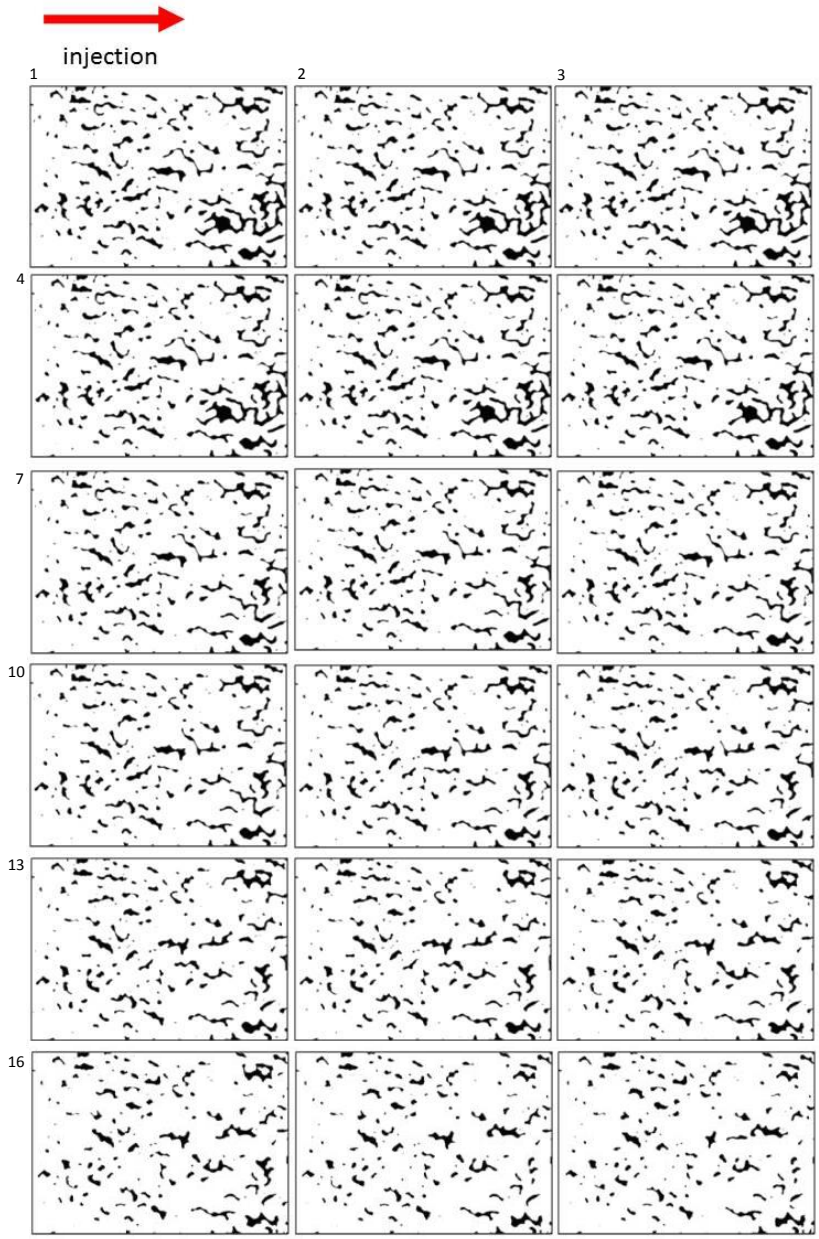

Figure 2.10: Capiliary-desaturation experiment of Sample 4 (processed images)

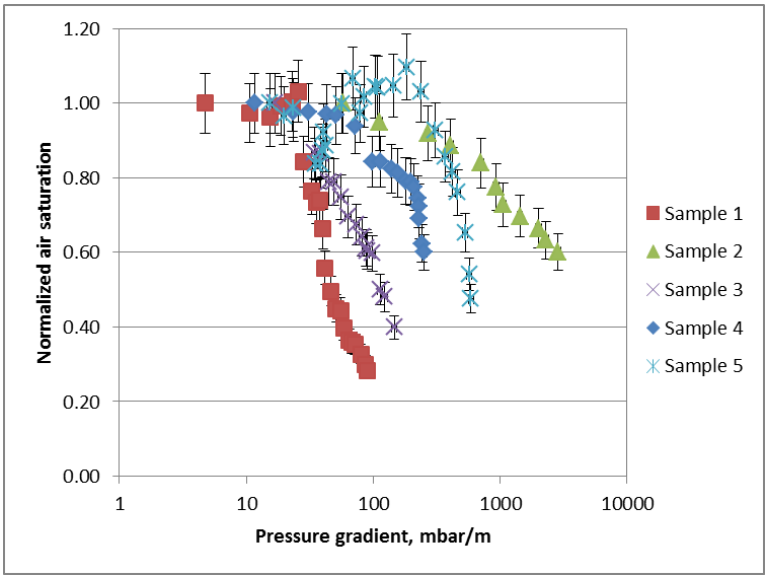

Figure 2.11: Normalized air saturation in experiments vs pressure gradient for the different five model fractures. The estimated error in the Y-axis represents the uncertainty in the analysis of images of trapped air while estimated error in the X-axis represents the maximum error of the pressure sensor.

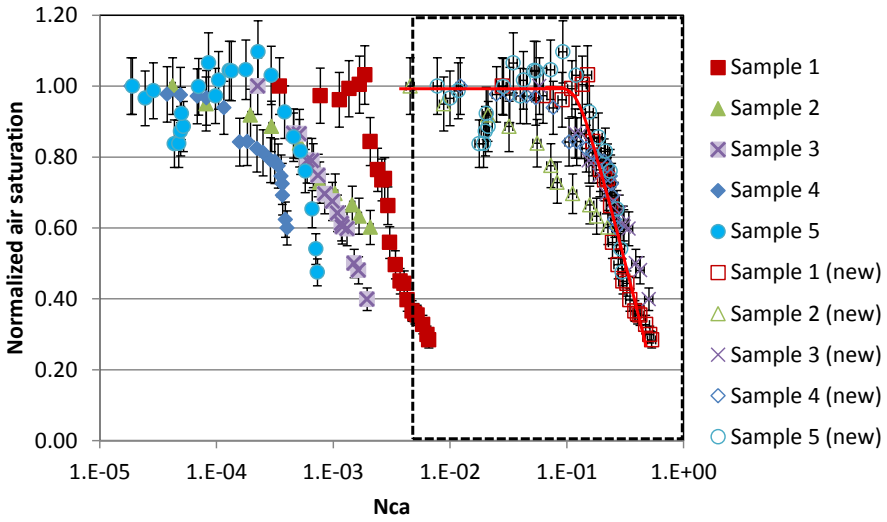

Figure 2.12: Comparison between Conventional and new capillary numbers. conventional capillary number (Equation (2.2)). The trend varies considerably between samples. The plot shows that the trend cannot be captured by the conventional capillary number. The new capillary number (Equation (2.11)). The relationship can be represented by approximately a single curve if the defined fracture geometric parameters are considered. A curve is drawn through the new capillary number data to guide the eye.

3

STUDY OF FOAM GENERATION AND PROPAGATION IN A FULLY CHARACTERIZED PHYSICAL-MODEL FRACTURE

FOAM greatly reduces gas mobility for gas enhanced-oil-recovery (EOR) projects. It substantially increases both the effective viscosity of gas and gas trapping. Numerous studies have been conducted to understand foam rheology in rock matrix both theoretically and experimentally. The knowledge of foam flow in fractured porous media is incomplete, however. This study aims to contribute to the understating of foam generation and propagation in a fully characterized physical-model fracture. We investigate foam-generation mechanisms and the propagation of pre-generated foam. Gas mobility was greatly reduced as a result of in-situ foam generation. Foam-generation mechanisms similar to those seen in 3D porous media were observed on this model fracture. Foam was generated predominantly by capillary snap-off and lamella division. Lamella division was observed at high gas fractional flow at two different superficial velocities. Fracture wall roughness played an important role in foam generation. In the case of pre-generated foam, two very distinct bubble sizes were injected: fine-textured bubbles much smaller than the roughness scale and coarse-textured foam with bubbles much larger than the roughness scale. The first case did not show any significant change in bubble size as foam propagated through the model fracture, while in the second case, the fracture played a role in reducing bubble size. Inter-bubble diffusion did not regulate bubble size in our apparatus because residence time in the fracture is relatively short. We cannot confirm that foam reached local equilibrium in our experiments but

This chapter is based on AlQuaimi, B. I., and Rossen, W. R. (2017), Study of foam generation and propagation in a fully characterized physical-model fracture. Submitted to the Journal of Petroleum Science and Engineering.

we believe that local equilibrium lies between the cases of in-situ- and pre-generated foams.

3.1. INTRODUCTION

Naturally fractured reservoirs (NFRs) have been receiving more attention over the last few decades due to the vast reserves of crude they contain. NFRs are found in many countries around the globe, in almost every lithology (Aguilera, 1995; Narr et al., 2006). Over the last four decades NFRs in the USA, for instance, have been under primary production, water injection and CO_2 flood (Manrique et al., 2007). Tertiary recovery or enhanced-oil-recovery (EOR) methods, including the injection of miscible carbon dioxide, steam, or nitrogen, have been implemented or considered for these reservoirs to recover the oil by-passed or not displaced during primary production (Manrique et al., 2007; Babadagli et al., 2001; Bourbiaux et al., 2016, 2017). However, these fluids impose challenges due to their density and viscosity differences compared to in-situ fluids (Kim et al., 2005). These differences cause gravity override and viscous instability and worsen channelling, all of which are much more pronounced in NFRs because of the high conductivity of fractures. A statistical review of the overall ultimate recoveries of 100 NFRs indicates that the recovery of NFRs is somewhat lower than those of many conventional reservoirs (Allan and Sun, 2003). Considerable oil reserves are not recovered because of the nature of these reservoirs, which is a strong motivation for considering the use of foam to mitigate the low oil recovery expected in gas injection EOR.

Chapter 1 provides a brief summary of the studies of foam EOR in a single fracture or in multiple fractures. Most of these studies discuss the behavior and benefits of pre-generated foam in a fracture. Only two studies address foam generation, in a 12-cm-diameter disk-shaped fracture and a 31.2-cm-long fracture with some vugs (Fernø et al., 2016; Kovscek et al., 1995). In these tests, the pressure drop was measured across the whole sample with little information about pressure gradient and foam texture as a function of position. In this study, we investigate foam generation and propagation in a well-characterized model fracture, 40 cm long, with 4 pressure measurements. Mechanisms of foam generation as well as bubble size can be observed directly along the fracture. Moreover, we compare in-situ-generated foam with pre-generated foam over foam qualities ranging from 25 to 97%.

3.2. FRACTURE PHYSICAL MODEL

We investigated different design alternatives used in the literature to perform fracture flow experiments. Sawed or fractured rock cores do not allow one to directly observe foam texture and generation mechanisms inside the rock sample. Microfluidic devices have limited size and feature abrupt changes in otherwise smooth faces. A third option is to design a fracture apparatus made of glass plates. Model fractures made of glass plates have been used to study foam and two-phase flow in fractures (Pruess and Tsang, 1990; Fourar et al., 1992; Pieters and Graves, 1994; Chen et al., 2004a,b; Yan et al., 2006; Qian et al., 2011; AlQuaimi and Rossen, 2017b). The transparent nature of the glass provides the ability to observe the flow and investigate foam generation mechanisms. More im-

portantly, it allows one to systematically vary roughness scales (magnitude of aperture, aperture variation and length scale over which aperture varies) and investigate the effect of these on foam generation, stability and mobility. The goal is to develop means to relate foam to the different fracture geometries encountered in field applications. This is the first report of a series; here we report on foam generation for the first of our model fractures.

We constructed a 40×10 cm model fracture that consisted of a roughened plate to represent the fracture roughness and a top plate that is smooth, to allow direct observation of the flow. The roughened plate is 4 mm thick and was strengthened by attaching a 15 mm-thick plate of glass using ultraviolet light and DELO®-Photobond® glue (DELO, Windach, Germany). The thickness of the top glass plate is 15 mm as well. The thickness of the glass plates was estimated based on solid-mechanics calculations to prevent any glass deflection during the flow. This was also checked using a Probe Indicator (2 μm resolution) during the experiment. The roughened plate included two inlet ports that allow separate co-injection of gas and liquid. These inlet ports were connected to 8.0×2.0×0.04 cm entry regions milled into the roughened plate. Four pressure ports were equally spaced over a length of 36 cm and including the fluid outlet. The gap between the top plate and the rough surface represents the fracture aperture. The two glass plates were glued together around the edges using Araldite® 2014, which is an epoxy adhesive that has a tensile strength of 26 MPa at 23°C. The fracture was mounted in a frame that can slide 50 cm in X and Y directions to allow for microscopic observation of flow in the whole 40×10 cm fracture. In all experiments reported here, the fracture was held horizontal.

3.2.1. FRACTURE CHARACTERIZATION

The model fracture used here has a regular pattern to its roughness, as shown in Figure 3.1. It provides an initial case study of foam behavior prior to testing more complicated surface geometries (AlQuaimi and Rossen, 2017a,c). The roughened glass sample was profiled using NPFLEX™ White Light Interferometer Optical Profiling (Philips Innovation Services, Eindhoven, The Netherlands), to quantify the spatial and vertical variations in height. A separate sample of the same glass was coated by depositing a layer of silver 150 nm to enhance the reflection. Since this is a regular pattern of roughness the measurement was performed on a 1.0×1.0 cm region of the glass with a lateral resolution of 3.6 μm (Figure 3.1)(a). A fracture can be considered as a two-dimensional network of pore bodies (maxima in aperture) connected by throats (saddle points in the topography of Figure 3.1 between pore bodies) (Tsang, 1984; Pyrak-Nolte et al., 1988; Rossen and Kumar, 1992; Hughes and Blunt, 2001). Locations of minimum aperture (highest locations in the topography of Figure 3.1(b) are occupied by water at all times in our experiments.

Several methods are available in the literature to extract a realistic pore network description for matrix rock samples (Rabbani et al., 2014). The method we use is based on a simple concept using flood fill and image slicing (AlQuaimi and Rossen, 2017a). A MatLab® (The MathWorks Inc., Eindhoven, The Netherlands) code was developed to highlight all areas with height less than a certain threshold and then produce images at every 5 μm

increment in height. An isolated, deep region represents a pore body. When two regions join upon increasing height, the connection between them is a pore throat. The sequence of images is loaded into ImageJ, an open-source Java image-processing program, to identify the pore throats and draw the pore-body boundaries. The characteristic pore-throat aperture (d_t) is taken at the percolation threshold for the region studied, the characteristic pore-body aperture (d_b) is the average pore-body aperture, and the characteristic pore length (L_p) is the average pore-body length of the 2D network in the flow direction (Figure 3.1)(b). We vacuum the model fracture and inject demineralized water to displace all the air from the system. We next measure the hydraulic aperture of the model fracture by incrementally increasing the water injection rate and recording the pressure. The rate-pressure relationship was used to estimate the hydraulic aperture (Witherspoon et al., 1980; Hakami and Larsson, 1996; Chen et al., 2004a; Fernø et al., 2016):

$$Q = \frac{1}{12}\frac{|\nabla P|\, w d_H{}^3}{\mu} \tag{3.1}$$

where Q is the volumetric flow rate, $|\nabla P|$ is the pressure gradient, w is the width of the fracture in the fracture plane, d_H is the hydraulic aperture, and μ is the viscosity. The flow experiments for our model fractures showed a linear relationship between Q and $|\nabla P|$, which indicates that the inertial forces were negligible and there was no change in the aperture during the flow (Figure 3.2).

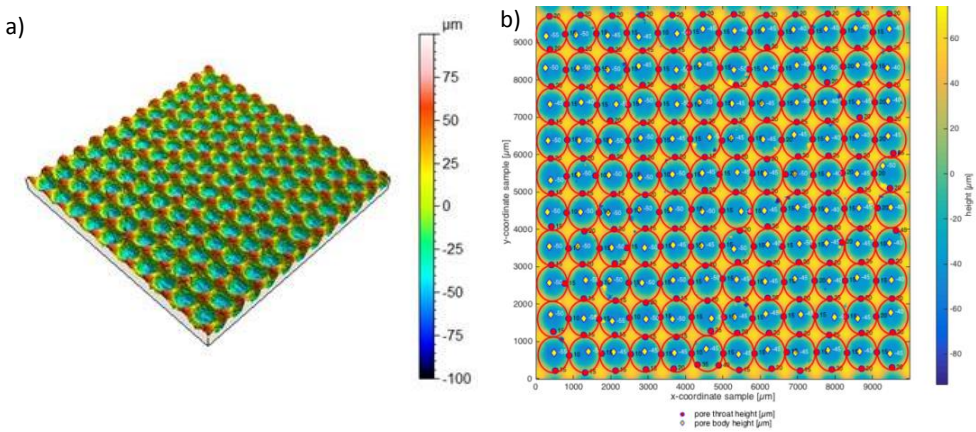

Figure 3.1: (a) Bottom glass surface topography. (b) 2D Network of pore bodies (blue) and pore throats (red). Region shown 1x1 cm.

Table 3.1 summarizes the fracture-aperture data. The table also shows the characteristics of the rough surface. Additional details on the characterization of the fracture data are reported by AlQuaimi and Rossen (2017a) (Chapter 2).

Table 3.1: Sample 1 height statistics and roughness values

Parameter	value, µm
Pore-throat aperture, (d_t)	60
Pore-body aperture, (d_b)	130
Hydraulic aperture (experimentally determined), (d_H)	66
Pore length, (L_p)	815
Arithmetic average absolute deviation from average aperture, (S_a)	29
Root-mean-square deviation from average aperture, (S_q)	34

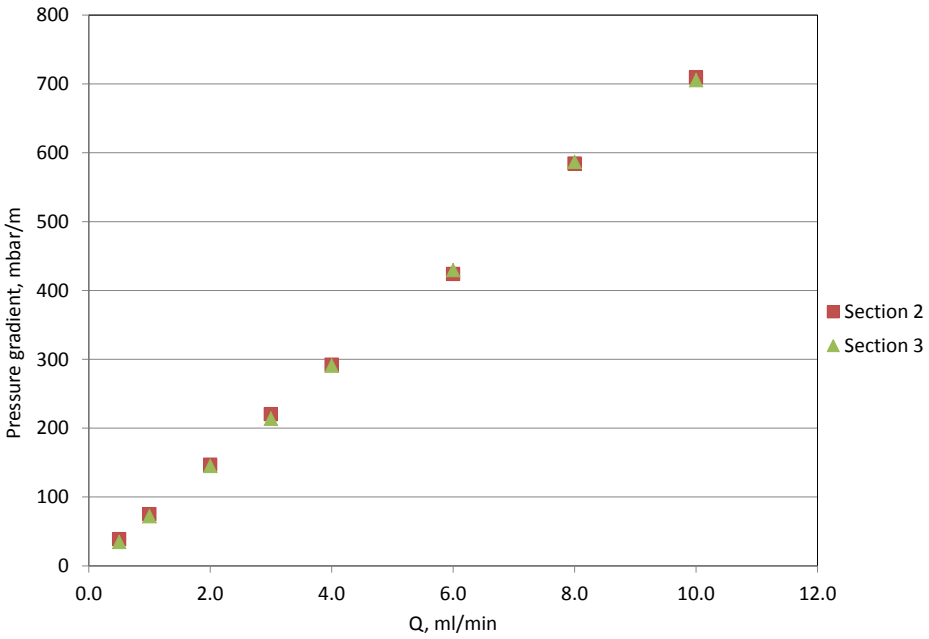

Figure 3.2: Rate-pressure gradient relationship.

3.3. EXPERIMENTAL SETUP

The model fracture discussed above is the centrepiece of the setup. Sodium C14-16 olefin sulfonate (Bio-Terge®- AS-40 KSB, Stepan, Voreppe, France), an anionic surfactant with 39 wt.% active component and a critical micelle concentration of 301.0 mg/l, was used to generate foams. We prepared a surfactant solution of 1.0 wt.% to be used in all the experiments. The surfactant solution is injected using a Standard Infusion PHD Ultra Syringe Pump (Model-703005, Harvard Apparatus, Holliston, MA, USA). Flow rates

are stated to be accurate to within 0.25%, with reproducibility within 0.05% of full scale. This pump is equipped with micro-stepping techniques to further reduce flow pulsation. The pump has a range from 0.0001 µl/hr to 216 ml/min.

Nitrogen is injected through a gas mass-flow meter/mass-flow controller (EL-Flow® F-230M-RAD-22-K, Bronkhorst High-Tech B.V., Ruurlo, Netherlands) which has a range of 0-10 mln/min. The bottom glass plate includes four pressure ports with a distance of 9.0 cm between them, to provide pressure readings across the length of the apparatus. The pressure-difference sensors are signal-conditioned and temperature-compensated. These sensors (MPXV5050DP, Freescale Semiconductor, Inc., Austin, TX, USA) have a range from 0 to 50 kPa (0 to 7.25 psi) with a maximum error of 2.5% from 0°c to 85°c temperature. The sensors are connected to a data-acquisition unit and a computer, where pressure is recorded every second.

For monitoring in-situ foam generation and foam texture a LEICA MZ 8 Microscope (10445538 1.0X, Leica Microsystems B.V., Amsterdam, Netherlands) is used. The microscope is connected to DRS's lightning RDTTM camera, consisting of a small camera head, detachable cable and custom frame-grabber board. The lightning RDTTM is an ultrafast, high-resolution camera that captures 1280×1024-resolution images at 500 full frames per second (fps). Higher fps of 16,000 can be achieved at reduced resolution for recording extremely rapid events. MiDAS 2.0 camera-control software (Xcitex Inc., Woburn, MA, USA) is also used to process the images/videos in real time during recording. A compact backlight (model CVI STAR-BL-110/110-WH-24V; Stemmer® Imaging B.V., Zutphen, Netherlands) provides constant and even illumination. Uniform light is needed to produce noise-free images. Figures 3.3 and 3.4 show the experimental setup.

3.4. IN-SITU FOAM GENERATION

In the model fracture, foam was generated in situ by similar mechanisms to those observed in rock porous media. First, we vacuum-saturated the fracture with water (no surfactant), followed by co-injection of gas and surfactant solution. The gas remained in the entry region until the gas pressure exceeded the capillary entry pressure of the fracture. Leave-behind lamella generation was observed upon initial gas entry in the vicinity of the entry region, as gas displaces water, leaving lenses in the throats. Figure 3.5 shows a sequence of images showing lens creation by leave-behind between gas entry paths. This foam was generated at 0.25 fractional flow of gas (f_g) and total superficial velocity u_t of 0.0021 m/s.

Lamella division occurs when a film of a large bubble divides as it encounters a split in the flow path. Figure 3.6 shows foam generation by lamella division at f_g = 0.88 and u_t = 0.0021 m/s. Lamella division was observed frequently at high f_g, especially when a foam bubble is larger than one pore body.

At lower f_g (0.37), u_t = 0.0021 m/s, at a distance of 20 cm from the injection point, as the foam front advances, foam was generated by repeated capillary snap-off events, until the given pore fills with bubbles. Fine-textured foam was created at the front, with bubbles

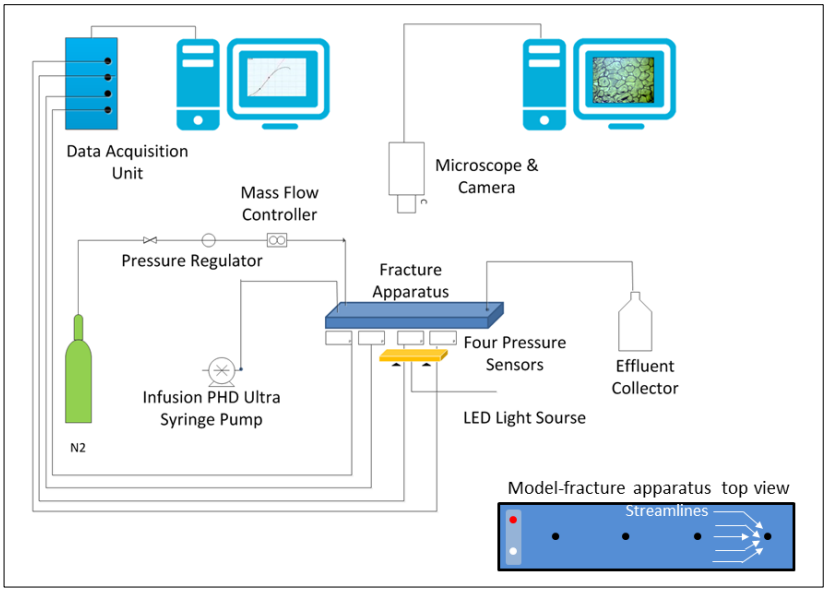

Figure 3.3: Schematic of the experimental setup. The bottom right shows the model-fracture design and the converging flow.

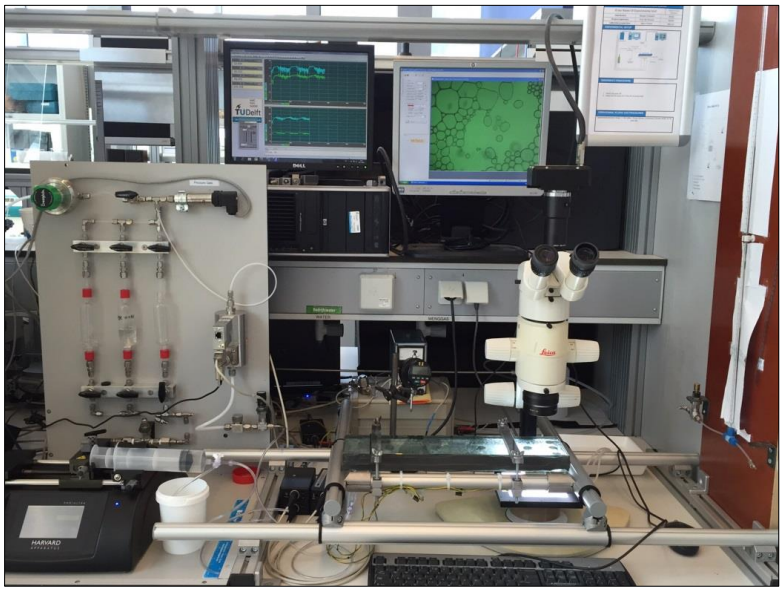

Figure 3.4: Photo of the experimental setup.

often smaller than the pore bodies and coarser foam behind (Figure 3.7). Snap-off of bubbles much smaller than pores reflects in part the slit-shaped geometry of the pore

throats (Rossen, 1996, 2003). For this model fracture the aperture at a pore throat d_t is much less than the width of the throat w. The capillary entry pressure is given by

$$P_c{}^e = \sigma\left(\frac{1}{\frac{w}{2}} + \frac{1}{\frac{d_t}{2}}\right) \cong \frac{2\sigma}{d_t} \tag{3.2}$$

where σ is the gas-liquid surface tension (Lenormand et al., 1983). The capillary pressure for snap-off $P_c{}^{sn}$ is $(2\sigma/d_t)$. Pore-throat aperture d_t is approximately 60 μm (Table 3.1), and throats are approximately 400 μm wide in the other direction (cf. pore length in Table 3.1 and pore geometry in Figure 3.1). For this surfactant σ = 0.031 N/m and d_t = 60 μm; therefore $P_c{}^e$ = 11.9 mbar and $P_c{}^{sn}$ is 10.3 mbar. In this geometry, where a pore throat approximates a slit, the ratio of capillary pressure for snap-off to capillary entry pressure ($P_c{}^{sn}/P_c{}^e$) approaches 1: a slight fluctuation in P_c can cause snap-off in such a throat. In rock matrix bubbles are thought to be as large as pores (Alvarez et al., 2001), in part because diffusion rapidly eliminate smaller bubbles. Appendix E presents an analysis of inter-bubble diffusion, which is slower in a slit-like geometry and does not have time to operate in the bubble residence time (approximately 2.66 min) in our apparatus. Figure 3.8 shows that bubbles typically advance on a scale of a few seconds. A similar observation was reported for foam flow in fractures (Haugen et al., 2014; Fernø et al., 2016). Appendix E shows an experiment to estimate the time taken for a small bubble to disappear by diffusion. The experiment confirms that diffusion is very slow on the time scale of our experiment.

Liquid lenses are created by snap-off and leave-behind during initial gas invasion, but many of these break without surfactant to stabilize them. With surfactant, these lenses survive as they drain to lamellae, and the gas phase remains discontinuous. The liquid lamellae and lenses block the paths of continuous flow and hence this increases flow resistance. Figure 3.9 shows trapped gas and the flow path of water in the case of no surfactant present. The mobility of both water and gas is much greater than if surfactant stabilizes the lamellae formed in the two-phase flow.

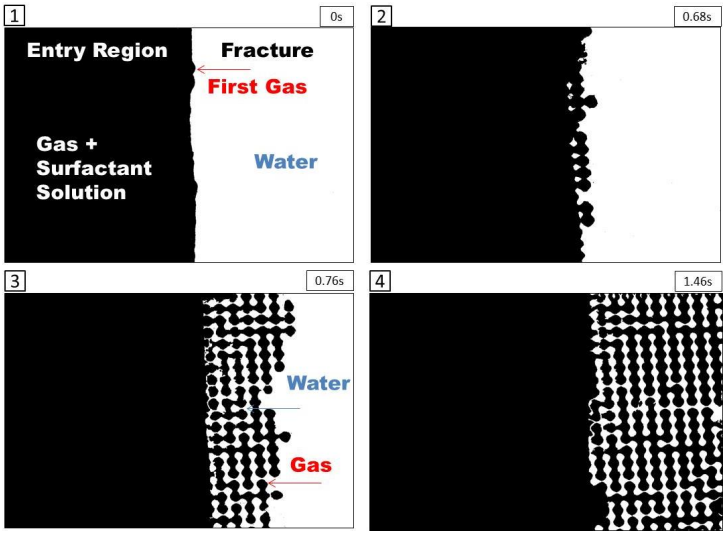

Figure 3.5: A sequence of processed images (2.2×1.5 cm) that shows lens creation by leave-behind. f_g = 0.25 and u_t = 0.0021 m/s. Black is gas and white is water. The images span a period of 1.46 seconds.

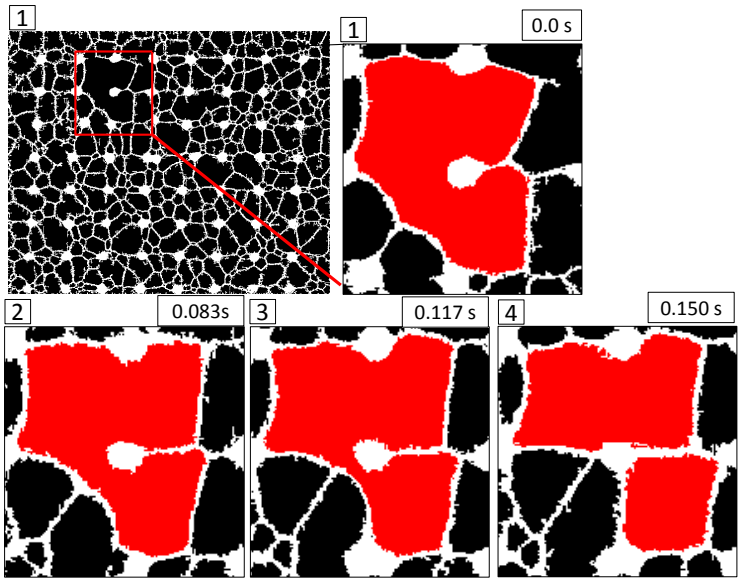

Figure 3.6: A sequence of processed images (0.18×0.2 cm) of foam generation by lamella division f_g = 0.88 and u_t = 0.0021 m/s. Black is gas and white is water. The images span over a period of 0.15 seconds. The divided bubble is highlighted in red.

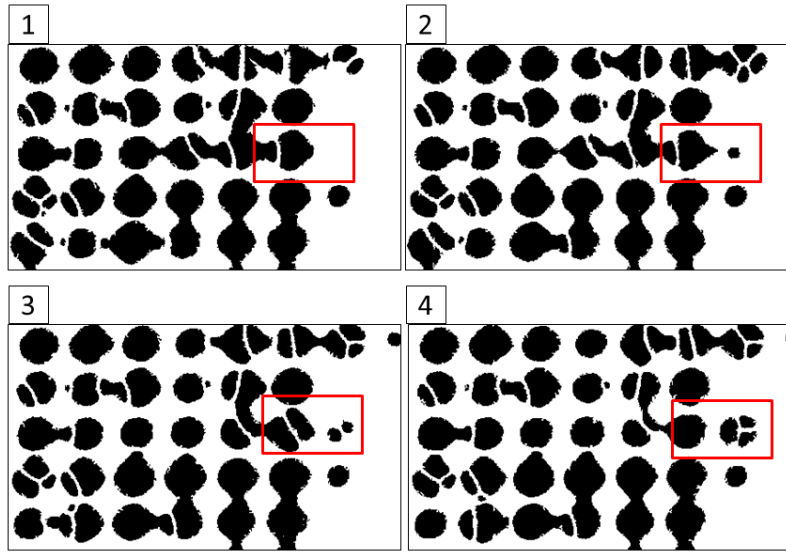

Figure 3.7: A sequence of processed images (0.43×0.75cm) that shows foam generation by capillary snap-off and foam propagation. Black is gas and white is water. The red rectangle highlights the event.

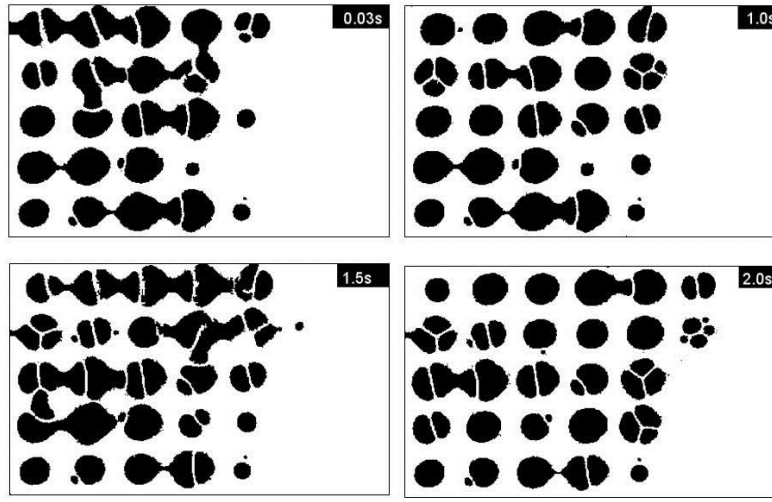

Figure 3.8: A sequence of processed images (0.45×0.75 cm) that shows movement of bubbles.

3.5. FOAM PROPAGATION

In general, underground rock fractures are large features which could span the reservoir height and extend hundreds of meters horizontally (Bertotti et al., 2005; Ozkaya, 2007). Thus, foam re-generation and propagation far into the reservoir is critical for the suc-

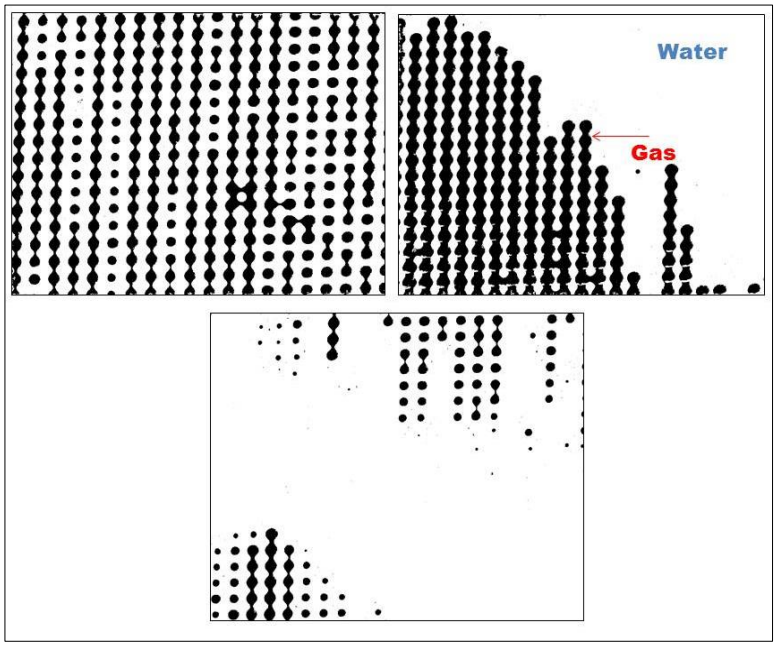

Figure 3.9: Images (2.0×1.5 cm) show gas and water flow (no surfactant) f_g (0.37), u_t = 0.0021 m/s. The bottom image shows that water advances in separate paths from gas. Flow is from left to right. Images were captured at three locations.

cess of the foam-injection process. We monitored bubble texture of the foam across the fracture at steady-state flow conditions. This test was conducted at f_g of 0.37, u_t of 0.0021 m/s and 1.0 wt.% surfactant solution. Figure 3.10 illustrates foam bubble texture at steady state from three locations, at 20, 120 and 270 mm from the injection port. The images demonstrate that finer foam continues to be generated as it propagates through the fracture. Figure 3.10 shows that the number of bubbles per unit area of fracture almost doubles toward the end of the model fracture (Table 3.2). As noted, at this low value of f_g (0.37), the dominant mechanism of lamella creation is snap-off. The pressure gradient increases as more bubbles are created. Thus the "entrance effect" seen in 3D porous media (Ettinger et al., 1992) extends 10's cm in our model fracture. Figure 3.11 shows the evolution of the pressure drop across the entire fracture. The pressure gradient in the first section is affected by the entry region and the last one by the converging flow towards the outlet, so they were not used in the analysis. Thus, we select the third section to base our comparison of the pressure-gradient behavior. We cannot directly confirm from these data that foam is at local equilibrium in the third section (see dissertation below), but it is our best basis of comparison. Figure 3.12 compares steady-state pressure gradient for pure gas injection, water injection, and co-injection of gas and water (no surfactant). A much greater pressure gradient was achieved when foam was injected compared to the other cases.

Figure 3.10 shows that bubble size decreases as foam flows along the fracture. It also shows that the fraction of the fracture area covered by water increases downstream. Water saturation S_w is monotonic with the area fraction covered by water, though we do not have the exact conversion from area fraction to saturation. Since pressure gradient is larger downstream, this implies that water relative permeability K_{rw} decreases as water saturation increases downstream. In 3D porous media,, it is often reported that the K_{rw} (S_w) function is unaffected by foam (Bernard and Holm, 1964; Holm, 1968; Huh and Handy, 1989), and this assumption underlies most foam simulation models. It is evidently not the case here, since K_{rw} decreases as S_w increases.

It could be argued that the capillary entry pressure explains the accumulation of water in sections 2 and 3 in Figure 3.10. However, the capillary entry pressure, as noted above, is approximately 11.9 mbar. The pressure difference in Section 4 alone (cf. Figure 3.11) is approximately 270 mbar, greatly exceeding the capillary entry pressure. Therefore, the impact of the capillary end effect on sections 2 and 3 is expected to be modest.

We performed foam-quality scans, where u_t is fixed and f_g is varied (Figure 3.13). The left-hand vertical axis shows foam apparent viscosity (μ_{app}) at different foam quality, with highest apparent viscosity at $f_g = 0.62 = f_g^*$. μ_{app} is calculated using Equation (3.3):

$$\mu_{app} = \frac{1}{12} \frac{|\nabla P| \, w {d_H}^3}{Q} \tag{3.3}$$

where $|\nabla P|$ is pressure gradient, w is the width perpendicular to flow, d_H is the hydraulic aperture, and Q is the volumetric flow rate. The data points have numbers which indicate the sequence at which they were acquired. This sequence was chosen to avoid possible hysteresis that might occur in the case of sequential increase or decrease in f_g. The value near zero for $f_g = 0$ represents the viscosity of water injection with no gas present. Additionally, point 7 at f_g of 0.25 was repeated after displacing all the foam and starting the experiment with the initial condition of only water in the fracture. This gives extra confidence in the measurement and the procedure followed to acquire the data. The error bars in μ_{app} data reflect oscillations in pressure gradient (cf. Figure 3.13).

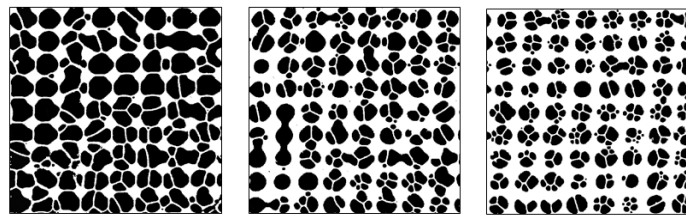

Figure 3.10: 0.8×0.77 cm images of foam texture versus distance from the injection point after the steady-state pressure gradient is achieved (Figure 3.11). Left: Section 1; middle: Section 2; right: Section 3. $f_g = 0.37$ and $u_t = 0.0021$ m/s.

Table 3.2: Image analysis statistics from Figure 3.10. The number of bubbles per unit area of the fracture almost doubles towards the end of the model fracture.

Section	1	2	3
Distance from inlet, mm	20	120	270
Average bubble size, mm^2	0.250	0.138	0.081
Bubble size, std. dev., mm^2	0.205	0.125	0.056
Number of bubbles per unit area	165	217	303

At high quality, we observed a cycle in which fine-textured foam is generated and propagates, followed by a slug of gas that is refined as it propagates. This causes the pressure response to fluctuate and hence reduces time-average foam apparent viscosity (AlQuaimi and Rossen, 2017b). In nonfractured porous media the decrease of foam apparent viscosity at high quality is believed to reflect destruction of foam at a limiting capillary pressure (Khatib et al., 1988; Ransohoff and Radke, 1988; Alvarez et al., 2001). In our results, in contrast, it reflects less efficient foam generation. The right-hand vertical axis (red symbols) shows the average bubble size determined from images taken at the stabilized pressure gradient (cf. Figure 3.14) in Section 3. The average bubble size correlates inversely with the pressure gradient, as expected; the error bar is the standard deviation of the average bubble size. The standard deviation of the bubble size increases with the increase in f_g due to reduced and fluctuating foam generation. Figure 3.14 shows that the foam-bubble shape becomes polyhedral at high foam quality.

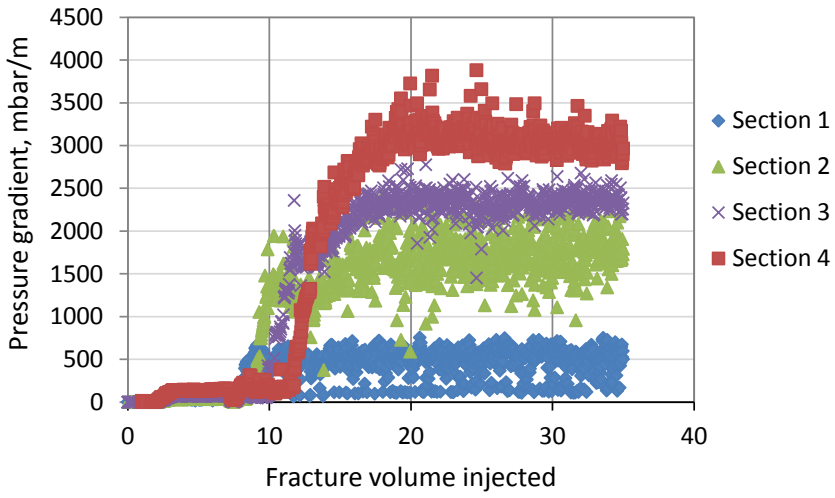

Figure 3.11: Pressure gradient along the model fracture; $f_g = 0.37$, $u_t = 0.0021$ m/s

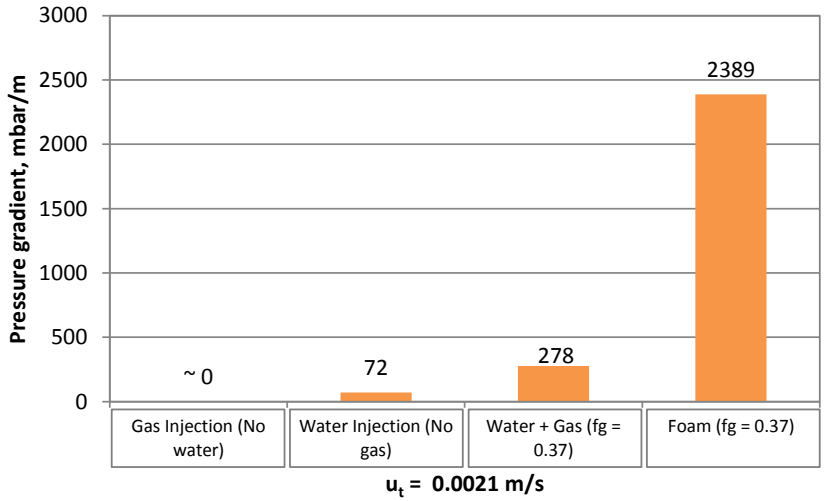

Figure 3.12: Pressure gradient for foam injection compared to gas, water and co-injection of gas and water. Pressure gradient with gas alone was too small to measure.

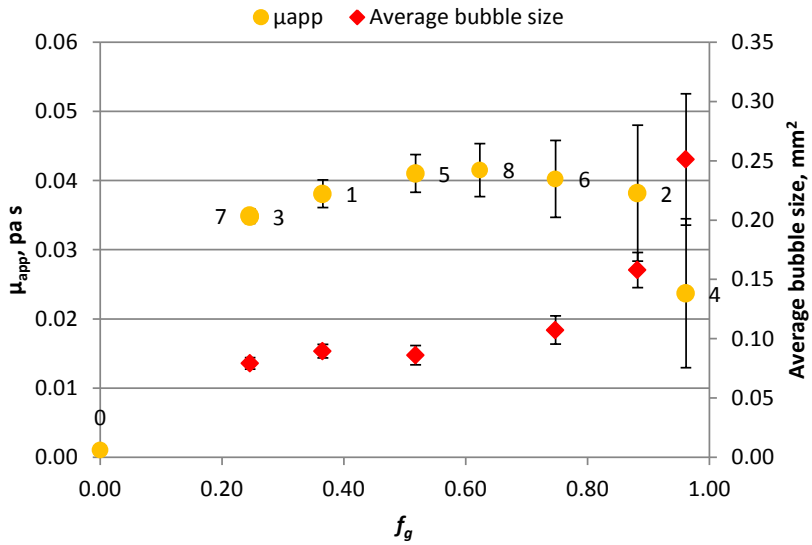

Figure 3.13: Foam apparent viscosity μ_{app} and average bubble size over a range of foam qualities; u_t = 0.0021 m/s. Error bars in μ_{app} reflect fluctuations in pressure gradient. Error bars in bubble size indicate standard deviation in the bubble size.

3.6. INJECTION OF PRE-GENERATED FOAM

We investigated the behavior of pre-generated-foam flow in our model fracture. Foam was generated upstream of the fracture apparatus using foam-generator filters. We se-

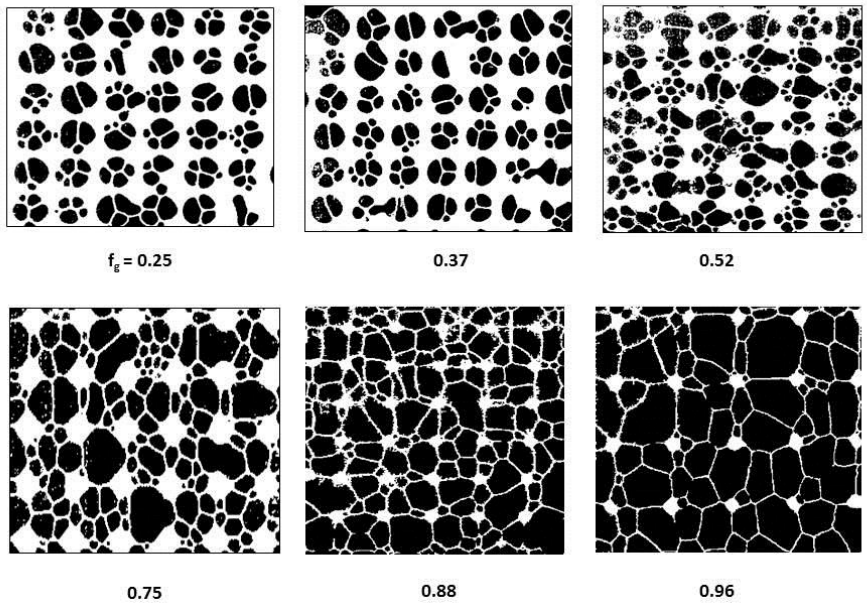

Figure 3.14: Foam texture versus f_g, (white is water and black is gas.) Images were captured with the stabilized pressure gradient, 270 mm from injection port. Image size is not identical in each case, but it is of the order of 0.4×0.48 cm.

lected two very distinct sizes of filters, with openings of 7 and 400 μm, to generate two different foams. In the flow of bulk foam through the tubing and in the entrance port, bubbles are expected to grow by inter-bubble diffusion (Nonnekes et al., 2015). In our experiments the bubbles grew considerably before they reached the model fracture. Bubbles initially 7 μm in size were still smaller than pores as they entered the fracture. Bubbles of initially 400 μm grew to sizes much greater than the pore size in the fracture. The experimental setup was the same except for the filter added upstream of the model fracture. The surfactant solution and nitrogen were injected through two different lines to the filter where foam was generated.

The same experimental conditions were used to generate foam in each case. The fracture was fully saturated with water (no surfactant). Surfactant solution (1.0 wt.%) was injected with nitrogen through the filter, at a superficial velocity u_t = 0.0021 m/s. With the 7-μm filter, foam bubbles were already considerably smaller than the pore throats (flow restrictions), so foam was not refined by snap-off. The foam front advanced steadily as bubbles filled each pore body (Figure 3.15). Small bubbles advanced much faster than larger bubbles (Figure 3.15). When pressure gradient reached steady-state, foam texture was investigated. Images were captured in the different sections between the injection port and the outlet. Section 1 had the greatest number of large bubbles, which advanced at a much lower velocity. Section 4 was affected by the converging flow into the produc-

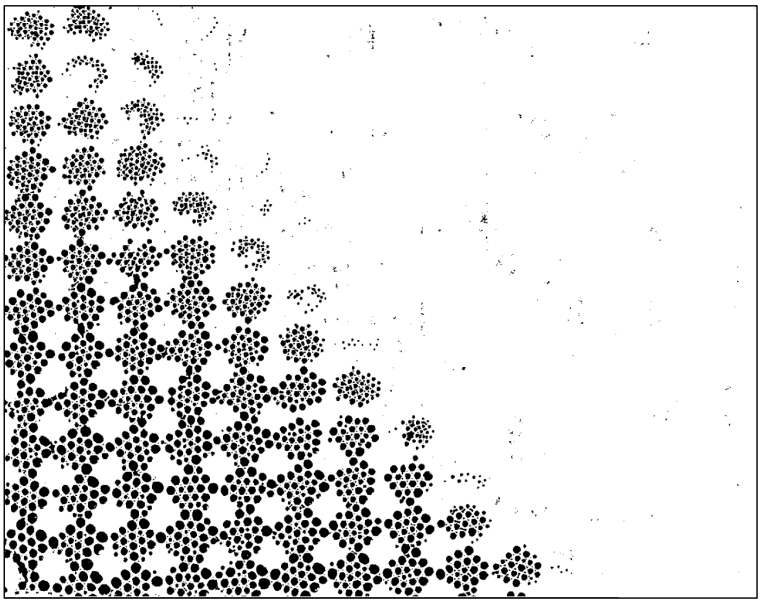

Figure 3.15: Foam texture near the advancing front of foam pre-generated using a 7-μm filter. 1.4×1.5 cm image of foam front (f_g =0.37). Flow is from left to right. The front has advanced further at the bottom of the image, but all along the front small bubbles advance ahead of larger ones.

tion port. The average foam bubble size in sections 2 and 3 is nearly the same (Figure 3.16 and Table 3.3).

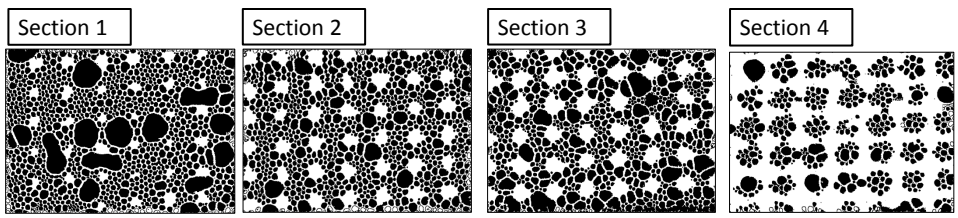

Figure 3.16: Foam texture versus distance f_g = 0.37, u_t=0.0021 m/s (black is gas and white is water). Images were captured during the stabilized pressure gradient. Image size 0.7×0.5 cm. Foam pre-generated using a 7-μm filter.

The 7-μm filter generates very fine foam; thus, we selected the 400 μm filter for the second pre-generated-foam experiment. We retained the same experimental conditions as the prevoius test. The model fracture was thorougly cleaned and saturated with water (no surfactant). Foam was injected at f_g = 0.37, u_t = 0.0021 m/s. The pre-generted foam contains bubbles much larger than the pores by the time foam reaches the fracture. The large pre-generated bubbles are sequezed into disk-like shapes in the reservoir upstream of the fracture (Figure 3.17). The large bubbles divide by capillary snap-off as they enter the fracture, and they occupy one or more pores. Analysis of images along the

Table 3.3: Image analysis statistics of the pre-generated foam using a 7-μm filter.

Section	1	2	3	4
Distance from inlet, mm	20	120	270	360
Average bubble size, mm^2	0.028	0.024	0.028	0.024
Bubble size, std. dev., mm^2	0.060	0.026	0.034	0.028
Number of bubbles per unit area	701	677	564	448

fracture (Figure 3.18) shows that average foam bubble size deceases as one moves downstream. Foam becomes finer due to snap-off as foam propgates forward. Consquently, the number of bubbles inceases 2.3-fold up to Section 3, excluding the possible effects of converging flow in Section 4 (Table 3.4).

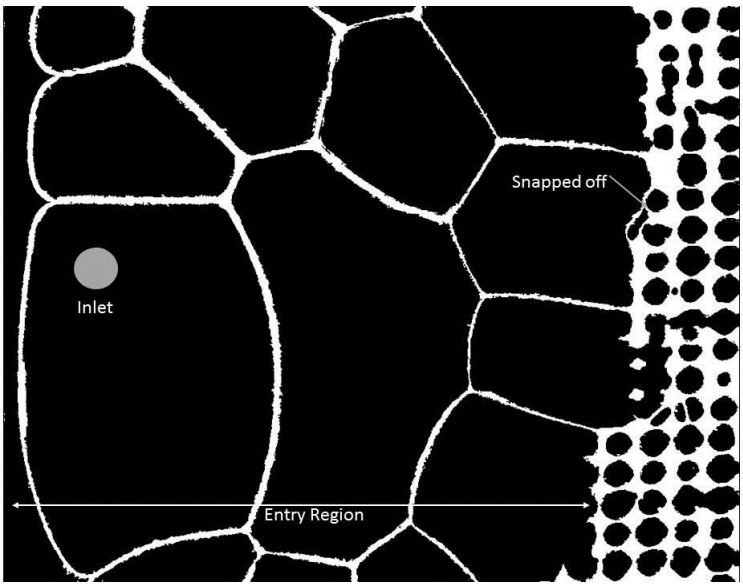

Figure 3.17: Image of the entry reservoir and entrance of the fracture for foam pre-generated using a 400-μm filter. Image size 2.0×1.6 cm. (f_g = 0.37, u_t=0.0021 m/s)

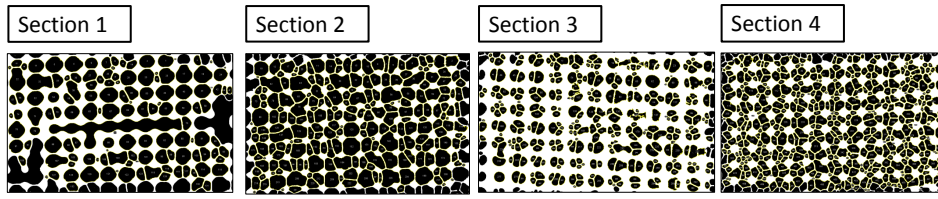

Figure 3.18: Foam texture vs distance, f_g = 0.37, u_t=0.0021 m/s. White is water while black is gas. Images captured during stabilized pressure gradient. Image size 1.21×0.75 cm. Foam pre-generated using a 400-μm filter

Table 3.4: Image analysis statistics of the pre-generated foam using a 400-μm filter.

Section	1	2	3	4
Distance from inlet, mm	20	120	270	360
Average bubble size, mm^2	0.343	0.250	0.107	0.100
Bubble size, std. dev., mm^2	0.439	0.175	0.072	0.068
Number of bubbles per unit area	132	227	305	486

Figure 3.19 compares foam apparent viscosity from all three tests. The apparaent viscosity of the in-situ-generated foam is comparable to the pre-generated foam. The model fracture continues to make the texture finer as foam propagates downstream. The model fracture is expected to make finer-textured foam until generation and destruction mechanisms are at equilibrum. We have not reached the final foam equlibirum state in the case of in-situ-generated foam. However, since the properties of the fine-textured pre-generated foam and in-situ generated foam are converging toward each other, we contend that steady-state texture is likely within this range.

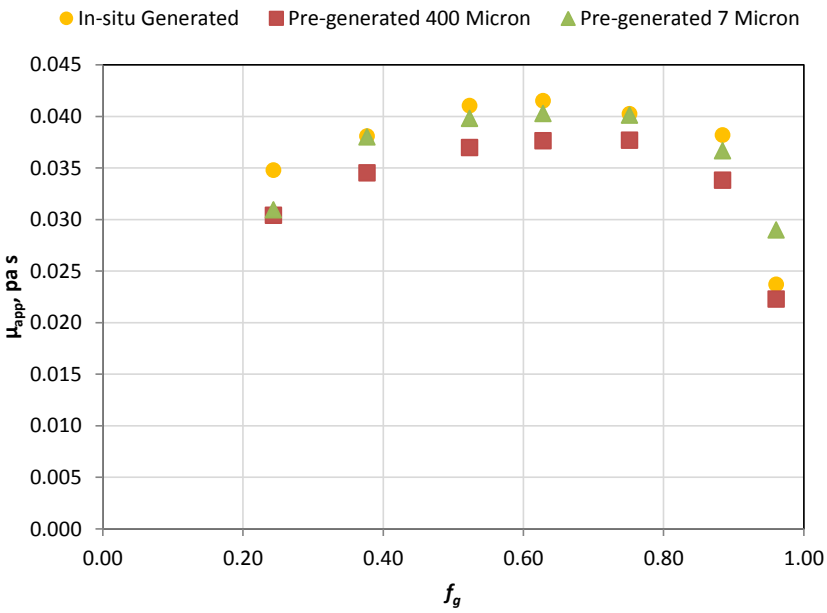

Figure 3.19: Foam apparent viscosity as a function of foam quality at u_t=0.0021 m/s of in-situ and pre-generated foams. The standard deviations of foam apparent viscosity are approximately 0.0009 and 0.01 pa. s at low quality and high quality, respectively.

3.7. SUMMARY AND CONCLUSIONS

This is the first report of a larger study of foam in fractures for EOR using a variety of model fractures with different geometries (AlQuaimi and Rossen, 2017a). The following conclusions can be drawn:

- Foam was generated in this 40×10 cm model fracture mainly by capillary snap-off: fracture-wall roughness played a major role in foam generation. Snap-off is less dominant at high injected gas fraction (f_g).
- Lamella division was observed at high f_g at two different total superficial velocities.
- Bubbles smaller than the pores were generated and propagated through the fracture. This depends in part on the geometry of the pore throats. Slit-shaped throats can give bubbles much smaller than pore bodies. The size of the bubbles is not always similar to the size of the pores because bubbles reside in the pore for a time that is much shorter than the time required for diffusion to eliminate smaller bubbles.
- For in-situ-generated foam, the pressure gradient correlates inversely with the average size of the bubbles.

- Oscillations in pressure gradient were observed at high f_g due to reduced and fluctuating foam generation. Similar oscillations are observed in 3D matrix porous-media, but in that case are due to bubble destruction at the limiting capillary pressure.
- This oscillation is also evident in the bubble sizes; bubble-size standard deviation increases as f_g increases.
- Foam may not have reached final local equilibrium within the length of our apparatus but we contend that it is bounded between the results for fine-textured pre-generated foam and in-situ-generated foam.

4

CHARACTERIZING FOAM FLOW IN FRACTURES FOR ENHANCED OIL RECOVERY

GAS is used in displacing oil for enhanced oil recovery projects because of its high microscopic-displacement efficiency. However, the process at the reservoir scale suffers from poor sweep efficiency due to density and viscosity differences compared to in-situ fluids. Foam substantially reduces the viscosity of injected gas and hence improves the sweep. Foam rheology in 3D geological porous media has been characterized both theoretically and experimentally. In contrast, the knowledge of foam flow in fractured porous media is far less complete.

In Chapter 3, we focused on foam generation and propagation in a fully characterized model fracture. Here we focus on foam rheology in the same model fracture. This investigation is conducted by varying superficial velocities of gas and surfactant solution. We find in this model fracture the same two foam-flow regimes central to the understanding of foam in 3D porous media: a low-quality regime where pressure gradient is independent of liquid velocity and a high-quality regime where pressure gradient is independent of gas velocity. The transition between regimes is less abrupt than in 3D porous media. Direct observation of bubble size, bubble trapping and mobilization, and foam stability as functions of superficial velocities allows comparison with our understanding of the mechanisms behind the two flow regimes in 3D porous media. Additionally, foam is shear-thinning in both regimes. But in other important respects the mechanisms thought to be behind the two flow regimes in 3D media do not appear in our model fracture. Foam is not at the limit of stability in the high-quality regime. Mobility in the

This chapter is based on (1) AlQuaimi, B. I., and Rossen, W. R. (2017). Characterizing Foam Flow in Fractures for Enhanced Oil Recovery. Paper presented at the 19th European Symposium on Improved Oil Recovery, Stavanger, Norway., (2) AlQuaimi, B. I., and Rossen, W. R. (2017). Characterizing Foam Flow in Fractures for Enhanced Oil Recovery. Submitted to the Journal of Petroleum Science and Engineering.

high-quality regime, instead, reflects reduced and fluctuating foam generation at high foam quality. Moreover, bubble size is not fixed at approximately pore size, the mechanism thought to control the low-quality regime in 3D porous media. Instead, bubbles are much smaller than pores. Finally, for this model fracture, the investigation of vertical flow reaches the same findings as for horizontal flow, with somewhat lower pressure gradient.

4.1. INTRODUCTION

Underground reservoirs that include natural fractures impose additional challenges for enhanced oil recovery (EOR) projects. The challenges are encountered because of the presence of highly conductive fractures or fissures (Allan and Sun, 2003). Injected fluids designed to recover un-displaced oil flow rapidly in the fractures, reducing the efficiency of the process. Foam greatly reduces gas mobility and hence allows gas to encounter more oil (Fjelde et al., 2008; Haugen et al., 2014; Steinsbø et al., 2015). Numerous studies have characterized foam rheology in 3D geological porous media, both theoretically and experimentally, but far fewer for fractured porous media.

Chapter 3 reviews previous research on foam generation in model fractures. Here we focus on the findings of those studies on foam rheology in fractures and the mechanisms behind it.

Kovscek et al. (1995) investigated nitrogen, water and aqueous foam flow through two transparent replicas of natural rough-walled rock fractures with hydraulic apertures of both roughly 30 μm and 100 μm. Radial-flow tests were done on these fractures, with a diameter of 12 cm. The total flow rate of nitrogen ranged from 1-100 standard cm^3/min, which is equivalent to 0.0014-0.147 m/s, at the outer radius. They concluded that the rheology of foam in fractures is complicated. At gas fractional flows, i.e. foam qualities, above 0.97 the pressure drop was proportional to the liquid flow rate at a fixed gas flow rate. For gas fractional flows below approximately 0.9, the pressure drop was insensitive to the liquid flow rate. At intermediate gas fractional flow, the pressure drop decreased with increasing liquid flow rate. These results would be consistent with the two flow regimes identified in 3D porous media (Alvarez et al., 2001).

Buchgraber et al. (2012) experimentally investigated the behavior of pre-generated foam in fractures at various foam qualities and fluid velocities. The experiments were conducted in fractures etched on 2×5 cm silicon chips. The first experiment was done in smooth channels with apertures of 40 and 30 μm. The second experiment was conducted in a smooth slit with apertures of 20 and 40 μm arranged in a checkerboard pattern. The third experiment was done on a uniform-aperture channel with a rough face. The gas superficial velocity ranged from 7.23×10^{-6}-0.0057 m/s and the liquid superficial velocity ranged from 2.89×10^{-5}-0.0017 m/s. Low- and high-quality regimes were identified. These explained the low pressure gradient observed in the high-quality regime as the result of coalescence of foam.

Fernø et al. (2016) reported a study of foam flow behavior in a fractured rock slab 31.2

cm long. The total superficial velocities used were 0.0003, 0.001, 0.0017 and 0.0028 m/s. Increased pressure gradient was observed at increased foam quality, for a given total flow rate. At high foam quality the pressure gradient suddenly dropped. They explained this sudden decrease as the result of the dry conditions leading to foam coalescence.

In this study, we investigate the rheology of in-situ-generated foam in a well-characterized transparent model fracture. We compare the behavior of foam using four total superficial velocities (0.0011, 0.0021, 0.0030, and 0.0049 m/s) and foam qualities ranging from 23 to 97%. We measure the pressure difference across four sections along the fracture and capture images to explain the foam behavior.

4.2. FRACTURE PHYSICAL MODEL

The fracture apparatus and the model fracture were used previously to study foam generation and propagation in fractures; Chapter 3 and (AlQuaimi and Rossen, 2017d). The 40×10 cm model fracture consists of a roughened plate that represents fracture-wall roughness and a top plate that is smooth, to allow direct observation of the flow. The gap between the top plate and the rough surface represents the fracture aperture. The following details are relevant to the practicalities of this study of foam rheology. The two glass plates are glued together at the edges using Araldite® 2014, which is a two-component epoxy adhesive that has a tensile strength of 26 MPa at 23 °C. The 4 mm-thick roughened plate was strengthened by attaching a 15 mm-thick glass plate using ultraviolet light and DELO® Photobond® glue (DELO, Windach, Germany). The thickness of the top glass plate is 15 mm as well. The thickness of the glass was estimated based on solid-mechanics calculations to prevent any significant glass deflection during the flow. This is also checked using a Probe Indicator (2μm resolution) during the experiment. Four pressure ports are equally spaced over a length of 36 cm; the last port is also the fluid outlet. The fracture is mounted in a frame that could slide 50 cm in the X and Y directions to allow for microscopic observation of the flow in the whole 40×10 cm fracture. Further details can be found in Chapter 3.

The model fracture has been characterized in terms of average aperture and variability and correlation length of aperture, allowing its representation as a 2D porous medium with pore throats and bodies (Chapter 2). Using this characterization we previously combined the capillary number-residual saturation curve for a wide range of model fractures into a single relationship (Chapter 2; (AlQuaimi and Rossen, 2017a)). This study is part of a larger effort to examine foam behavior in a wide variety of model fractures and relate the behavior to dimensionless geometrical factors that can be applied to natural fractures in the field.

A full description of the model fracture geometry can be found in Chapter 3.

4.3. EXPERIMENTAL PROCEDURE

The same experimental setup described in Chapter 3 is used here. The pressure gradient in the first section is affected by the entry region and the last section by converging

flow towards the outlet (Figure 3.3). We therefore selected the third section on which to base our analysis of the pressure behavior in this paper. We averaged the pressure gradient over the period of stabilization for each foam quality. The hydraulic aperture of this model fracture is 66 μm.

The foam experiment starts by co-injecting a solution of 1.0 wt.% sodium C14-16 olefin sulfonate and nitrogen into the fully water-saturated fracture. The two fluids enter the model fracture at the entry region and flow into the fracture. In-situ foam generation is observed as discussed in Chapter 3. The pressure gradient is recorded until stabilization is reached. Figure 4.1 shows the evolution of the pressure gradient as the water initially present is displaced and foam is generated in our experiment. The test was conducted at a foam quality (f_g) of 37% and total superficial velocity of 0.0021 m/s. Oscillation in $|\nabla P|$ is observed in this test, and larger oscillation is evident at higher f_g. The injected gas volume is corrected to the pressure at the middle of the fracture. We performed foam-quality scans at fixed total superficial velocity (u_t). The pressure-gradient data were acquired in a non-uniform sequence to avoid any hysteresis that may occur in the case of sequential increase or decrease in f_g (Figure 4.2). The data points have numbers which indicate the sequence in which they were acquired. The error bars in the plot indicate the standard deviation of the measurement. Additionally, point 3 at f_g = 0.25 was repeated after displacing all the foam and starting the experiment again with only water in the fracture. This gives extra confidence in the measurement and the procedure followed to acquire the data. The oscillation in $|\nabla P|$ reflects fluctuation in foam generation, as discussed below.

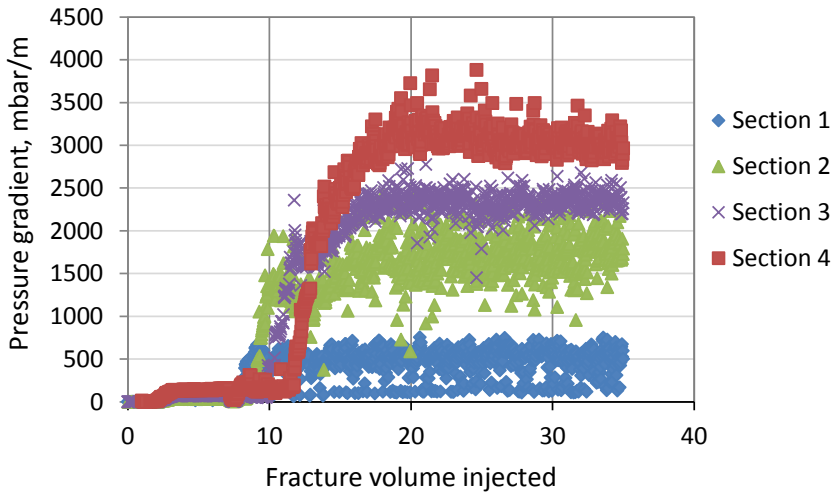

Figure 4.1: Pressure gradient during a foam-injection test at a foam quality of 37%

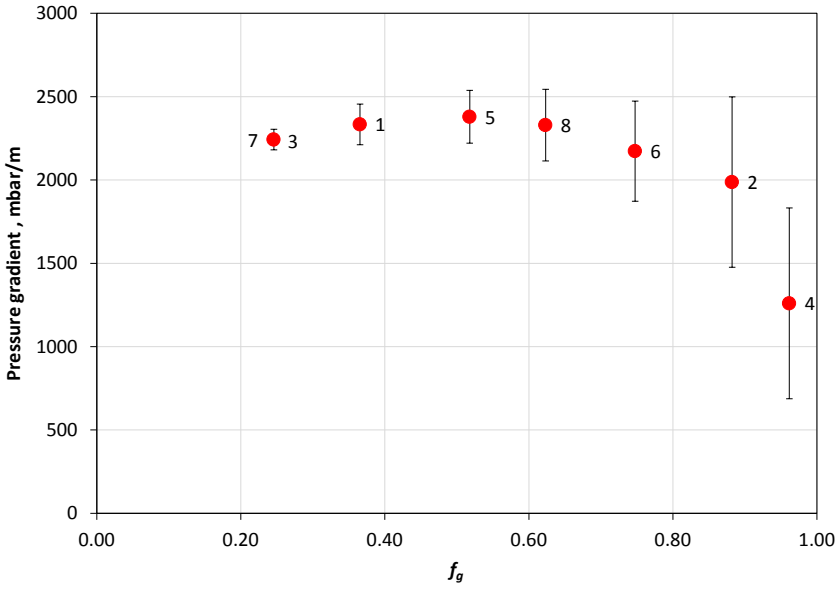

Figure 4.2: Foam-quality scan (pressure-gradient as a function of foam quality f_g) at total superficial velocity u_t = 0.0021 m/s.

4.4. EXPERIMENTAL RESULTS

We tested four total superficial velocities u_t, 0.0010, 0.0021, 0.0030, and 0.0049 m/s (Figure 4.3). As the velocity increases the pressure gradient increases; however, the increase is not proportional to u_t. At a total superficial velocity of 0.0010 m/s, the lowest f_g that can be achieved within the limits of our gas mass-flow meter/mass-flow controller is 0.38. We used Equation (3.1) to estimate foam apparent viscosity in these four tests (Figure 4.3). The largest mobility reduction is achieved at a velocity of 0.0010 m/s. A mobility reduction by a factor of 67 relative to that of water in single-phase flow is estimated at f_g of 0.53. If we estimate the mobility reduction to the gas phase alone, this estimate would be much larger. Figure 4.4 indicates that foam is shear-thinning and Figure 4.5 shows that foam apparent viscosity is shear-thinning with respect to superficial velocity, with an average exponent of approximately (-0.82). Represented as a power law fluid (Bird, 2002), this corresponds to a power law exponent n= 0.18. Previous studies (Kovscek et al., 1995; Fernø et al., 2016) also found shear-thinning rheology in the model of a real fracture.

Central to the understanding of flow in 3D porous media is the existence of two distinct foam-flow regimes, corresponding to high foam quality and low foam quality (Osterloh and Jante, 1992; Alvarez et al., 2001). Pressure gradient is independent of liquid velocity in the low-quality regime and independent of gas velocity in the high-quality

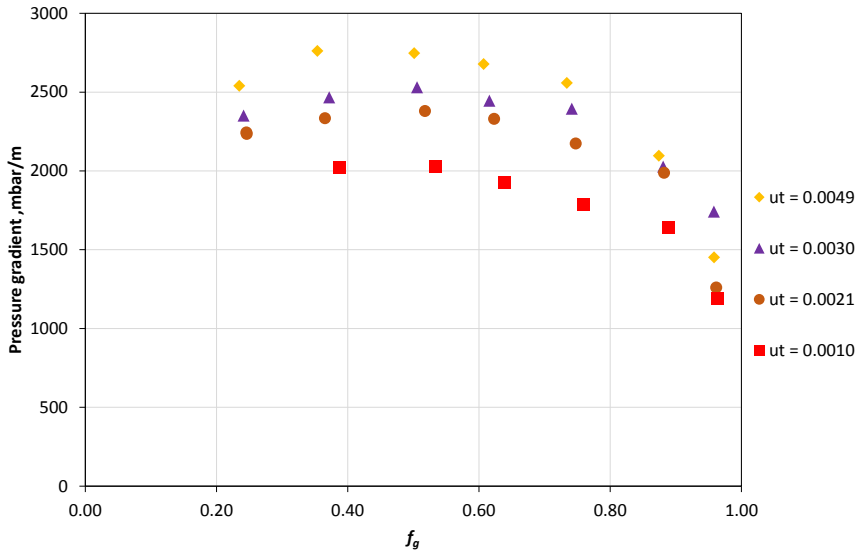

Figure 4.3: Foam-quality scan at different total superficial velocities (m/s). The standard deviations of foam pressure-gradient data are approximately 60 and 570 mbar/m at low quality and high quality, respectively. They are not drawn to avoid clutter in the diagram.

regime. We investigated the existence of these two flow regimes in our model fracture. The pressure-gradient data were plotted using a Julia (open source programming language, julialang.org) script, to construct a contour plot from the data. The plot shows the existence of two flow regimes in the fracture similar to those in 3D porous media (Figure 4.6). Figure 4.6 reveals a broader transition between the two qualities than usually seen in 3D porous media. The explanation for pressure-gradient behavior in the high-quality regime in 3D porous media is that foam collapse at the limiting capillary pressure (P_c^*) controls bubble size and therefore gas mobility (Khatib et al., 1988). In the low-quality regime, bubble size is thought to be unchanging at approximately pore size, and pressure gradient depends on porous medium and surface tension, but not on the ability of the surfactant to stabilize foam (Rossen and Wang, 1999). The transition between regimes is sensitive to both the nature of the porous medium and ability of the surfactant to stabilize foam (Alvarez et al., 2001).

In our model fracture, we observe different phenomena controlling the two flow regimes from those believed to operate in 3D porous media. Several images were captured and analysed using ImageJ, an image-processing and analysis software. We developed a procedure for the analysis of the images using image thresholding to detect the boundaries of the foam bubbles and determine bubble sizes. At high foam quality, we see reduced and fluctuating foam generation, but steady foam generation at low quality. At high foam quality, fine-textured foam is generated and propagates, followed by a slug of gas that is

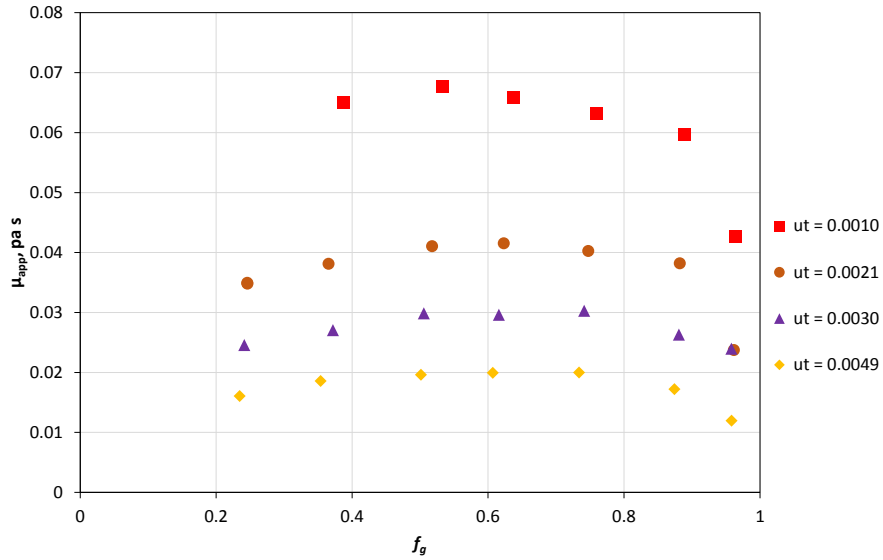

Figure 4.4: Foam apparent viscosity as a function of foam quality at different total superficial velocities.

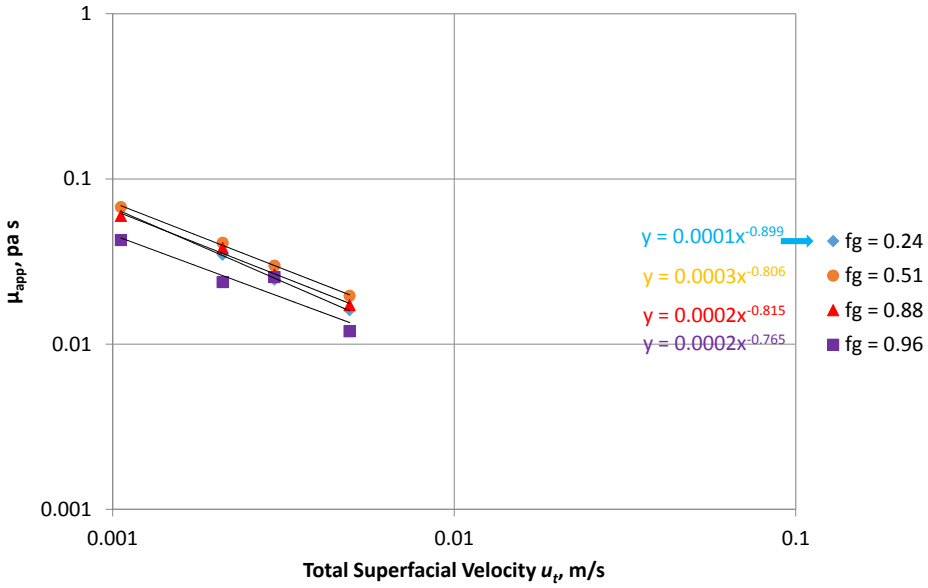

Figure 4.5: Foam apparent viscosity as a function of total superficial velocity.

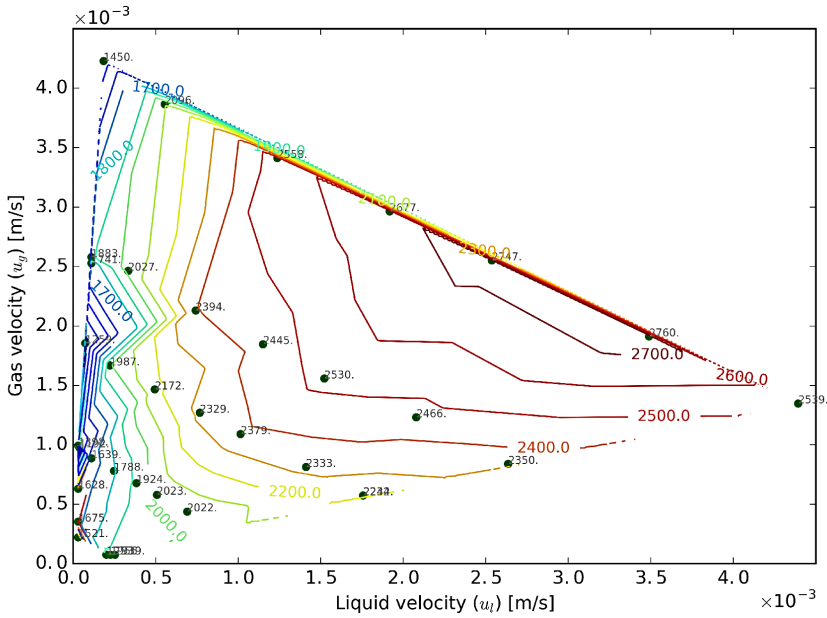

Figure 4.6: Pressure gradient (mbar/m) as a function of superficial velocities of gas and liquid; existence of two flow regimes in fracture.

refined as it propagates (Figure 4.7). This causes the pressure response to fluctuate and hence reduces time-average foam apparent viscosity. Figure 4.7 shows the time interval between the individual gas slugs at u_t = 0.0030 m/s and f_g = 0.90. The length of the gas slug and its velocity increase as f_g increases (Figure 4.8). Figure 4.8 illustrates that the time interval between the gas slugs is much shorter and the size of the gas slugs is much larger than in the previous case, such that a similarly enlarged image as that on the right of Figure 4.7 would be completely occupied by the slug. The pressure-gradient data correlate well with this observation. At steady state, we tracked the pressure behavior as the slug propagates downstream using the pressure sensors spaced over the entire length of the fracture at u_t = 0.0030 m/s and f_g = 0.96 (Figure 4.9). The pressure decreases sequentially as the slug arrives to the section and increases as the fine-textured foam behind it reaches the section. At low foam quality, foam is generated mainly by capillary snap-off and the average bubble size remains constant at a size less than pore size (Figure 4.10). Kovscek et al. (1995) reported behavior consistent with the high- and low-quality flow regimes in a model fracture. Buchgraber et al. (2012) report observing the two flow regimes in a microfluidic devices and ascribe the high-quality regime to foam coalescence of high foam quality.

Three low foam qualities f_g, 0.24, 0.38 and 0.51, are used to investigate foam texture at different u_t. The pressure gradient, as shown in Figure 4.3, increases as u_t increases at a fixed f_g. However, we find that for the these values of u_t the average bubble size does

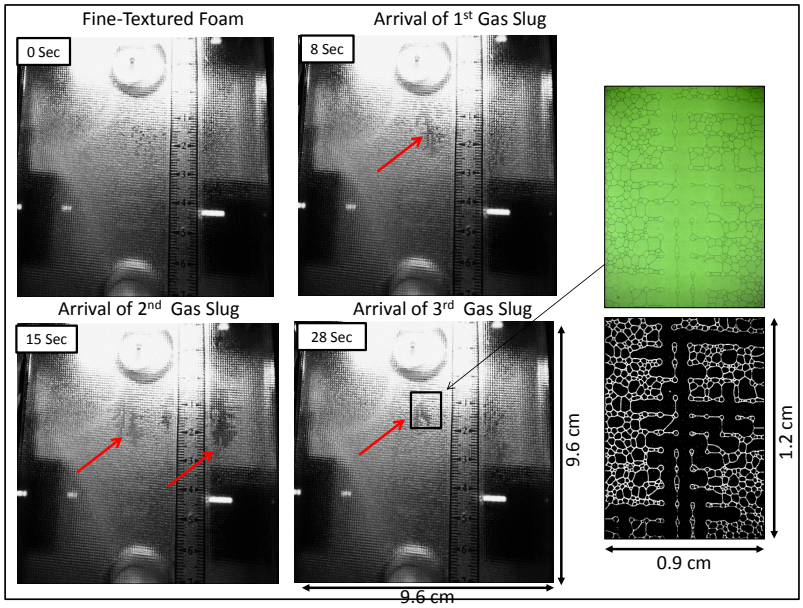

Figure 4.7: Time-lapse images of reduced and fluctuating foam generation. The enlarged images at right show a gas slug. (This binary image is the processed version: black is gas and white represents foam films (lamellae.) Total superficial velocity u_t = 0.0030 m/s and f_g = 0.90. Flow is from the top of the image to the bottom; the fracture itself is horizontal.

not change greatly at fixed f_g (Figures 4.11, 4.12, and 4.13). It is thought that average bubble size does not change in the low-quality foam regime in 3D porous media (Rossen and Wang, 1999; Alvarez et al., 2001). Bubbles are thought to be as large as pores in that regime. The near-invariance of bubble size in figures 4.11 to 4.13 is consistent with these findings, but bubbles are smaller than pores. Appendix F shows the same findings on a random rough sample. It is possible that bubbles reflect a characteristic size for snap-off in the throats rather than the pore-body size. Pore throats in this model are 5-10 times as wide across as the aperture (Table 3.1, Figure 3.1), a slit-shaped geometry that favors snap-off (Rossen, 1996). The error bar on the average bubble size represents the standard deviation of bubble-size distribution.

4.5. VERTICAL FLOW EXPERIMENT

We modified the experimental setup to study the effect of gravity on foam flow. The model fracture was oriented vertically such that gas and surfactant solutions are injected from the bottom. The other experimental conditions were held constant. We conducted a foam-quality scan at u_t = 0.0010 m/s (Figure 4.14). The comparison between vertical flow with horizontal flow shows a somewhat lower pressure gradient during vertical flow. The difference is approximately 100 mbar per meter, the difference between potential gradients for gas and liquid. We performed four foam-quality scans with four total

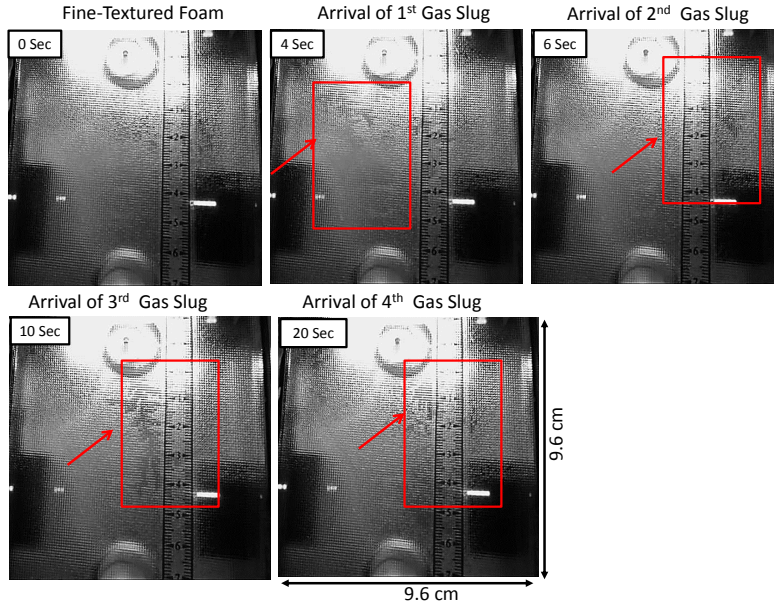

Figure 4.8: Time-lapse images show reduced and fluctuating foam generation. Total superficial velocity u_t = 0.0030 m/s and f_g = 0.96. Flow is from the top of the image to the bottom.

superficial velocities u_t. The tested velocities are 0.0010, 0.0021, 0.0030, and 0.0049 m/s (Figure 4.15). Similarly, we used Equation (3.3) to estimate foam apparent viscosity in these four tests (Figure 4.16). The largest mobility reduction is achieved in these tests at a velocity of 0.0010 m/s.

The pressure-gradient data were plotted to construct a contour plot, which shows again the existence of two flow regimes during vertical flow (Figure 4.17). The observed behavior during vertical flow shows the same flow characteristics discussed above.

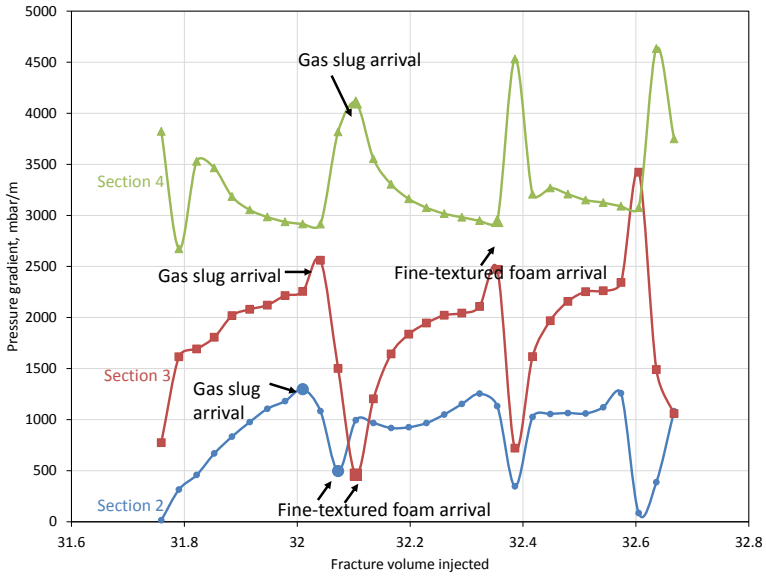

Figure 4.9: Pressure gradient in three sections of the fracture during coinjection of gas and liquid $u_t = 0.0010$ m/s and $f_g = 0.88$. The pressure gradient increases as fine-textured foam behind the slug reaches the section. The curves connect the points to guide the reader's eye.

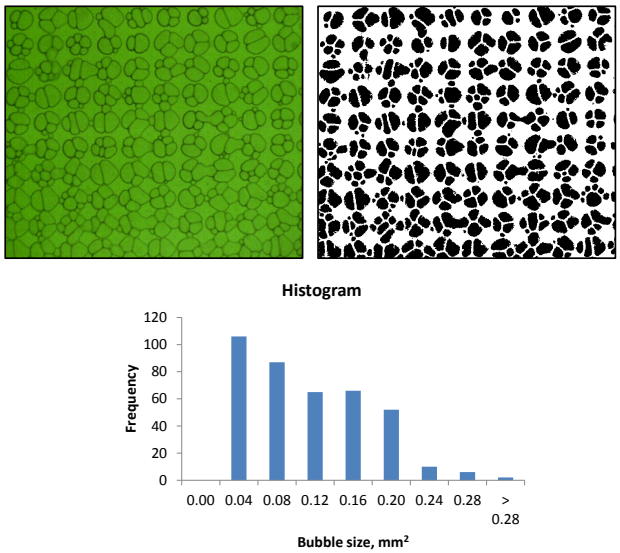

Figure 4.10: Image (0.97×0.82 cm) taken at low foam quality, $u_t = 0.0010$ m/s and $f_g = 0.38$, and the binary version of it (top). Black is gas and white is water. The histogram shows the bubble-size distribution.

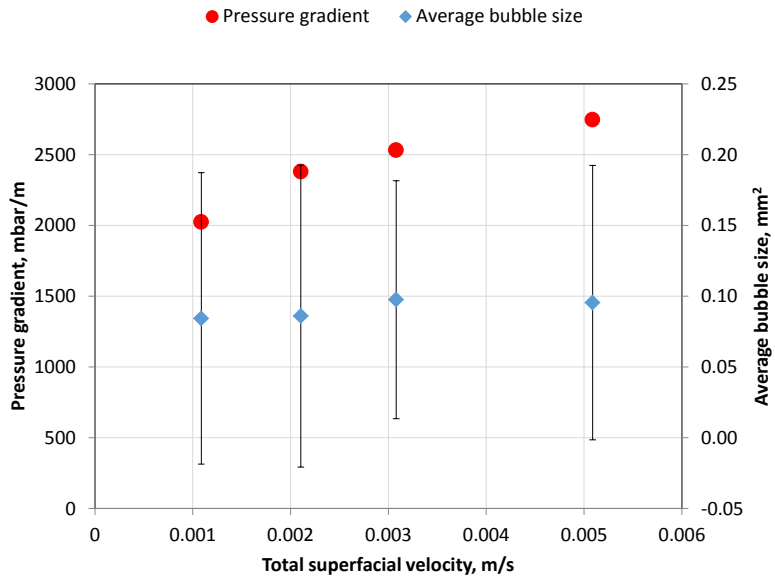

Figure 4.11: Pressure gradient and average bubble size versus u_t at $f_g = 0.51$.

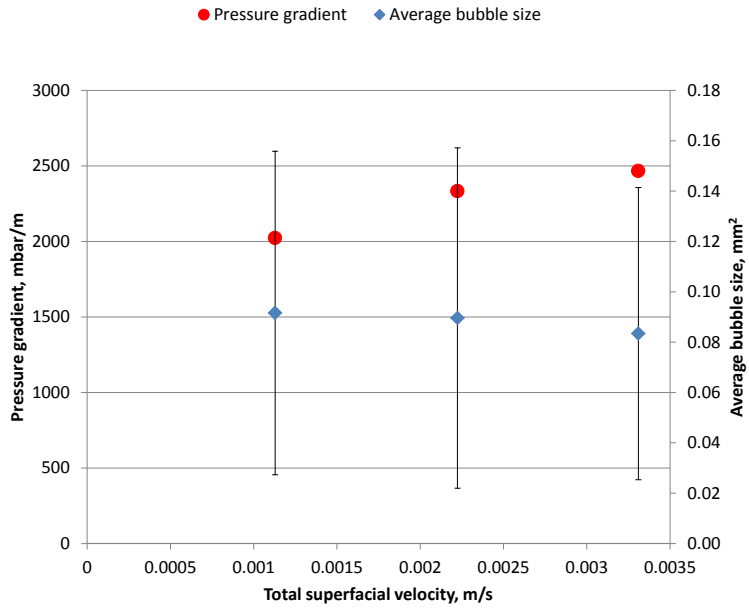

Figure 4.12: Pressure gradient and average bubble size versus u_t at $f_g = 0.38$.

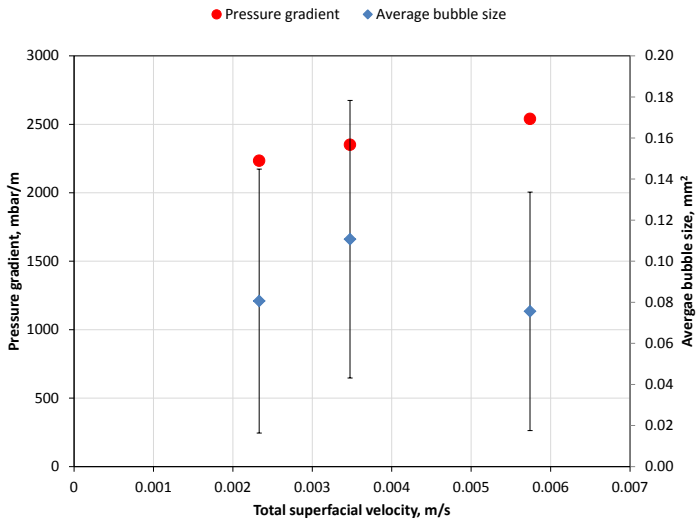

Figure 4.13: Pressure gradient and average bubble size versus u_t at $f_g = 0.24$.

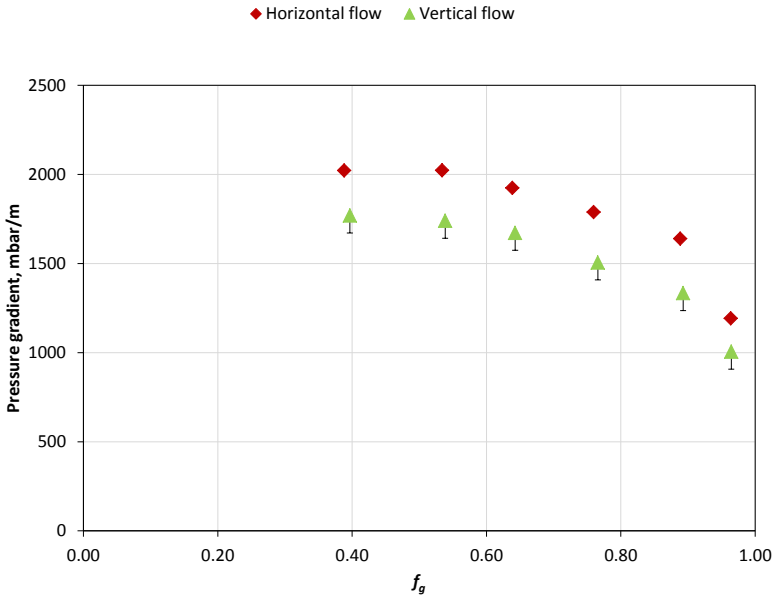

Figure 4.14: Comparison between vertical flow and horizontal flow at $u_t = 0.0010$ m/s. Comparison between vertical flow and horizontal flow at $u_t = 0.0010$ m/s. The error bars for vertical flow represent the effect of gravity on the liquid flow potential.

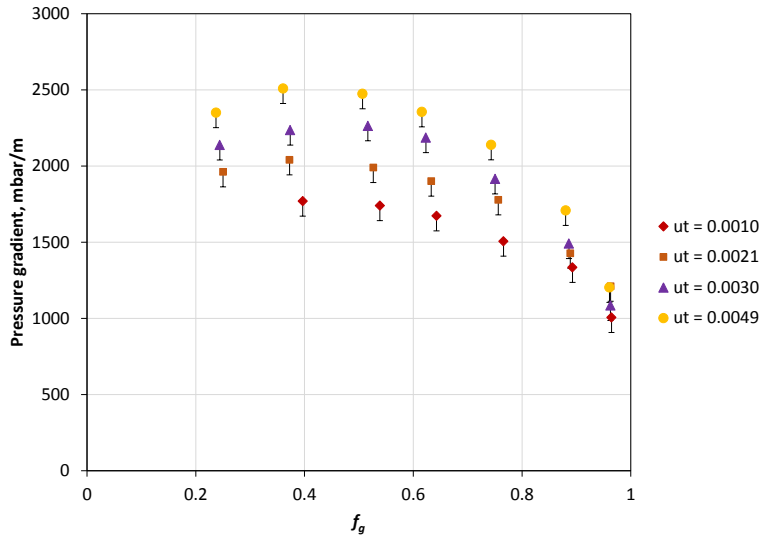

Figure 4.15: Foam-quality scan at different total superficial velocities (m/s) during vertical flow. The error bars represent the effect of gravity on the liquid flow potential, i.e., the difference from the values measured in horizontal flow.

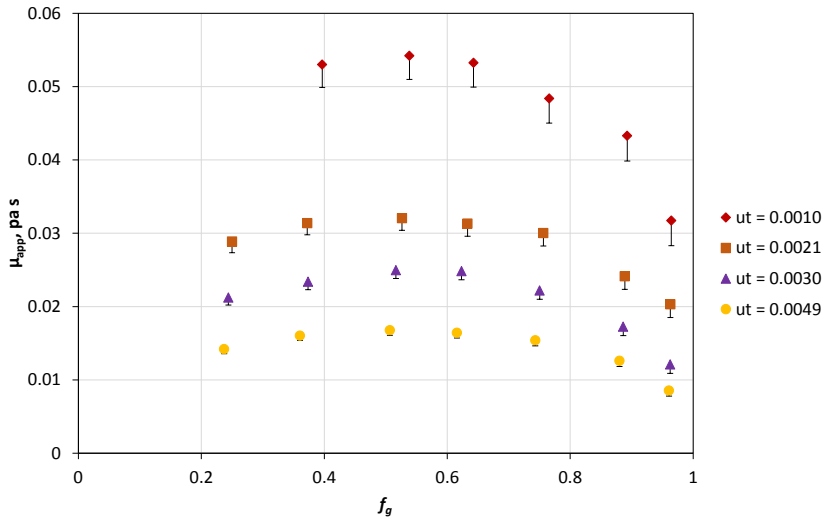

Figure 4.16: Foam apparent viscosity at different total superficial velocities during vertical flow. The error bars represent the effect of gravity on the liquid flow potential.

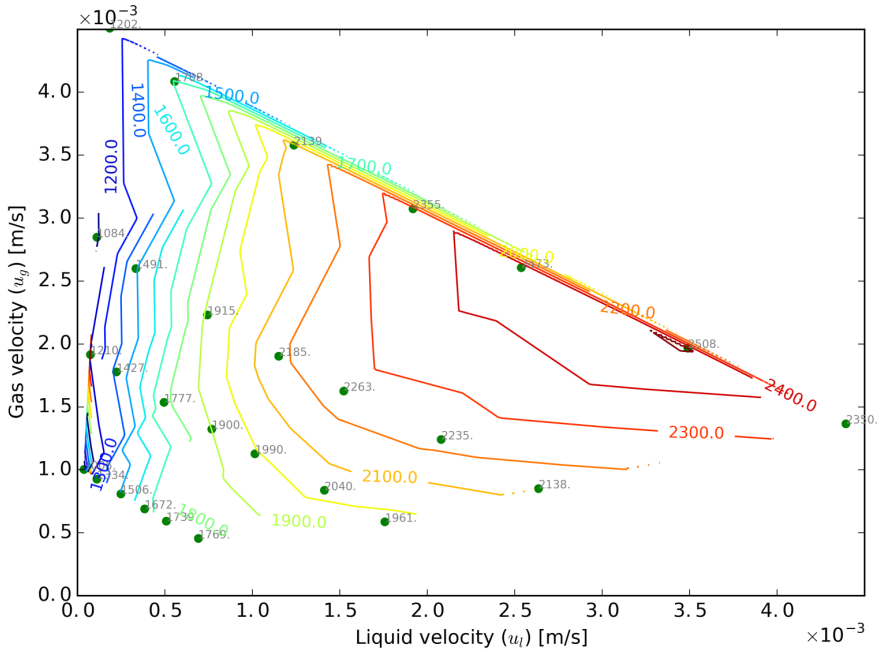

Figure 4.17: Pressure gradient (mbar/m) as a function of superficial velocities of gas and liquid in vertical flow; existence of two flow regimes in the fractures.

4.6. SUMMARY AND CONCLUSIONS

The following conclusions can be drawn from our experimental investigation of foam rheology in a model fracture:

- The pressure gradient increased with increasing total superficial velocity of the foam injection, but the increase in pressure gradient was not proportional to superficial velocity. Instead it reflects shear-thinning behavior, with an average exponent of approximately (-0.82) (apparent power-law-fluid exponent n = 0.18).
- The pressure-gradient data for in-situ generated foam reveals the existence of two foam-flow regimes, i.e. high- and low-quality regimes, as seen in 3D porous media.
- These two foam-flow regimes were observed during horizontal flow and vertical flow. Somewhat lower pressure gradient was recorded in vertical flow, however.
- In our experiments, the high-quality regime is evidently the result of reduced and fluctuating foam generation, not foam collapse at the limiting capillary pressure. The pressure-gradient data correlates well with the propagation of gas slugs downstream and hence confirms this finding of fluctuating foam generation at high f_g.
- For three low foam qualities, the images at different superficial velocities show no significant change in average bubble size with superficial velocity, but the bubbles are smaller than pores. It is possible that the bubble size reflects a characteristic size for snap-off in the throats.

5

FOAM GENERATION AND RHEOLOGY IN A VARIETY OF MODEL FRACTURES

GAS is used in petroleum reservoirs to displace oil for enhanced oil recovery. The microscopic displacement efficiency of gas is very good, but at the reservoir scale the process suffers from poor sweep efficiency, especially in naturally fractured reservoirs. Foam can improve the sweep.

There have been considerable scientific contributions towards understanding foam flow in nonfractured porous media, with relatively little work on foam flow in fractured porous media. We investigate foam-generation mechanisms in five fully characterized model fractures with different apertures and correlation lengths of the aperture distribution. We also study the rheology of the in-situ-generated foam by varying the superficial velocities of the gas and surfactant solution. We compare the measured pressure gradient against the fracture attributes, aperture and the correlation length of the aperture. We also compare foam texture as a function of position within the fracture as the generated foam propagates through the fracture.

Gas mobility was greatly reduced as a result of in-situ foam generation in our model fractures. Foam was generated predominantly by capillary snap-off and lamella division. The measured mobility reduction depends on fracture attributes. Fracture-wall roughness, represented by both the hydraulic aperture and the correlation length of the aperture, plays an important role in foam generation and mobility. Two model fractures show the same two foam-flow regimes central to the understanding of foam in nonfractured porous media: a low-quality regime where pressure gradient is independent of

This chapter is based on AlQuaimi, B. I., and Rossen, W. R. (2017). Foam Generation and Rheology in a Variety of Model Fractures. Submitted to the Journal of Energy & Fuels.

liquid velocity and a high-quality regime where pressure gradient is independent of gas velocity. Average bubble size increases as the aperture increases, which results in a significant decrease in pressure gradient.

5.1. INTRODUCTION

Foam is injected to recover the undisplaced oil in petroleum reservoirs. Foam has been applied in the field from as early as the 1960s (Holm, 1970). A foam pilot test was conducted in the Snorre Field, starting with laboratory experiments and numerical simulations (Svorstol et al., 1995a,b; Blaker et al., 2002). Patzek (1996) reported the experience and the benefits of steam-foam injection in many field applications. Foam is also used in acid diversion for selective stimulation (Nasr-El-Din et al., 2006; Kam et al., 2007). Szafranski et al. (1998) used foam for the remediation of an aquifer.

Many petroleum reservoirs have natural fractures caused by earth stresses (Nelson, 2001). Natural fractures vary in aperture, length, orientation, asperities and wall roughness (van Golf-Racht, 1982; Bertotti et al., 2005; Ozkaya, 2007). Studies have examined foam flow in fractures in the last two decades. Pre-generated foam was injected into sawed rock core samples or blocks to study oil recovery (Haugen et al., 2012, 2014; Steinsbø et al., 2015). Yan et al. (2006) injected pre-generated foam in parallel slits to study sweep and foam rheology. Studies of pre-generated foam in microfluidics as an approximation to fracture flow have also been reported by Buchgraber et al. (2012) and Gauteplass et al. (2015). Kovscek et al. (1995) investigated foam flow in fracture replicas with apertures of roughly 30 and 100 μm. Fernø et al. (2016) studied foam generation and sweep efficiency in a fractured rock slab with aperture of approximately 100-150 μm. These studies reported the pressure gradient across the entire sample, so it is not possible to know foam texture or pressure behavior as foam propagates through the sample. Moreover, most studies involved the injection of pre-generated foam. AlQuaimi and Rossen (2017d) studied in-situ foam generation and propagation in a physical-model fracture, and reported foam texture and pressure gradient versus distance from the injection face. This chapter shows the results of in-situ foam generation in five distinct model fractures. The fracture varies in aperture and correlation length of the aperture. The study also addresses foam texture as a function of roughness scale and aperture variation. In addition, it shows the effect of fracture aperture on foam texture and pressure gradient.

5.2. DESCRIPTION OF MODEL FRACTURES

Model fractures made of glass plates have previously been used to study foam and two-phase flow in fractures (Pruess and Tsang, 1990; Fourar et al., 1992; Pieters and Graves, 1994; Chen et al., 2004a,b; Yan et al., 2006; Qian et al., 2011; AlQuaimi and Rossen, 2017b). Glass-model fractures provide the ability to observe the flow and investigate the mechanisms of foam generation. More importantly, it allows one to systematically vary roughness scales (magnitude of aperture, aperture variation and the length scale over which the aperture varies) and investigate the effect of these on foam generation, stability and mobility. Our goal is to cover a wide range of apertures and different fracture geometries encountered in fractured reservoirs. Figures 5.1, 5.2, 5.3, 5.4, and 5.5 show the fracture-

wall surface topography of our model fractures.

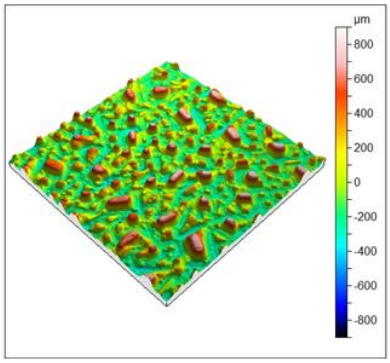

Figure 5.1: Sample 1 3D surface topography. The patch shown is 4×4 cm.

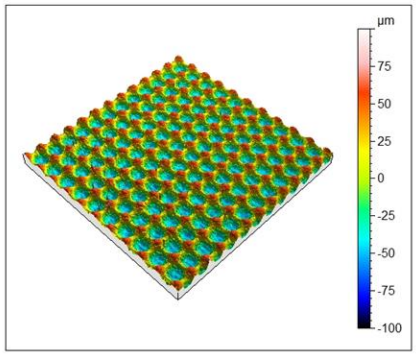

Figure 5.2: Sample 2 3D surface. The patch shown is 1×1 cm.

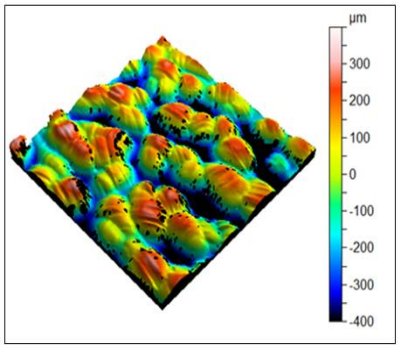

Figure 5.3: Sample 3 3D surface topography. The patch shown is 4×4 cm.

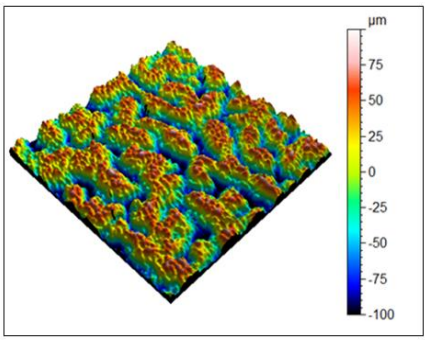

Figure 5.4: Sample 4 3D surface topography. The patch shown is 4×4 cm.

The model fractures, examined here, consist of a roughened plate to represent the fracture roughness and a top plate that is smooth, to allow direct observation of the flow. One model fracture has a 40×10 cm plate with regular patterns in its roughness. The remaining four model fractures have 43×10 cm plates with significant differences between them in their roughness scales. The roughened plate is 4 mm thick and was strengthened by attaching a 15 mm-thick plate of glass using DELO®-Photobond® glue (DELO, Windach, Germany). The thickness of the top glass plate was also 15 mm. The required thickness of the glass plates was estimated using solid-mechanics calculations to prevent any glass deflection during the flow. The glass deflection was also checked using a Probe Indicator (2 µm resolution) during the experiment.

The design details of the regular-pattern model fracture (Sample 2) were reported by

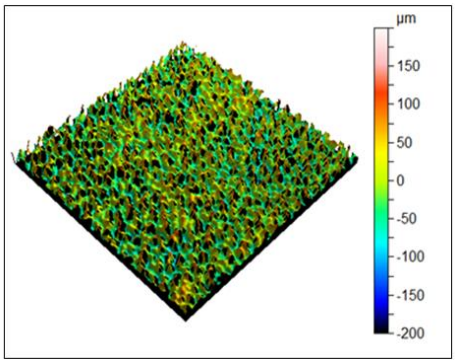

Figure 5.5: Sample 5 3D surface topography. The patch shown is 4×4 cm.

AlQuaimi and Rossen (2017b). The other four model fractures have roughened glass plates that include three inlet ports that allow a separate co-injection of gas and liquid. These inlet ports are equally spaced and connected to an 8.0×2.0×0.04 cm entry region milled into the roughened plate (see Figure 6, bottom right). Sample 2 has a single port for outflow without a milled outlet region. The milled outlet region in the other four samples eliminates radial converging flow to the single outlet port we observed in Sample 2. For these four samples, the fourth pressure port is located 2 cm upstream of the outlet. Thus behavior in the fourth section, between taps 3 and 4, is relatively isolated from the capillary end effect at the edge of the fracture. The middle inlet port was used for liquid injection and the other two inlet ports for gas injection. The roughened glass plate includes four pressure ports spaced over a length of 39 cm and an 8.0×2.0×0.04 cm milled outlet region (see Figure 6, bottom right). The gap between the top plate and the rough surface represents the fracture aperture. The two glass plates are glued together using Araldite® 2014, an epoxy adhesive that has a tensile strength of 26 MPa at 23°C. The fracture is mounted in a frame that can slide 50 cm in X and Y directions to allow for microscopic observation of the flow in the whole 43×10 cm fracture.

A fracture can be considered a two-dimensional network of pore bodies (maxima in aperture) connected by throats (saddle points between pore bodies) (Tsang, 1984; Pyrak-Nolte et al., 1988; Rossen and Kumar, 1992; Hughes and Blunt, 2001). To characterize the two-dimensional network, a 4×4 cm patch of each roughened glass sample was profiled to quantify the spatial and vertical variations in height. Appendix A show the images and the statistics of the pore throats and pore bodies. We identify the characteristic pore-throat aperture (d_t) as that at the percolation threshold, a characteristic pore-body aperture (d_b) that is the average pore-body aperture, and a characteristic pore length (L_p) that is the average pore-body length of the 2D network in the flow direction. A separate measure would be the correlation length of aperture. Table 5.1 shows that these two measures correlate well with each other. The hydraulic aperture is measured experimentally by injecting water and obtaining the flow rate-pressure drop relationship:

details are in AlQuaimi and Rossen (2017a). Table 5.1 summarizes the fracture-aperture data for all five fractures. The model fracture topography with the conceptual 2D network superimposed on the images is given in Appendix A.

Samples 4a, 4b, 5a and 5b were fabricated to investigate the effect of d_H at a fixed L_p. The model fractures were fabricated from glass plates similar to samples 4 and 5, but with spacers with known thickness (and dimensions 0.5 × 0.5 cm) distributed uniformly mainly over the fracture perimeter. The spacers occupy only 0.01% of the total area available for flow. We measured the hydraulic aperture experimentally after fabrication.

5.3. EXPERIMENTAL SETUP

The experimental setup is described in chapter 3 and 4. Here we used low ranges of the same pressure sensors.

Four sets of experiments were carried out using this setup, after measuring experimentally the hydraulic aperture of each fracture:

1. In-situ Foam Generation : The fracture was first vacuum-saturated with water (no surfactant), followed by co-injection of gas and a surfactant solution. The foam-generation mechanisms within each of the fractures were observed and categorized.

2. Foam Propagation : Once the foam had been generated, its behavior and evolution as it propagates through the model was investigated.

3. Foam Quality Scan : After foam flow had been established throughout the fracture, the pressure gradient across the four sections was recorded until a stable signal was observed. The variation in the pressure gradient with foam quality, while holding total superficial velocity u_t constant, could then be recorded.

5.4. RESULTS

5.4.1. IN-SITU FOAM GENERATION

Foam generation was observed in our five model fractures, with corresponding mobility reduction of the gas. Foam was generated in-situ mainly by snap-off and lamella division. In samples 2, 3 and 4, lamella division and repeated snap-off occurred. The throats in these samples are wide in the plane of the fracture (Appendix A) but narrow in aperture d_t (Table 5.1); this slit-shaped geometry favors snap-off (Rossen, 1996, 2003). In Sample 2 (Chapter 3), snap-off created bubbles that are much smaller than the pores.

Table 5.1: Model fracture aperture and roughness data (all measurements are in μm).

Paramter	Sample 1	Sample 2	Sample 3	Sample 4	Sample 4a	Sample 4b	Sample 5	Sample 5a	Sample 5b
Hydraulic aperture , d_H	670	66	330	51	72	204	115	145	170
Pore-throat aperture, d_t	818	68	443	100	150	414	131	165	193
Pore-body aperture, d_b	1128	138	853	210	296	851	211	266	312
Pore length, L_p	2661	819	5156	4415	4415	4415	2421	2421	2421
Correlation length, L_{cor}	2754	795	4800	5100	5100	5100	2240	2240	2240

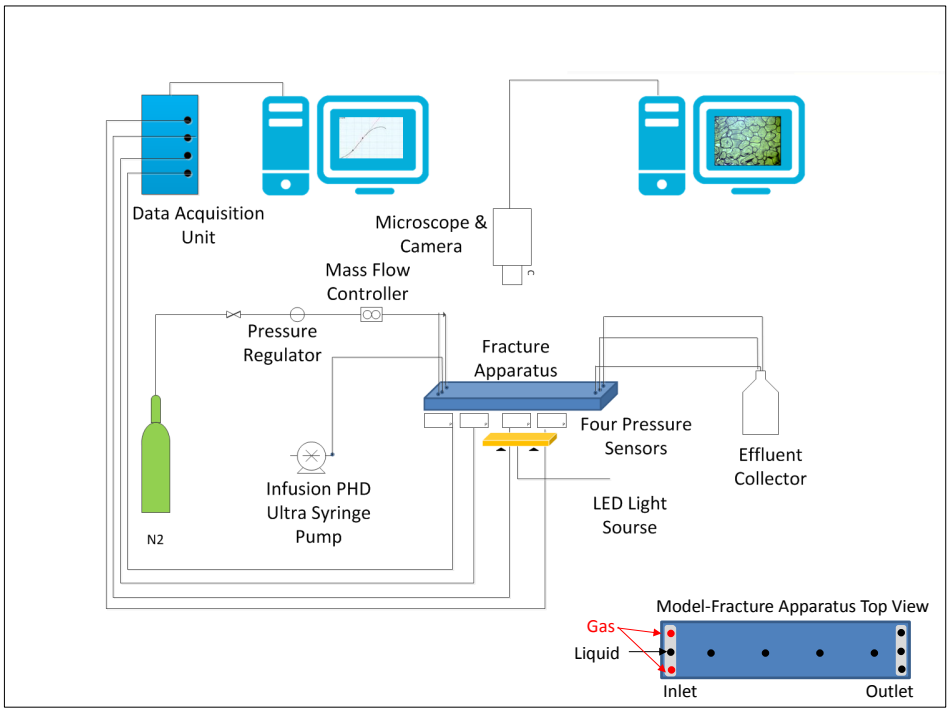

Figure 5.6: Schematic of the experimental setup. The injection and production lines are fitted from the bottom of the fracture plate, but are drawn from the top to avoid clutter in the diagram. The bottom right shows the model-fracture design.

Lamella division was observed at high gas fractional flow (f_g). Figure 5.7 shows snap-off events in Sample 2 at f_g = 0.37 and total superficial velocity (u_t) of 0.0021 m/s. Figure 5.8 shows lamella division at f_g = 0.87 and u_t = 0.0049 m/s. In these and similar images to follow, the white area represents water, which occupies the peaks in the topography of figures 1-5 (i.e., locations of the narrowest aperture) and some pore throats (saddle points between peaks; see Appendix A). Gas occupies the pore bodies (i.e., locations of widest aperture, or valleys in figures 1-5). Lamellae appear as white lines in figures 7ff. We observe foam generation by lamella division as a film leading a large bubble divides as it encounters a split in the flow path. We did not observe lamella division at f_g lower than 0.76 in Sample 2. Inter-bubble diffusion does not have time to operate because bubble residence time in our model is relatively short, approximately 2.7 min (AlQuaimi and Rossen, 2017d). A similar observation of bubbles smaller than pores was reported for foam flow in fractures by Fernø et al. (2016).

In samples 3 and 4, we also observed snap-off; see figures. 5.9 and 5.11, respectively. Samples 3 and 4 differ greatly in their hydraulic apertures and correlation length for aperture (Table 5.1). This led to significant differences in foam texture (cf. figures 5.9 and 5.11), foam texture as a function of position (discussed in the next section), and pressure

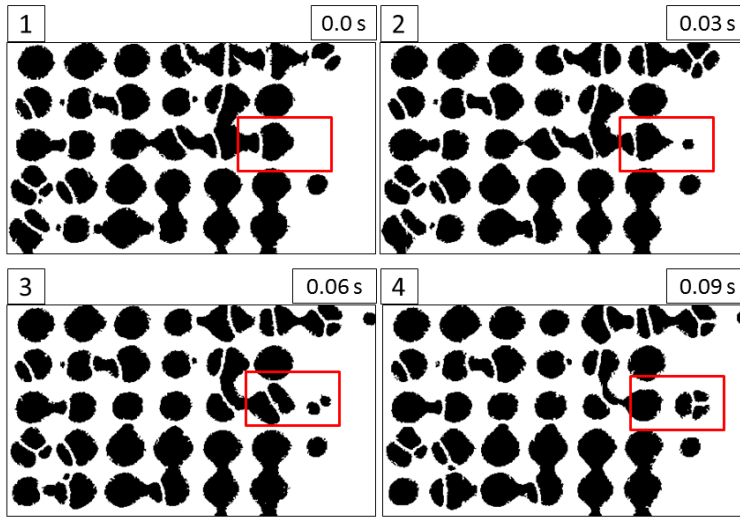

Figure 5.7: Sample 2: foam generation by snap-off; image size (0.75×0.43 cm). f_g = 0.37 and u_t = 0.0021 m/s. Black is gas and white is water. The area of interest is highlighted in red.

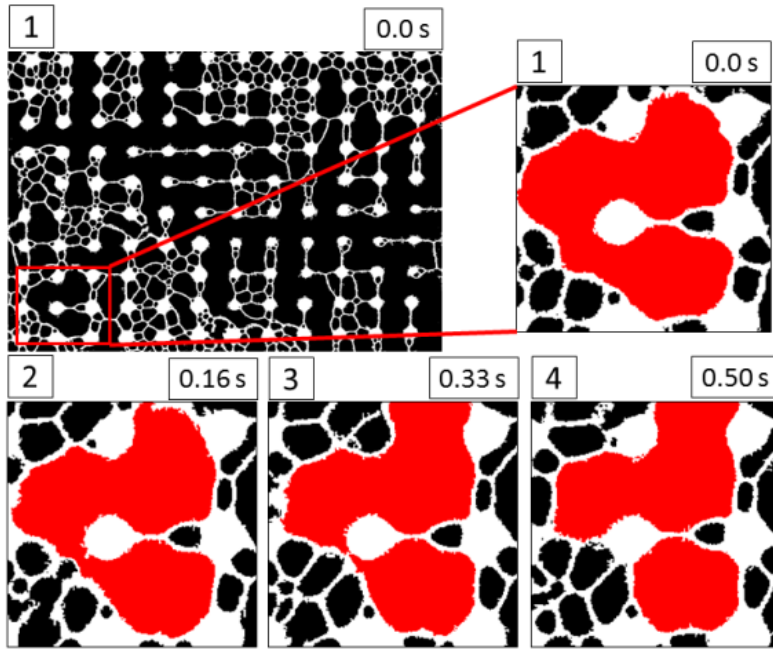

Figure 5.8: Sample 2: foam generation by lamella division; image size (0.21×0.2 cm). f_g = 0.87 and u_t = 0.0049 m/s. Black is gas and white is water. The divided bubble is highlighted in red.

response. Moreover, in samples 3 and 4 lamella division occurred at flow conditions that were similar to those of snap-off. figures 5.10 and 5.12 show lamella division in samples 3 and 4, respectively.

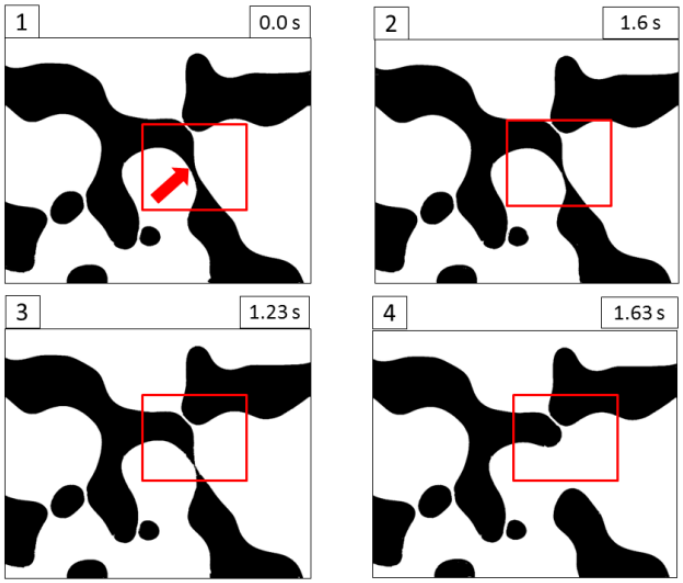

Figure 5.9: Sample 3: foam generation by snap-off (see arrow); image size (2.6×2.1 cm). f_g = 0.45 and u_t = 0.0013 m/s. Black is gas and white is water.

In samples 1 and 5, foam was generated primarily by lamella division (cf. figures 5.13 and 5.14). In Sample 1 the throats are deeper than in the other samples, and thus less slit-like. In Sample 5 the throats are slightly deeper than in Sample 4, for instance, but not nearly as wide in the plane of the fracture (figures 5.4 and 5.5, Appendix A): again, less slit-like and less favourable to snap-off. The large aperture of Sample 1 has a significant impact on foam texture and pressure gradient, as discussed below. These results show that the foam-generation mechanism is a function of aperture, fracture-wall geometry, gas fractional flow and total superficial velocity. Surfactant-solution type and concentration are also important but they were the same for all experiments.

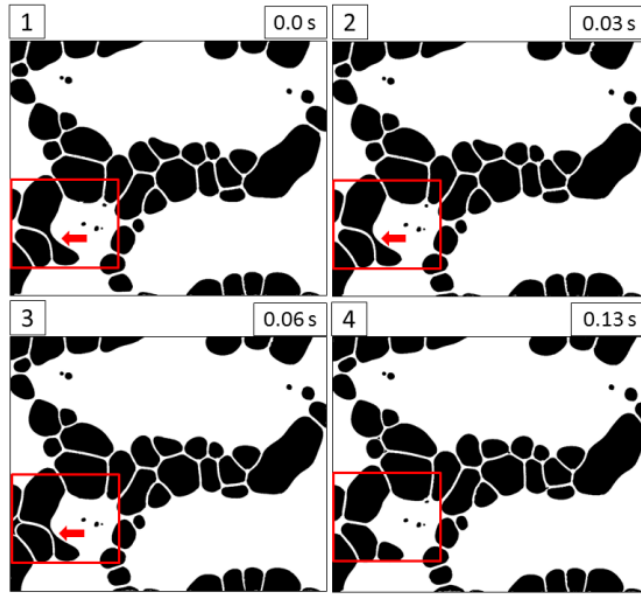

Figure 5.10: Sample 3: foam generation by lamella division (see box); image size (2.6×2.1 cm). f_g = 0.45 and u_t = 0.0025 m/s. Black is gas and white is water.

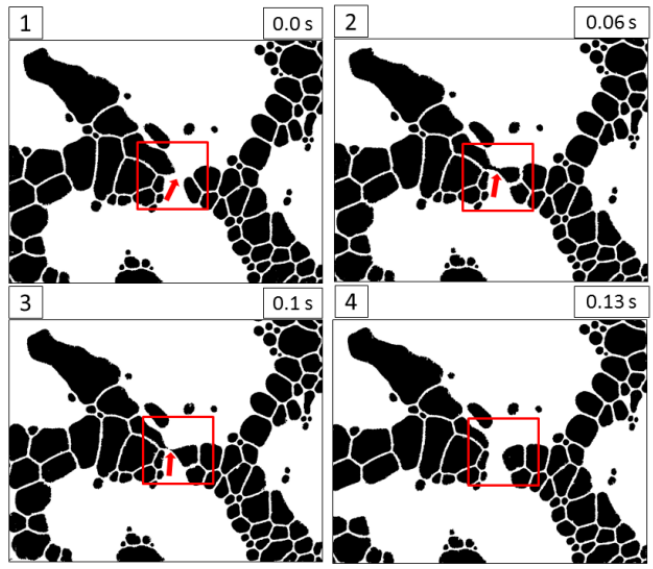

Figure 5.11: Sample 4: foam generation by snap-off (see box); image size (1.1×0.9 cm). f_g = 0.68 and u_t = 0.0032 m/s. Black is gas and white is water.

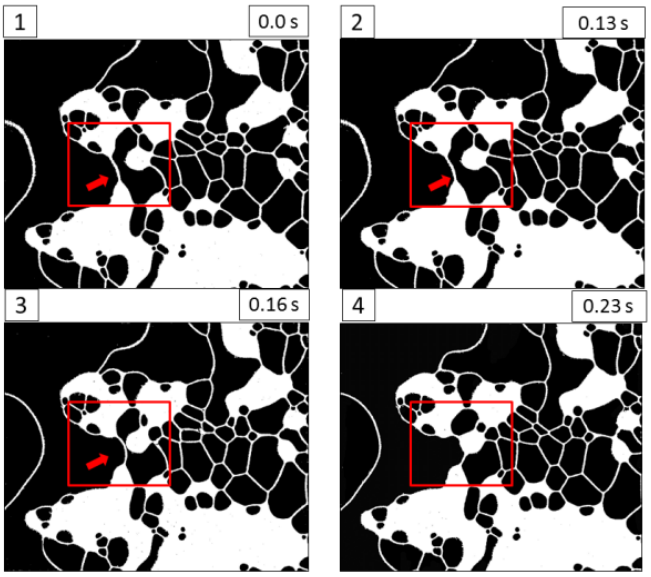

Figure 5.12: Sample 4: foam generation by lamella division (see box); image size (0.72×0.66 cm). f_g = 0.45 and u_t = 0.0016 m/s. Black is gas and white is water.

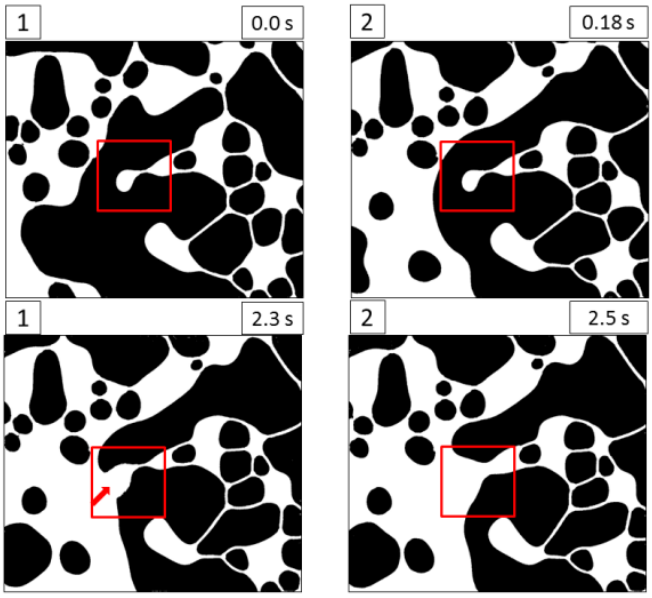

Figure 5.13: Sample 1: foam generation by lamella division (see box); image size (2.1×1.8 cm). f_g = 0.60 and u_t = 0.0025 m/s. Black is gas and white is water.

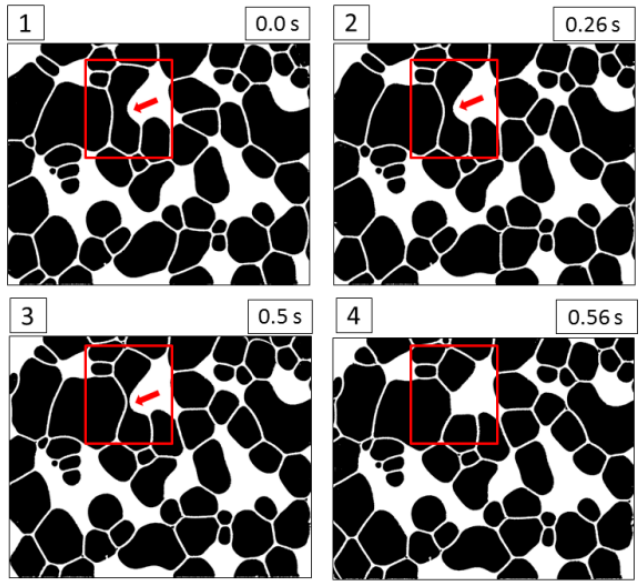

Figure 5.14: Sample 5: foam generation by lamella division (see box); image size (1.2×0.96 cm). f_g = 0.70 and u_t = 0.0007m/s. Black is gas and white is water.

5.4.2. FOAM PROPAGATION

We monitored the texture of the foam across the fracture at steady-state flow conditions, using images captured at different distances from the injection port.

5.4.2.1. SAMPLE 1

Sample 1 has the greatest hydraulic aperture d_H (Table 5.1) and many asperities. We analyzed foam texture for f_g = 0.45 and u_t = 0.0012 m/s. The analysis shows that gas enters the model and propagates approximately 6 to 10 cm as a continuous phase (Figure 5.15, image 1). This is evident in the average bubble size and the number of bubbles per unit area. The continuous gas phase starts to break up into relatively smaller gas bubbles by lamella division as discussed previously. We did not observe significant changes in foam texture in sections 2 and 3 (Figure 5.15, images 2 and 3). However, in the last section the bubble size became somewhat smaller than the average size of the pore, 7.3 mm^2, determined from the 2D network analysis (Figure 5.15, image 4). Table 5.2 illustrates the statistics of the image analysis for Sample 1. We believe that the foam has not reached a final local-equilibrium state in this case. The wide aperture strongly influences the entrance region, lengthening it considerably. This effect was also clear in the pressure response, as discussed in the next section.

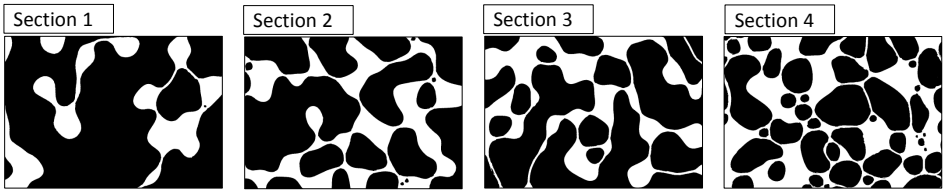

Figure 5.15: Sample 1: Foam texture versus distance at f_g = 0.45 and u_t = 0.0012 m/s. Image size is 2.5×1.7 cm; black is gas and white is water. The images were captured once the pressure gradient had stabilized. Gas is initially continuous and bubbles are generated by lamella division as gas propagates through the fracture. Bubble size becomes smaller than the pore-body size toward the last section of the model fracture. The number of bubbles per unit area significantly increased in Section 4.

Table 5.2: Sample 1: image analysis statistics. f_g = 0.45 and u_t = 0.0012 m/s.

Section	1	2	3	4
Distance from inlet, mm	60	150	230	360
Average bubble size, mm^2	58.06	14.23	17.66	4.92
Bubble size, std. dev., mm^2	107.6	20.63	21.22	6.19
Number of bubbles per unit area	5	21	17	55

5.4.2.2. SAMPLE 2

Sample 2 has a regular pattern in its roughness, with much smaller d_H and L_p than Sample 1. Foam was generated mainly by snap-off and lamella division. In a manner similar to Sample 1, we captured images at different distances from the injection point. In this model fracture, unlike the others, there was converging flow toward a single outlet port, so the last section is not included in the foam-texture analysis (Chapter 3). This analysis was performed at f_g = 0.37 and u_t = 0.0021 m/s. The foam gets finer as it propagates through the facture, due to snap-off. The average bubble size decreases and the number of bubbles per unit area in Section 3 is almost double that in Section 1 (Figure 5.16 and Table 5.3). Despite the fact that the two tests were not at identical f_g and u_t, in Sample 2 bubble size is much smaller than in Sample 1, indicating that both d_H and L_p play a role in foam texture. This test also shows that by Section 3 of Sample 2 the average bubble size was much smaller than the pore body of the sample, which is 0.50 mm^2.

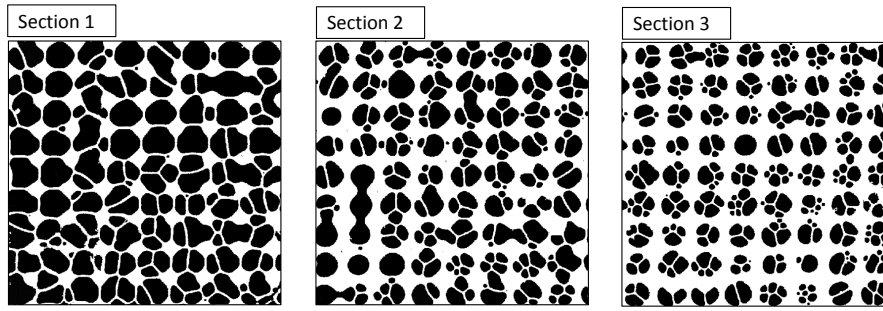

Figure 5.16: Sample 2: Foam texture versus distance at f_g = 0.37, u_t = 0.0021 m/s; black is gas and white is water. The images are captured during the stabilized pressure gradient. Image size 0.8×0.77 cm. Foam-texture analysis shows that the average bubble size decreases and the number of bubbles in Section 3 is almost double that in Section 1.

Table 5.3: Sample 1: image analysis statistics. f_g = 0.37, u_t = 0.0021 m/s.

Section	1	2	3
Distance from inlet, mm	20	120	270
Average bubble size, mm^2	0.250	0.138	0.081
Bubble size, std. dev., mm^2	0.205	0.125	0.056
Number of bubbles per unit area	165	217	303

5.4.2.3. SAMPLE 3

Sample 3 has the second largest d_H and the largest L_p (Table 5.1), and foam was generated by both snap-off and lamella division as discussed earlier. Foam-texture analysis was performed at f_g = 0.60 and u_t = 0.0013 m/s and shows that the average bubble size decreases; the number of bubbles in Section 4 is 12 times greater than in Section 1 (Figure 5.17). The average pore-body size of this sample is 32.9 mm^2, which is significantly larger than the average bubble size of 4.47 mm^2 observed towards the end of the fracture (Table 5.4). Similarly to Sample 1, we observed large gas bubbles near the entrance and only towards the last section did the foam bubbles become finer.

Figure 5.17: Sample 3: Foam texture versus distance at f_g = 0.60, u_t = 0.0013 m/s; black is gas and white is water. The images are captured during stabilized pressure gradient. Image size 1.7×1.1 cm. The number of bubbles is 12-times greater in Section 4 than in Section 1.

Table 5.4: Sample 1: image analysis statistics. f_g = 0.60, u_t = 0.0013 m/s.

Section	1	2	3	4
Distance from inlet, mm	60	150	230	360
Average bubble size, mm^2	34.24	15.73	12.99	4.47
Bubble size, std. dev., mm^2	19.55	18.72	6.93	5.63
Number of bubbles per unit area	2	5	10	24

5.4.2.4. SAMPLE 4

Sample 4 is characterized by a small d_H and a large L_p. Foam was generated by both snap-off and lamella division in this sample. Foam-texture analysis was performed at f_g = 0.70 and u_t = 0.0016 m/s. This analysis shows that a considerable number of lamellae have been created in Section 2, as compared to samples 1 and 3, where the d_H were much larger, 670 and 330 μm, respectively (Figure 5.18). Foam propagates through the fracture and is refined as it flows downstream. The average pore-body size in this sample is 13.2 mm^2, compared to the average bubble size of 0.14 mm^2 observed towards the end of the fracture (Table 5.5). The small d_H in this sample has influenced the bubble size greatly, making a significant number of bubbles within a short distance of fluid entry.

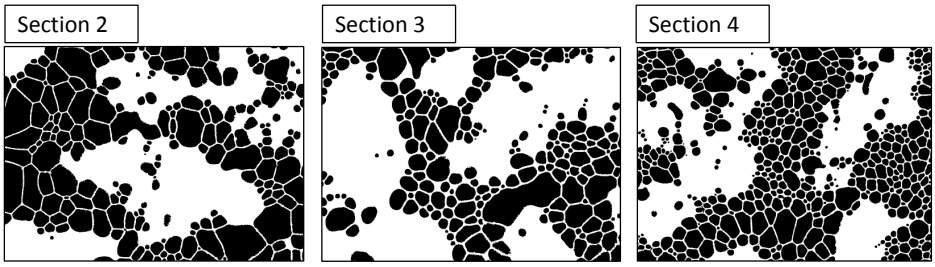

Figure 5.18: Sample 4: Foam texture versus distance at f_g = 0.70, u_t = 0.0016 m/s, and black is gas and white is water. The images were captured during the stabilized pressure gradient. Image size 1.4×1.0 cm. An image of Section 1 was not available for the analysis. Among our samples, Sample 4 has the smallest d_H, 51 μm. A considerably greater number of lamellae have been created in Section 2 as compared to samples 1 and 3, where d_H = 670 and 330 μm, respectively.

In addition to the original samples 4, with d_H = 51 μm, Sample 4a and 4b have d_H = 72 and 207 μm, respectively. We made a comparison of foam texture at the same distance from the injection port once a stable pressure gradient was observed in each case. This test was conducted at fixed f_g = 0.45 and u_t = 0.0032 m/s. Coarser-textured foam is evident as d_H increases (Figure 5.19), and fewer snap-off events are observed at d_H of 207 μm. (The increase in bubble volume is greater than the increase in bubble area as aperture increases (Table 5.6).) The average bubble size increases with increasing d_H (Table 5.6).

Table 5.5: Sample 1: image analysis statistics. f_g = 0.70, u_t = 0.0016 m/s.

Section	1	2	3	4
Distance from inlet, mm	60	150	230	360
Average bubble size, mm^2	NA	0.36	0.26	0.14
Bubble size, std. dev., mm^2	NA	0.47	0.40	0.16
Number of bubbles per unit area	NA	207	216	479

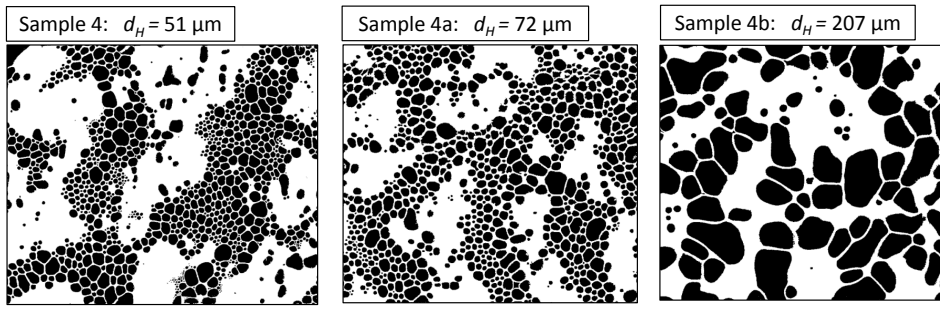

Figure 5.19: Samples 4, 4a, 4b: foam texture versus d_H at f_g = 0.45 and u_t = 0.0032 m/s. Black is gas and white is water. The images are captured during the stabilized pressure gradient. The image size is 1.7×1.5 cm. The correlation length of roughness and L_p are the same in all three fractures. Images are captured 36 cm from the inlet. The analysis shows that for fixed L_p the average bubble size increases with increasing d_H.

Table 5.6: Samples 4, 4a, 4b: effect of hydraulic aperture on foam texture at fixed L_p

Paramter	Sample 4	Sample 4a	Sample 4b
Hydraulic aperture d_H , µm	51	72	207
Average bubble size, mm^2	0.097	0.148	1.37
Bubble size, std. dev., mm^2	0.114	0.133	1.32
Number of bubbles per unit area	972	750	78

5.4.2.5. SAMPLE 5

Foam was generated solely by lamella division in Sample 5. The foam-texture analysis was performed at f_g = 0.46 and u_t = 0.0007 m/s. Initially, the gas forms a continuous phase, and foam bubbles are created as it propagates downstream. The average pore-body size of this sample is 4.00 mm^2, compared to the average bubble size of 0.53 mm^2 observed towards the end of the fracture (Table 5.7). Foam is generated by a similar mechanism in both samples 1 and 5. The two samples have roughly the same L_p; however, the foam texture is different in the two samples due to the difference in apertures (Figure 5.20).

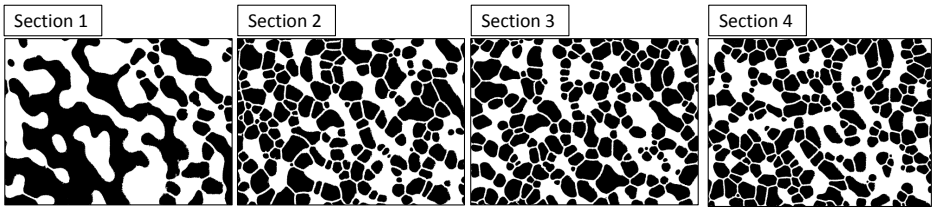

Figure 5.20: Sample 5: Foam texture versus distance at f_g = 0.46, u_t = 0.0007 m/s; black is gas and white is water. The images are captured during the stabilized pressure gradient. Image size 1.6×1.6 cm. Initially the gas forms a continuous phase, then bubbles are created by lamella division.

Table 5.7: Sample 1: image analysis statistics. f_g = 0.46, u_t = 0.0007 m/s.

Section	1	2	3	4
Distance from inlet, mm	60	150	230	360
Average bubble size, mm^2	2.48	0.66	0.60	0.53
Bubble size, std. dev., mm^2	7.84	0.57	0.48	0.36
Number of bubbles per unit area	37	160	176	194

Samples 5a and 5b have d_H = 145 and 170 μm, respectively. Tests were conducted at a fixed f_g = 0.45 and u_t = 0.0022 m/s (Figure 5.21). The image analysis reveals a similar behavior to Sample 4, with coarser-textured foam observed as d_H increases. The average bubble size increases, and the number of bubbles decreases, as d_H increases (Table 5.8).

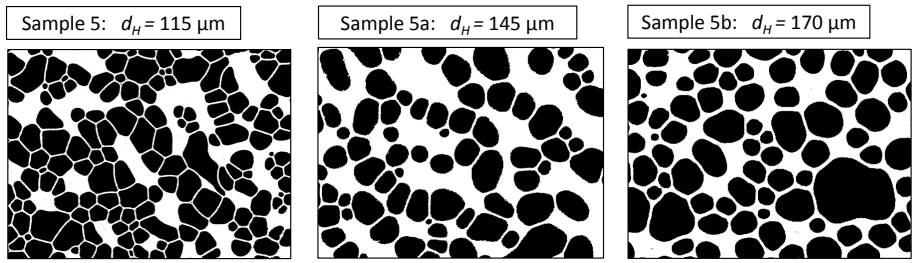

Figure 5.21: Samples 5, 5a, 5b: Foam texture versus d_H at f_g = 0.45 and u_t = 0.0022 m/s. Black is gas and white is water. The images are captured during the stabilized pressure gradient. The image size is 1.1×0.86 cm. The roughness scale, or L_p, is the same for all three fractures. Images are captured 36 cm from the inlet. The analysis shows that for a fixed L_p the average bubble size increases as d_H increases.

Table 5.8: Samples 5, 5a, 5b: effect of hydraulic aperture on foam texture at fixed L_p

Paramter	Sample 5	Sample 5a	Sample 5b
Hydraulic aperture d_H , µm	115	145	170
Average bubble size, mm^2	0.468	0.74	0.943
Bubble size, std. dev., mm^2	0.343	0.438	1.02
Number of bubbles per unit area	120	55	54

5.5. COMPARISON OF SAMPLES

These experiments demonstrate the effect of d_H and L_p on foam texture. In all the samples, foam becomes finer as it propagates through the fracture. We cannot confirm that foam has reached the final local equilibrium state by the time it reaches the outlet in these experiments. Fine-textured foam was observed in the fractures with the smallest apertures and course-textured foam in the fractures with the largest apertures. Samples with approximately similar apertures (samples 2 and 4) and different L_p show two distinctly different textures: smaller bubbles in the fracture with smaller pores, though the bubbles are smaller than the pores in both cases. Foam occupies the pore bodies differently, based on the shape of the pore bodies.

5.6. FOAM-QUALITY SCANS

Foam-quality scans were carried out on these model fractures, by holding u_t constant and varying f_g. The surfactant solution and nitrogen were co-injected into the initially water-saturated fracture, and the pressure gradient across the four sections was recorded until stabilization of pressure gradient was achieved. Significant pressure oscillations were observed in these tests, and larger oscillations were evident at high f_g. These oscillations reduce the time-average foam apparent viscosity. In nonfractured porous media

the foam behavior at high quality is believed to reflect the destruction of foam at the limiting capillary pressure (Khatib et al., 1988; Ransohoff and Radke, 1988; Alvarez et al., 2001). We did not observe significant foam coalescence in any of our samples at any tested foam qualities. In our experiments oscillations in pressure gradient reflect fluctuations in foam generation (AlQuaimi and Rossen, 2017b).

We selected the fourth section of each sample, except for Sample 2, as the basis for our analysis of the pressure behavior. In Sample 2, we used the third section, due to the converging flow toward the outlet port in the fourth section. We averaged the pressure gradient over the period of stabilization for each foam quality. The injected gas volume was corrected to the pressure at the middle of the fracture. The pressure-gradient data was acquired in a random sequence, to avoid mis-interpreting the possible effects of hysteresis that may occur in the case of sequential increase or decrease in f_g.

We tested foam mobility as a function of foam quality f_g for four total superficial velocities u_t, for three of the model fractures (samples 2, 4 and 5). For Sample 1, with d_H = 670 µm, foam was observed only towards the outlet of the model. The recorded pressure gradient ∇P was only a few mbar/m, with large oscillations (Figure 5.22). Although we tested flow at different values of u_t and f_g, we were not able to obtain a meaningful foam-quality scan on this sample due to the large oscillation at very low pressure gradients: the relative uncertainty and variability in ∇P was too great for meaningful analysis, especially at higher f_g. Similarly, for Sample 3, with the second largest d_H of 330 µm, we did not obtain a foam-quality scan. The recorded pressure gradient was an average of 34.6 mbar/m with significant fluctuations (Figure 5.23), even at low f_g. It was harder to create foam, reduce gas mobility and increase ∇P significantly with wider apertures.

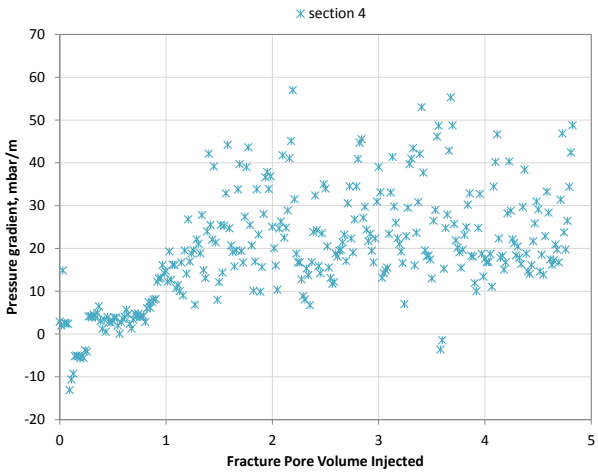

Figure 5.22: Sample 1: (d_H = 670 µm); Section 4 pressure gradient at u_t = 0.0012 m/s and f_g = 0.45. No foam-quality scan could be carried out due to small magnitude and the large oscillation at low pressure gradients.

Foam-quality scans were successfully carried out for samples 2, 4 and 5. In general, as

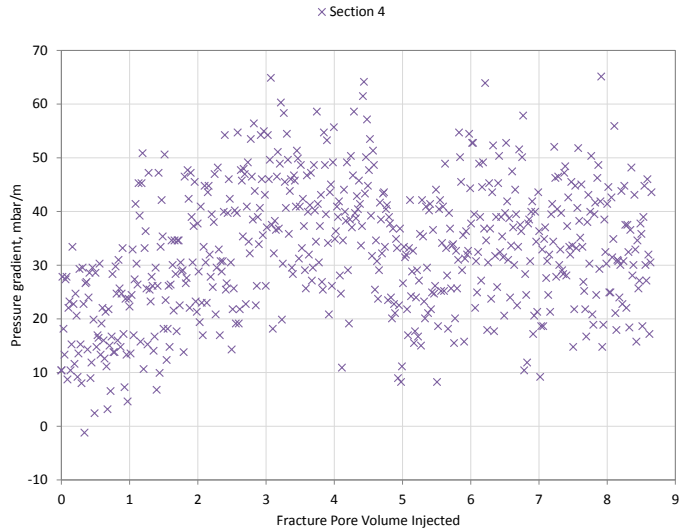

Figure 5.23: Sample 3: (d_H = 330 µm); section 4 pressure gradient at u_t = 0.0013 m/s and f_g = 0.45. No foam-quality scan could be carried out due to the small magnitude and large oscillation at low pressure gradients.

the velocity increases, the pressure gradient increases; however, the increase is not proportional to u_t. Figures 5.24, 5.25 and 5.26 show the foam-quality scans of samples 2, 4 and 5, respectively. The effect of L_p or the correlation length on the pressure gradient is made clear by comparing samples 2 and 4 , which have the similar hydraulic aperture d_H (Table 5.1). The overall pressure gradient for Sample 2 is greater than that for Sample 4. We believe this is due to the fact that there is a throat which both contributes to foam generation and restricts bubble flow every 800 µm in Sample 2 (Table 5.1). The throats are also somewhat wider in Sample 4, but the pores are five times longer.

Central to the understanding of flow in nonfractured porous media is the existence of two distinct foam-flow regimes, corresponding to high foam quality and low foam quality (Osterloh and Jante, 1992; Alvarez et al., 2001). The pressure gradient is independent of liquid velocity in the low-quality regime and independent of gas velocity in the high-quality regime. In Sample 2, these two regimes were observed. Figure 5.27 shows the pressure-gradient contours for Sample 2. Pressure-gradient data of samples 4 and 5, are shown in figures 5.28 and 5.29, respectively.

The same two foam-flow regimes were observed in Sample 5. For Sample 4, all of the data would correspond to a transition region between the high- and low-quality regimes. The transition between regimes is sensitive to both the nature of the porous medium and the ability of the surfactant to stabilize foam (Alvarez et al., 2001). Given the absence of evidence of either flow regime in so wide a scan of foam quality (see Figure 5.28), it may well be that the two regimes do not apply to this foam in this fracture. We do not

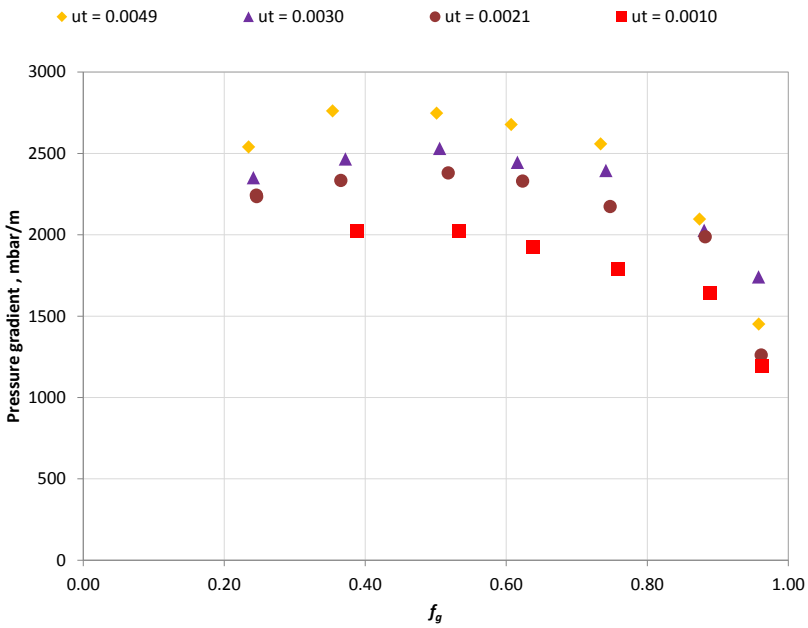

Figure 5.24: Sample 2: foam-quality scans at different total-injection velocities (m/s). As the velocity increases the pressure gradient increases; however, the increase is not proportional to u_t. The standard deviations of foam pressure-gradient data are approximately 60 and 570 mbar/m at low quality and high quality, respectively. They are not drawn to avoid clutter in the diagram.

Table 5.9: Summary of pressure-gradient results with respect to variation in d_H and L_p at specific flow conditions.

Sample	d_H, m	u_t, m/s	f_g	∇P_{foam}, mbar/m	∇P_{water}, mbar/m	MRF	L_P
Sample 1	670	0.0025	0.45	35	0.67	52	2661
Sample 2	66	0.0030	0.38	2466	82.6	30	819
Sample 3	330	0.0025	0.45	52	2.75	19	5156
Sample 4	51	0.0032	0.45	713	142.6	5	4415
Sample 4a	72	0.0032	0.45	800	80	10	4415
Sample 4b	207	0.0032	0.45	137	9.1	15	4415
Sample 5	115	0.0022	0.45	563	29	19.4	2421
Sample 5a	145	0.0022	0.45	162	13	12.4	2421
Sample 5b	170	0.0022	0.45	117	13	9	2421

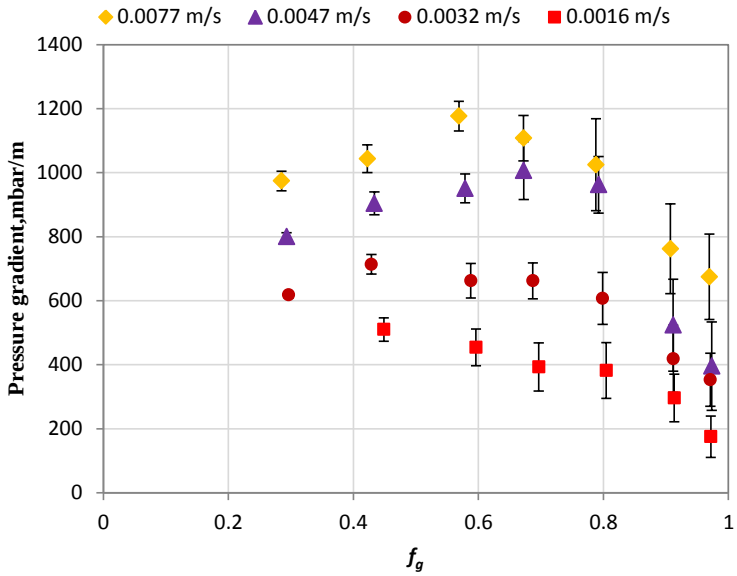

Figure 5.25: Sample 4: foam-quality scans at different total-injection velocities (m/s). Pressure gradient increases as u_t increases. The error bars in the data reflect oscillations in pressure gradient.

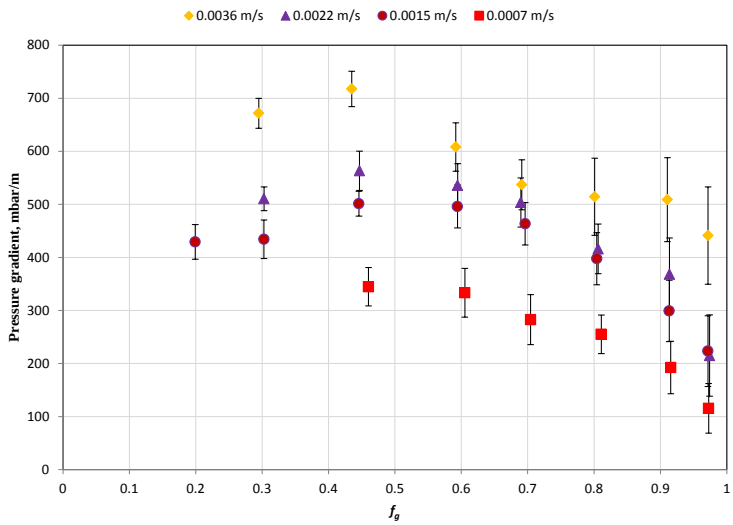

Figure 5.26: Sample 5: foam-quality scans at different total-injection velocities (m/s). Pressure gradient increases as u_t increases. The error bars in the data reflect oscillations in pressure gradient.

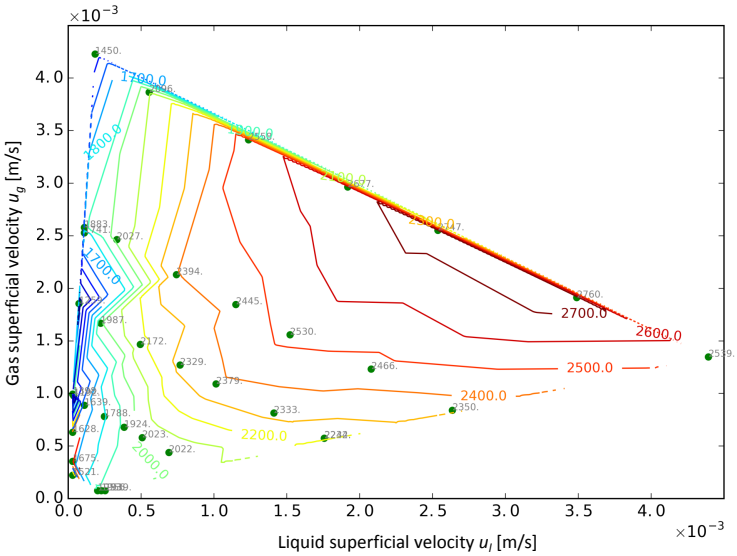

Figure 5.27: Sample 2: pressure-gradient data plotted as a contour plot. The plot shows the existence of two flow regimes in the fracture.

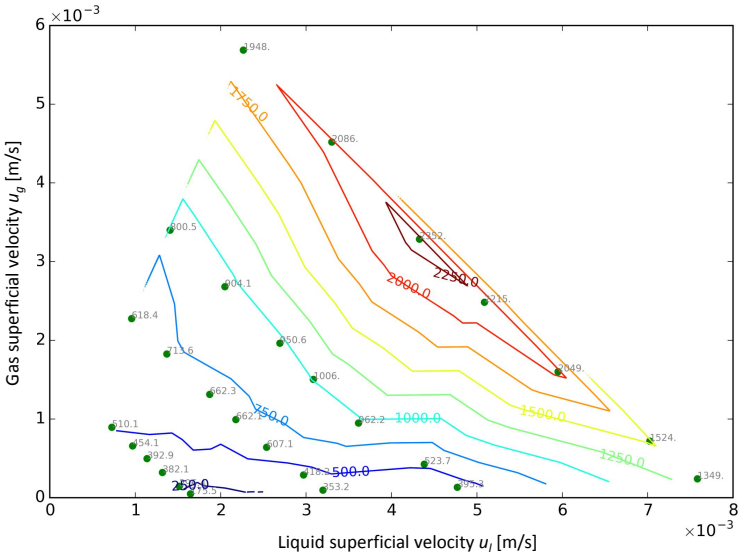

Figure 5.28: Sample 4: pressure-gradient data plotted as a contour plot. The plot shows that the recorded pressure-gradient data falls within the transition between the high- and low-quality regimes.

know the reason for this difference. Sample 4 has a narrower aperture than Sample 5 but similar aperture to Sample 2 (Table 5.1). It is possible that foam has not reached local

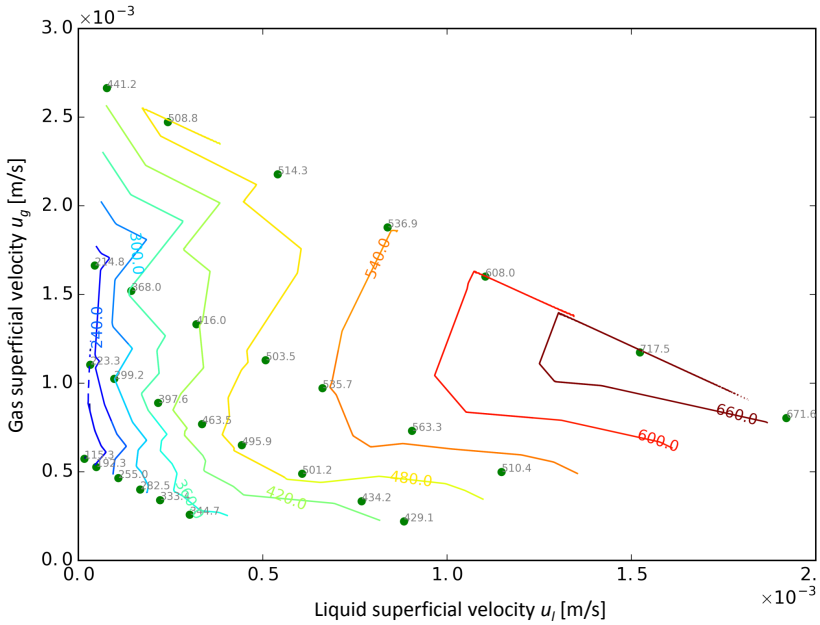

Figure 5.29: Sample 5: pressure-gradient data plotted as a contour plot. The plot shows the existence of two flow regimes in the fracture.

equilibrium with the fracture, since the texture is still rapidly changing in the fourth section (Figure 5.18, Table 5.5).

As d_H increases from 51 to 72 µm (samples 4 and 4a), the pressure gradient increases for all the foam qualities tested. We do not have an explanation for this increase in pressure gradient. However, when d_H increases further to 207 µm (samples 4b), the pressure gradient decreases substantially (Figure 5.30).

As d_H increases from 115 to 145 µm (samples 5 and 5a), the pressure gradient substantially decreases. An additional 17% increase in d_H yields a marginal decrease in pressure gradient (Figure 5.31). This appears to be related to the number of bubbles in the two cases. The number of bubbles for d_H = 170 µm decrease slightly compared to the case at d_H = 145 µm.

Table 5.9 summarizes the pressure-gradient results. For this comparison we selected f_g and u_t to be in the vicinity of 0.45 and 0.0025 m/s for all the samples. Samples 2 and 4 deviate the most from the selected u_t, but based on the shear-thinning behavior shown in figures 5.24 and 5.26, we do not expect a significant change in the values of ∇P_{foam}. Sample 2 showed the highest value of ∇P_{foam}. We believe this reflects a small d_H and small L_p (compared to Sample 4, with similar d_H). The calculated mobility-reduction factor of foam to water (MRF) is based on the single-phase flow experiments used to

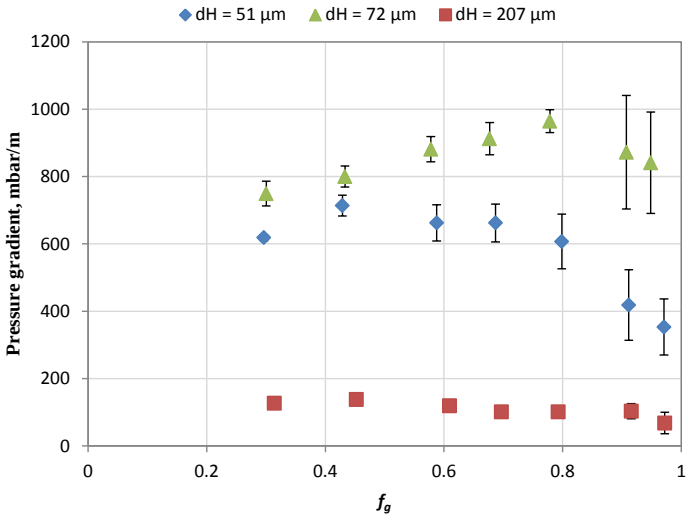

Figure 5.30: Samples 4, 4a, 4b: foam-quality scans at different values of d_H. As d_H increases from 51 to 72 µm, the pressure gradient increases, but when d_H increases further to 207 µm, the pressure gradient decreases substantially. The error bars in the data reflect oscillations in pressure gradient.

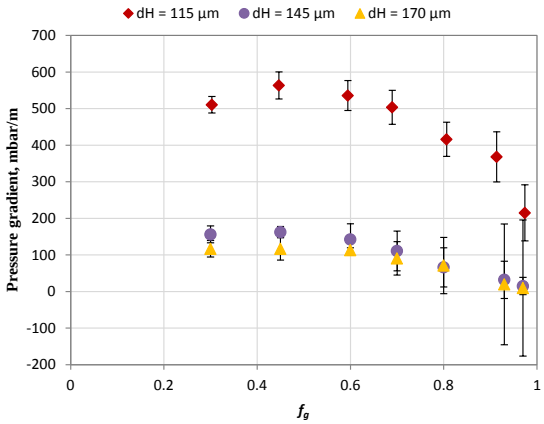

Figure 5.31: Sample 5, 5a, 5b: foam-quality scans at different d_H. As d_H increases from 115 to 145 µm, the pressure gradient substantially decreases. An additional 17% increase in d_H yields a marginal decrease in pressure gradient, due to a slight decrease in the number of bubbles between the two cases. The error bars in the data reflect oscillations in pressure gradient.

determine d_H for each sample (Chapter 2). There is no simple trend between MRF and either d_H or L_p alone (figures 5.32 and 5.33).

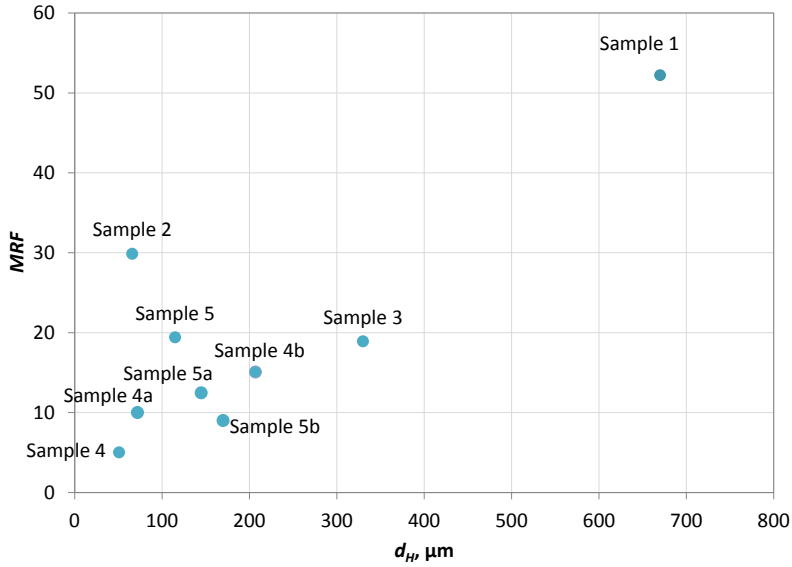

Figure 5.32: MRF versus d_H for all the samples. No clear trend can be established because of the change in roughness scale both laterally and vertically.

5.7. SUMMARY AND CONCLUSIONS

Experiments investigating foam generation, propagation and mobility reduction were carried out using a variety of model fractures with different geometries. The following conclusions can be drawn:

- Foam was generated in-situ in different model fractures that varied in the magnitudes of the aperture, aperture variation within the fracture and length scale over which the aperture varies. Foam in the fractures was generated primarily by two processes: capillary snap-off and lamella division. In both cases the fracture-wall roughness played a major role in foam generation.
- Two of the five fracture samples show only lamella division. This may reflect relatively wide apertures and a throat geometry less favorable for snap-off. The other three samples show both generation mechanisms at different foam qualities and superficial velocities.
- In cases where foam is generated only by lamella division, gas enters the fracture and propagates for some distance as a continuous phase before additional films are created.
- In all cases, bubbles smaller than the pores are generated and propagate through

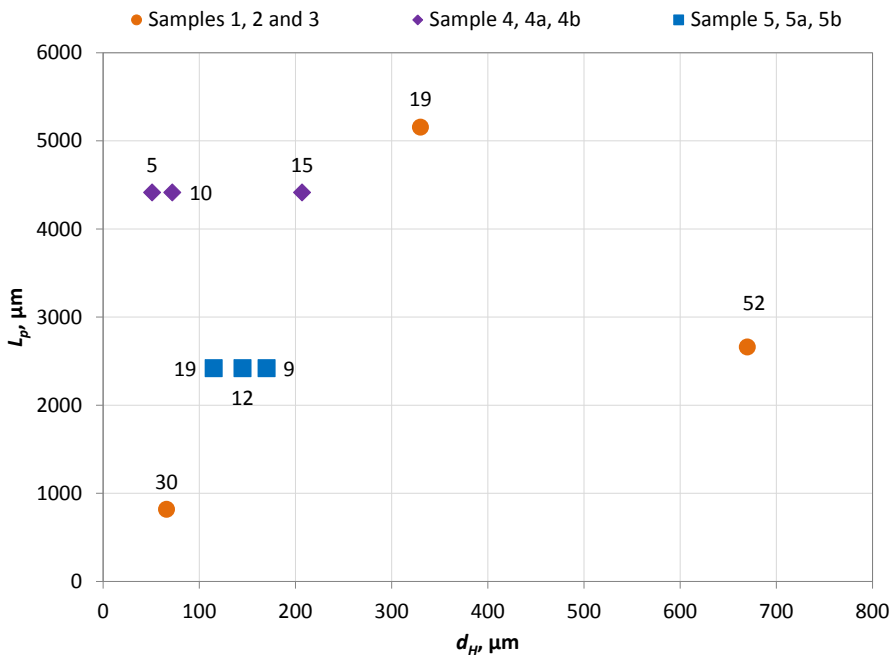

Figure 5.33: Effect of d_H and L_p on pressure gradient. The highest pressure gradient is achieved in Sample 2. L_p was fixed in samples 4 and 5 and d_H was increased in successive tests.

the fracture. The size of the bubbles is not always similar to the size of the pore, as is thought to be the case in 3D rock pore space, in part because bubbles reside for a time that is much shorter than the time required for diffusion to eliminate small bubbles. Moreover, snap-off can produce bubbles much smaller than pores in slit-shaped throats.

- Very small pressure gradients were recorded for the samples with very large apertures. In these cases no foam-quality scans could be conducted. In most cases, bubble size increased and pressure gradient declined as the aperture increased for the same roughness of the pore wall. In some cases, however, the mobility reduction factor increased relative to water; that is, as hydraulic aperture increased, the mobility of foam increased less than the square of the aperture (as mobility does for single-phase flow of water).

- Foam-quality scans were carried out using three samples.The pressure-gradient data reveals, in two of the fractures, high- and low-quality flow regimes like those seen in rock matrix. However, the high-quality regime was controlled not by foam stability and coalescence but by intermittent foam generation.

- Hydraulic aperture alone is not enough to determine foam-generation behavior

and mobility reduction. The roughness scale, both laterally and vertically, plays a significant role.

- When the roughness scale was fixed, a significant reduction in pressure gradient was measured with increasing hydraulic aperture. Foam bubbles become larger as the aperture increases.

6

CONCLUSIONS AND RECOMMENDATIONS

NATURALLY fractured reservoirs have unique characteristics in their flow behaviour. Short-circuiting is encountered in these reservoirs during displacement processes. This unfavourable behavior leads to considerable unrecovered hydrocarbons. Injection of gas without mobility control can have a negative economic consequence. Foam greatly reduces the mobility of gas in nonfractured porous media. However, the knowledge of foam in fractured porous media in far less complete.

6.1. CONCLUSIONS

In this dissertation, we contribute to the knowledge of trapping and mobilization and of foam flow in fractures. First, we study the mobilization of the nonwetting phase in fractures. Our goal is to understand the desaturation process in fractures and whether or not the conventional capillary number is suitable to describe the process. We propose a new definition of capillary number for fractures defined based on a force balance on a trapped ganglion in the fracture. We identify three geometric parameters to describe features governing mobilization. These parameters can be determined from analysis of a map of the fracture aperture along the fracture, with no two-phase flow data. Five distinctive model fractures made of roughened glass plates are used to test the new capillary number. We profile and analyse the fracture surfaces to determine the geometric parameters. We conduct desaturation experiments to quantify the relationship between trapping of ganglion and pressure gradient. We find that the new definition of the capillary number shows its suitability to describe the mobilization of the trapped nonwetting phase in fractures.

Our research objectives required the design of an extensive experimental program to study different aspects of foam flow in fractures. The first part is to study foam generation and mobilization, since it is crucial for the success of foam-injection processes. We fabricate a 40×10 cm model fracture to study foam generation and mobilization. Foam is generated mainly by capillary snap-off: fracture-wall roughness plays a major role in foam generation. Snap-off is less dominant at a high fractional flow of gas (f_g). Lamella division is observed at high f_g at two different total superficial velocities. In most cases, bubbles smaller than the pores are generated and propagated through the fracture. This depends in part on the geometry of the pore throats. Slit-shaped throats can give bubbles smaller than pore bodies. The size of the bubbles is not always similar to the size of the pore because bubbles reside in the apparatus for a time that is much shorter than the time required for diffusion to eliminate smaller bubbles compared to nonfractured porous media. We find that pressure gradient correlates inversely with the average size of the bubbles. Oscillations are observed in the pressure gradient at high f_g due to reduced and fluctuating foam generation. Similar oscillations are observed in 3D matrix porous-media, but in that case are ascribed to bubble destruction at the limiting capillary pressure. This oscillation is also evident in the bubble sizes; the standard division of bubble size increases as f_g increases.

In this dissertation, we also study foam rheology by varying superficial velocities of gas and surfactant solution. We carry out this part of the study using both horizontal and vertical flow to investigate the gravity effect. We find in our model fracture the same two foam-flow regimes central to the understanding of foam in 3D porous media: a low-quality regime where the pressure gradient is independent of liquid velocity and a high-quality regime where the pressure gradient is independent of gas velocity. The transition between regimes is less abrupt than in 3D porous media. Direct observation of bubble size, bubble trapping and mobilization, and foam stability as functions of superficial velocities allows comparison with our understanding of the mechanisms behind the two flow regimes in 3D porous media. Additionally, foam is shear-thinning in both regimes.

But in other important respects the mechanisms thought to be behind the two flow regimes in 3D media (foam coalescence) do not appear in our model fracture. Foam is not at the limit of stability in the high-quality regime. Mobility in the high-quality regime instead reflects reduced and fluctuating foam generation at high foam quality. We observe gas slugs due to fluctuating foam generation followed by fine-textured foam. The time elapsed between the gas slugs and the size of the slugs depend on both gas fractional flow and the total superficial velocity. The pressure-gradient data correlate well with the propagation of gas slugs downstream and hence confirms this finding of fluctuating foam generation at high fractional flow of gas. Finally, the two foam-flow regimes were observed during horizontal flow and vertical flow. Somewhat lower pressure gradient was recorded in vertical flow, however.

Fractures encountered in the field differ in their aperture, roughness scale, correlation length of the roughness, etc. In this study, we investigate foam-generation mechanisms in five fully characterized model fractures with different apertures and correlation lengths of the aperture distribution. We also study the rheology of the in-situ-generated foam by varying the superficial velocities of the gas and surfactant solutions. We compare the measured pressure gradient against the fracture attributes, aperture and the correlation length of the aperture. We also compare foam texture as a function of position within the fracture as the generated foam propagates through the fracture. We find that gas mobility is considerably reduced as a result of in-situ foam generation in our model fractures. Foam is generated predominantly by capillary snap-off and lamella division. Two of the five fracture samples show only lamella division, because the throat geometry is less favorable for snap-off. In cases where foam is generated only by lamella division, gas enters the fracture and propagates for some distance as a continuous phase before additional films are created. The other three samples show both snap-off and lamella division at different f_g and u_t. Very small pressure gradients, with oscillations, are recorded for the samples with very large apertures. In these cases, no foam-quality scans could be conducted. The measured mobility reduction depends on fracture attributes. Fracture wall roughness, represented by both the hydraulic aperture and the correlation length of the aperture, plays an important role in foam generation and mobility. Two model fractures show the same two foam-flow regimes central to the understanding of foam in nonfractured porous media. When the roughness scale is fixed, a significant reduction in pressure gradient is measured with an increasing hydraulic aperture. Foam bubbles become larger as the aperture increases.

6.2. RECOMMENDATIONS

We recommend continued the analysis of the experimental results to find a model that explains the behavior of foam in fractures. This is necessary as a predictive tool for fractures that are not tested in our research. An analysis based on the fracture characteristics can be used to simulate flow through it and predict pressure drop and mobility over distance.

We recommend to investigate whether and when local equilibrium is achieved. We can-

not confirm from our experiments that foam has reached local equilibrium, where the rate of lamella creation and destruction is equal. The experiments show that as aperture increases the entry effect becomes much larger. First, we recommend carrying out an experiment with an aperture of approximately 100 μm with a fracture length of 1 m. Then, repeat the experiment for the wider-aperture samples, which often have a larger roughness scale and a larger entry effect.

In our department laboratory, we have an apparatus that creates hydraulic fractures in rocks and blocks. We could start with fracturing granite or shale core samples. Samples could be fractured differently in terms of the magnitude of the load and direction. One could perform flow experiments on these samples and then compare the findings with our model fractures. It would be challenging to measure pressure at different sections in these samples because one would need to drill through the core and tap into the fracture. Therefore, pressure could be measured across the entire sample.

Dr. Barnhoorn's research group in our department has fractured many blocks with different lithology. If these blocks can be used, one could build a setup to do flow experiments on them. Otherwise, it is possible to make replicas and perform flow experiments.

Dr. Barnhoorn's research group has fractured core plugs and CT-scanned them for geomechanics studies. The data sets include fractures, which are natural and induced, from different rock types or lithology. These data can be analysed and converted into 2D "pore-network" maps based on the apertures. Then, fracture characteristics, aperture range, correlation length, etc., based on rock type and whether the fracture is induced or natural, could be studied. These data could later be fed into reservoir simulations for fluid flow studies.

A

FRACTURE SAMPLE PORE THROATS AND PORE BODIES DESCRIPTION

SEVERAL methods are available in the literature to extract a realistic pore network from matrix rock samples. The method we use is based on a simple concept using flood fill and image slicing. A MatLab® code was developed to highlight all the areas with height less than a particular threshold and then produce images at every 5 μm increment in height for the very rough samples and increments of 10 μm for the less rough ones. An isolated, deep region represents a pore body. When two regions join upon increasing height, the connection between them is a pore throat. The sequence of images is loaded into ImageJ, an open-source Java image-processing program, to identify the pore throats and draw the pore-body boundaries.

A

A.1. FRACTURE SAMPLES PORE THROATS STATISTICS

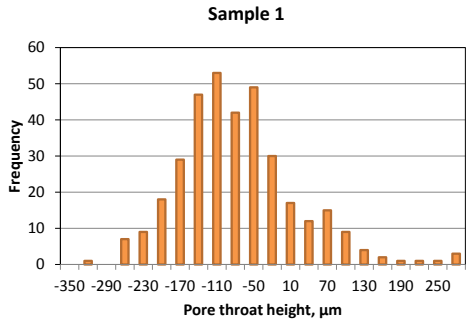

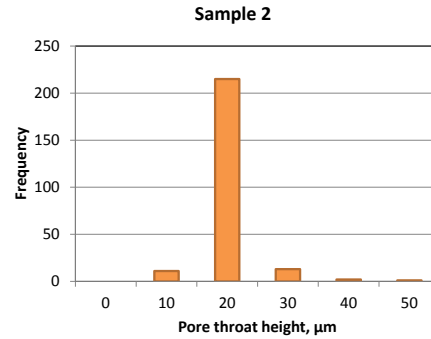

Figure A.1: Histogram of Sample 1 pore-throat height. **Figure A.2:** Histogram of Sample 2 pore-throat height.

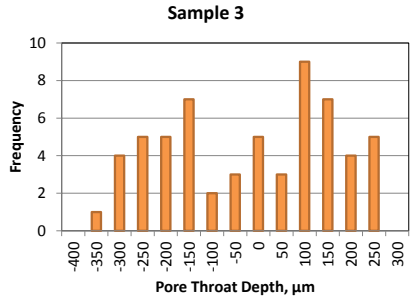

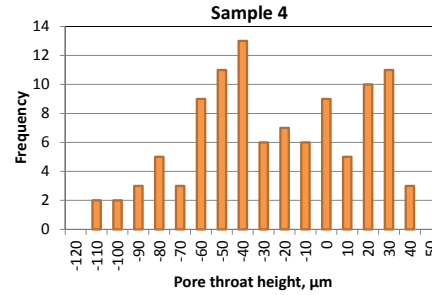

Figure A.3: Histogram of Sample 3 pore-throat height. **Figure A.4:** Histogram of Sample 4 pore-throat height.

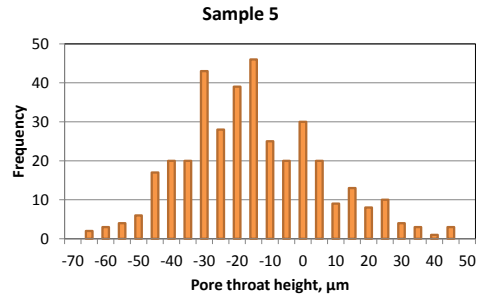

Figure A.5: Histogram of Sample 5 pore-throat height.

A.2. FRACTURE SAMPLES PORE BODIES STATISTICS

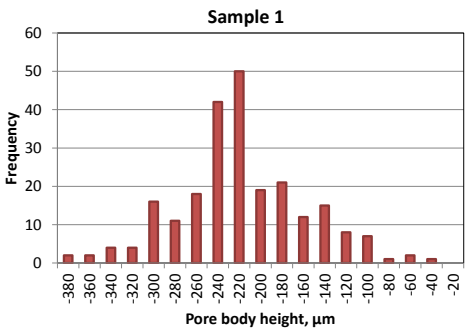

Figure A.6: Histogram of Sample 1 pore-body height.

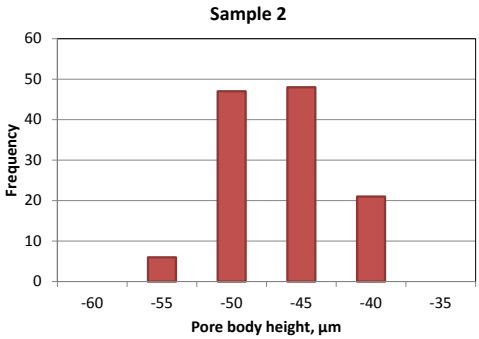

Figure A.7: Histogram of Sample 2 pore-body height.

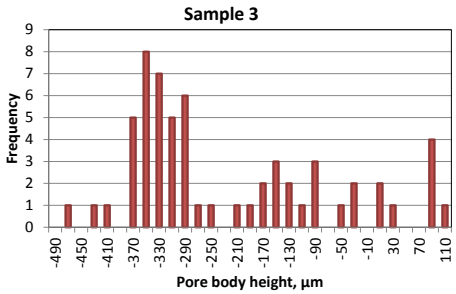

Figure A.8: Histogram of Sample 3 pore-body height.

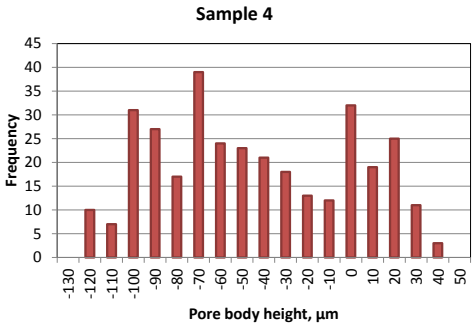

Figure A.9: Histogram of Sample 4 pore-body height.

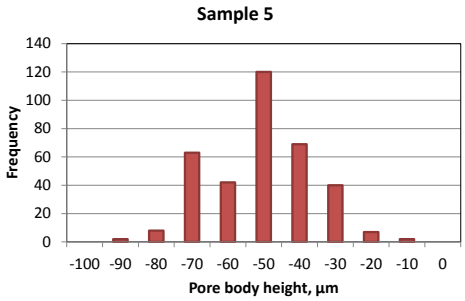

Figure A.10: Histogram of Sample 5 pore-body height.

A

A.3. PORE THROATS ON FRACTURE TOPOGRAPHY

Topography of fracture samples with conceptual pore throats superimposed on images. The images are 4.0×4.0 cm except the regular rough sample which is 1.0×1.0 cm. All the dimensions are in μm.

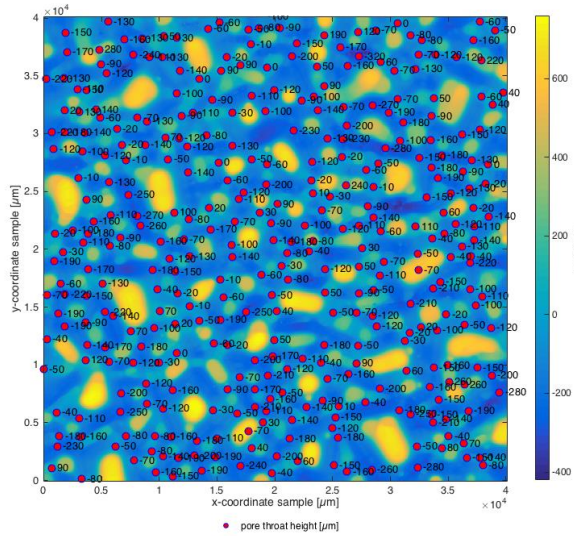

Figure A.11: Pore throats on Sample 1 topography. The patch shown is 4 x 4 cm.

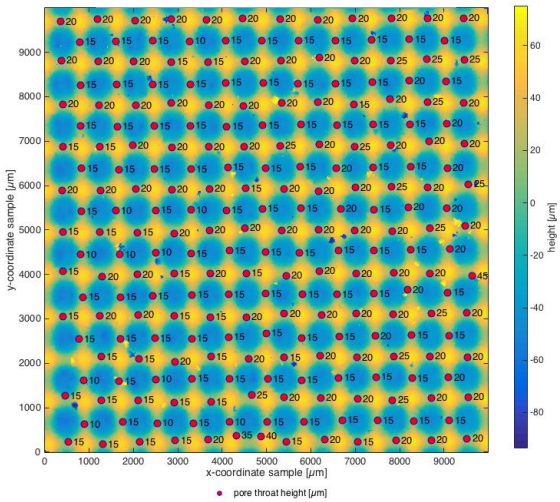

Figure A.12: Pore throats on Sample 2 topography. The patch shown is 1 x 1 cm.

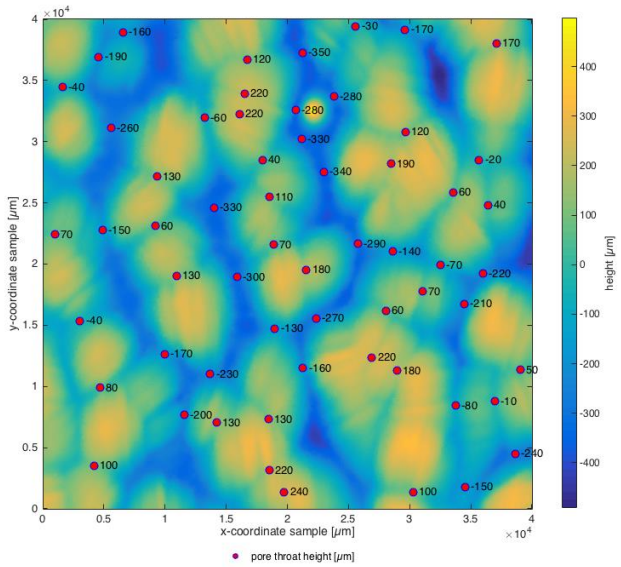

Figure A.13: Pore throats on Sample 3 topography. The patch shown is 4 x 4 cm.

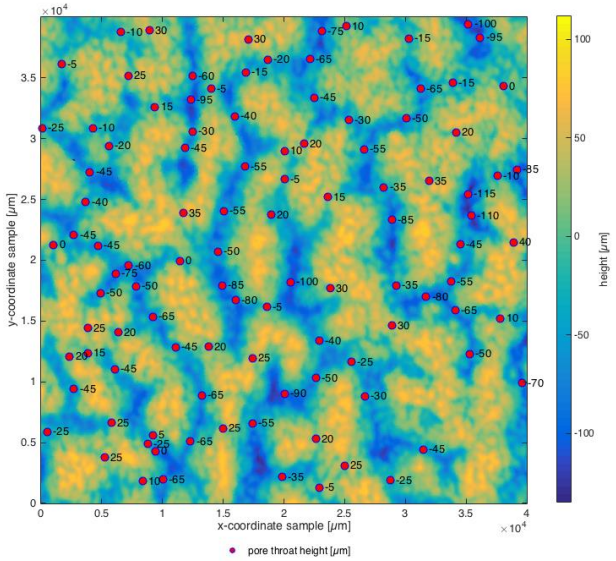

Figure A.14: Pore throats on Sample 4 topography. The patch shown is 4 x 4 cm.

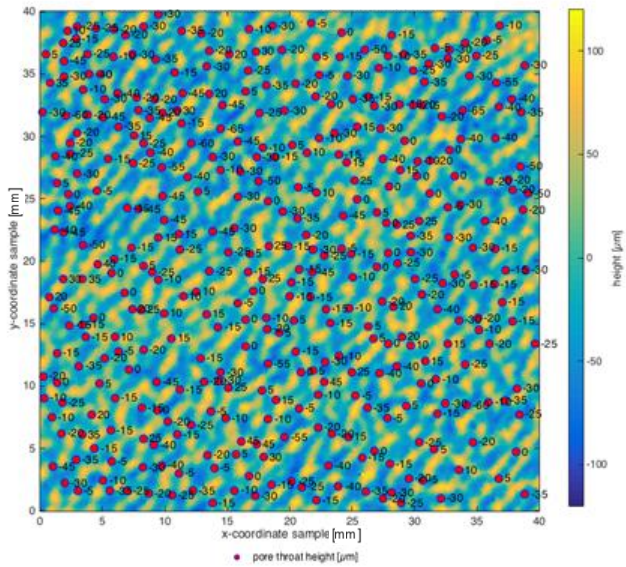

Figure A.15: Pore throats on Sample 5 topography. The patch shown is 4 x 4 cm.

A.4. PORE BODIES ON FRACTURE TOPOGRAPHY

Topography of fracture samples with conceptual pore bodies superimposed on images.

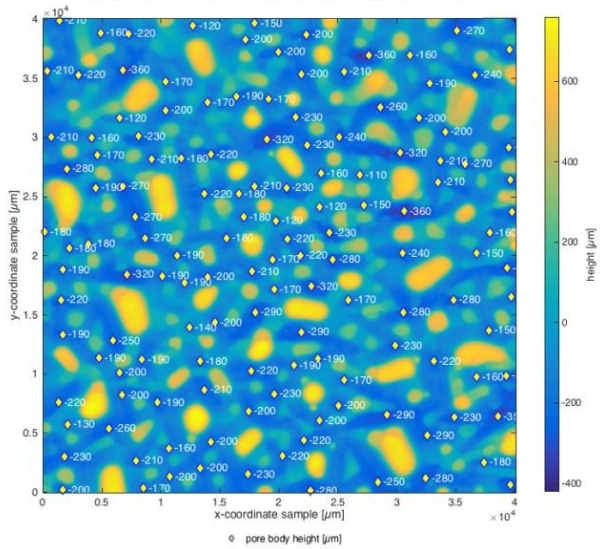

Figure A.16: Pore bodies on Sample 1 topography. The patch shown is 4 x 4 cm.

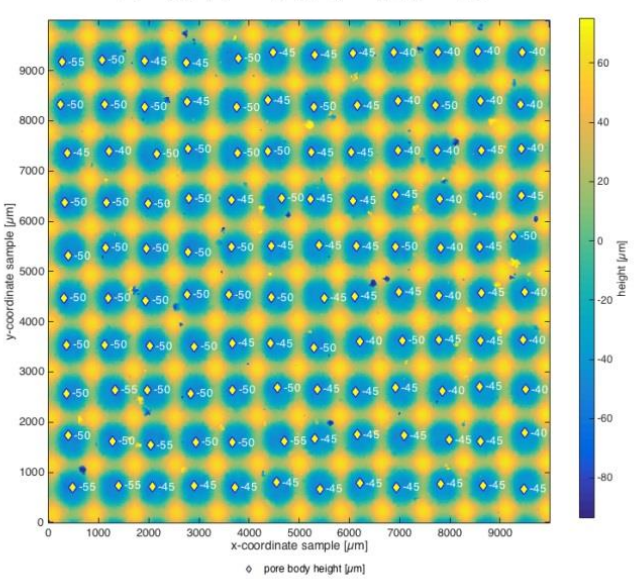

Figure A.17: Pore bodies on Sample 2 topography. The patch shown is 1 x 1 cm.

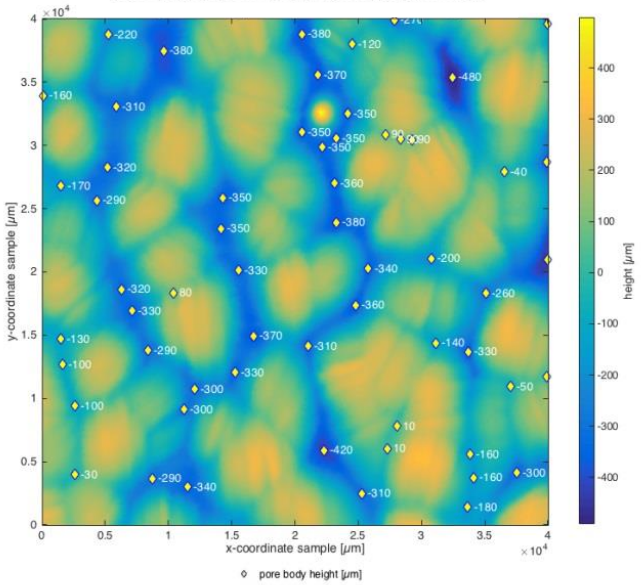

Figure A.18: Pore bodies on Sample 3 topography. The patch shown is 4 x 4 cm.

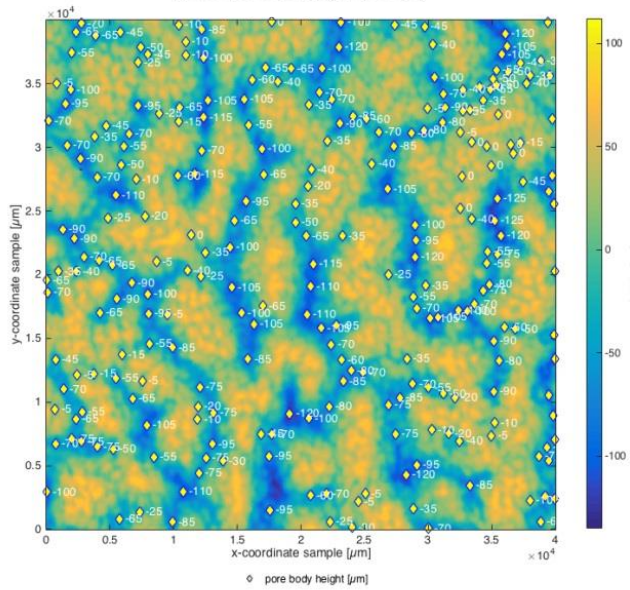

Figure A.19: Pore bodies on Sample 4 topography. The patch shown is 4 x 4 cm.

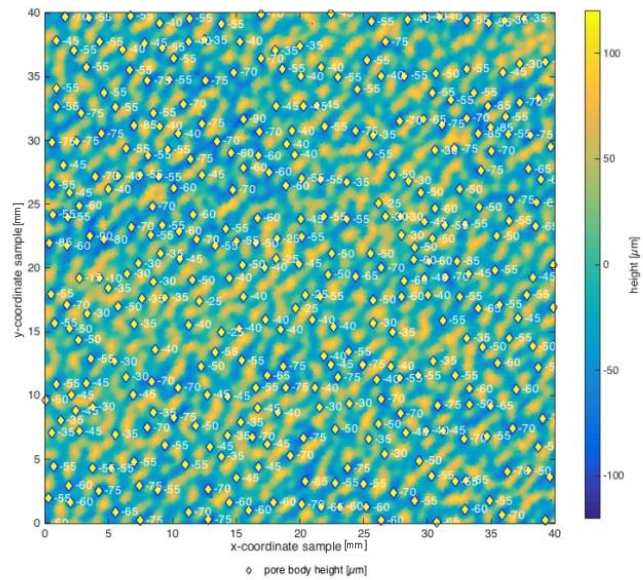

Figure A.20: Pore bodies on Sample 5 topography. The patch shown is 4 x 4 cm.

A.5. 2D NETWORK

The lines are drawn around the pore bodies and connect the pore throats of each pore. In some cases we exclude shallow saddle points within a pore body and count them as part of the larger pore body.

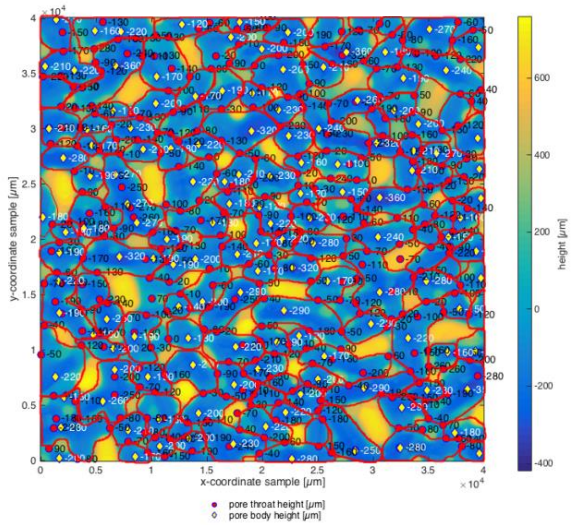

Figure A.21: 2D network of Sample 1. The patch shown is 4 x 4 cm.

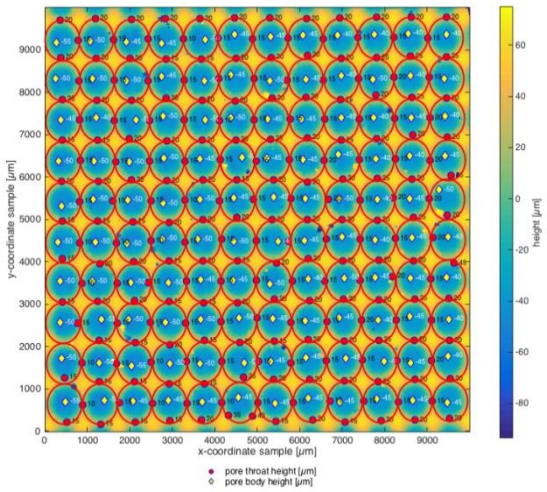

Figure A.22: 2D network of Sample 2. The patch shown is 1 x 1 cm.

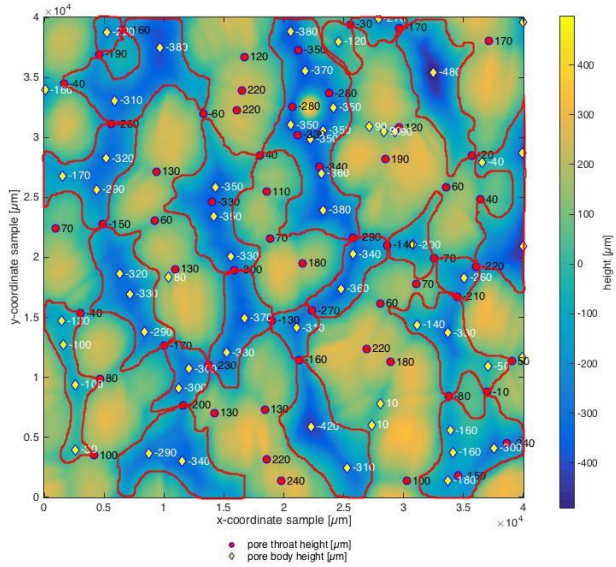

Figure A.23: 2D network of Sample 3. The patch shown is 4 x 4 cm.

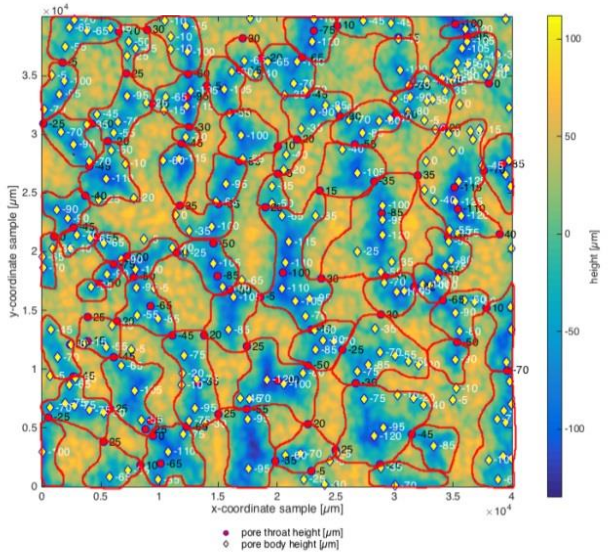

Figure A.24: 2D network of Sample 4. The patch shown is 4 x 4 cm.

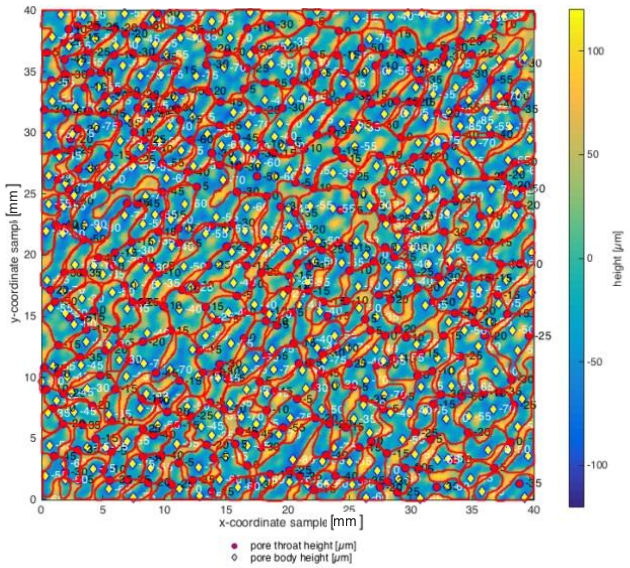

Figure A.25: 2D network of Sample 5. The patch shown is 4 x 4 cm.

B

APERTURE CORRELATION LENGTH

SEMI-VARIOGRAM analysis was conducted to quantify the special variation of the roughness. The correlation length for an aperture is an alternate measure of ganglion length.

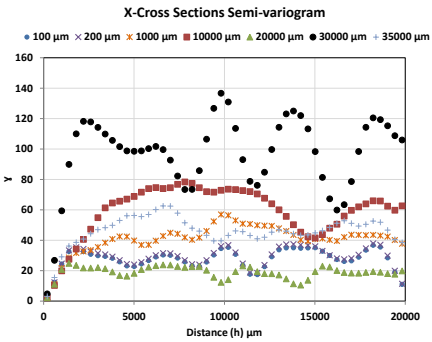

Figure B.1: Sample 1: semi-variogram in X-direction.

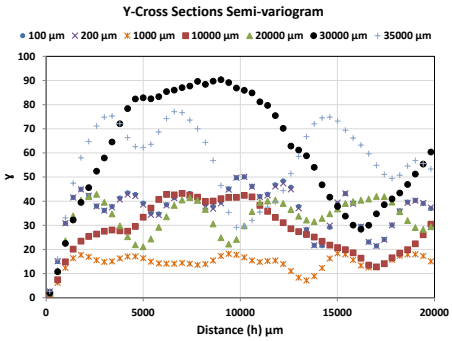

Figure B.2: Sample 1: semi-variogram in Y-direction.

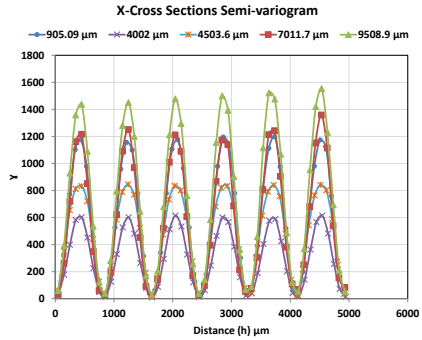

Figure B.3: Sample 2: semi-variogram in X-direction.

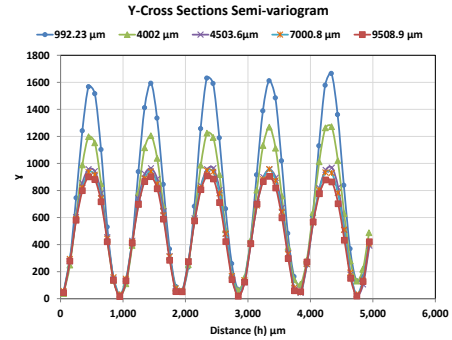

Figure B.4: Sample 2: semi-variogram in Y-direction.

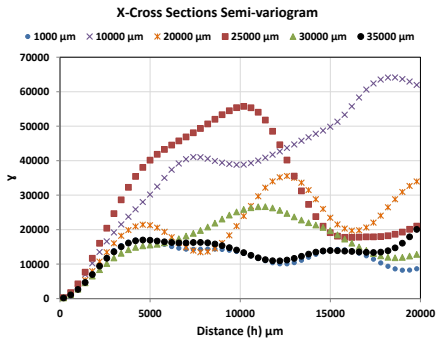

Figure B.5: Sample 3: semi-variogram in X-direction.

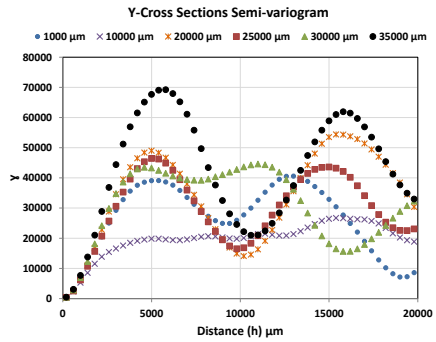

Figure B.6: Sample 3: semi-variogram in Y-direction.

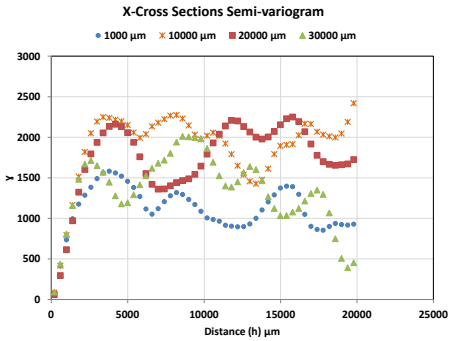

Figure B.7: Sample 4: semi-variogram in X-direction.

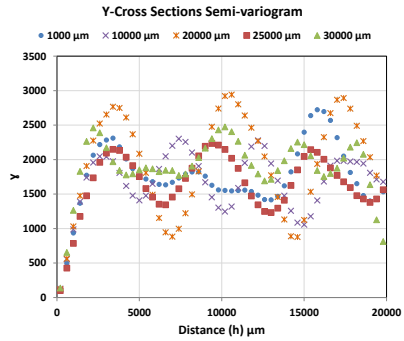

Figure B.8: Sample 4: semi-variogram in Y-direction.

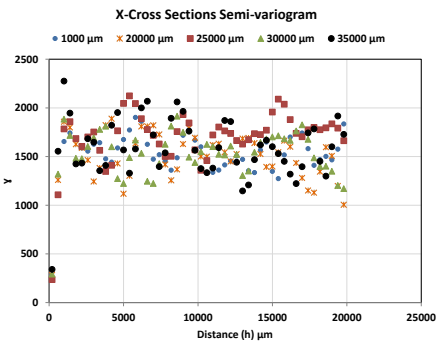

Figure B.9: Sample 5: semi-variogram in X-direction.

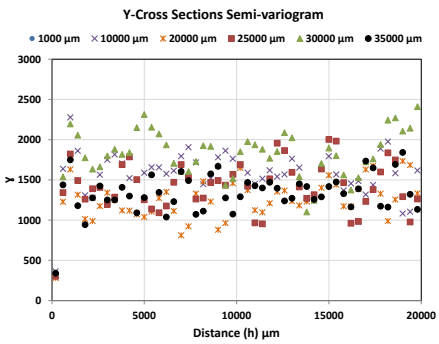

Figure B.10: Sample 5: semi-variogram in Y-direction.

C

HYDRAULIC APERTURE ESTIMATION AND PERCOLATION HEIGHT

C.1. RATE-PRESSURE GRADIENT RELATIONSHIP

Experimental rate-pressure gradient relationship for the hydraulic aperture estimation.

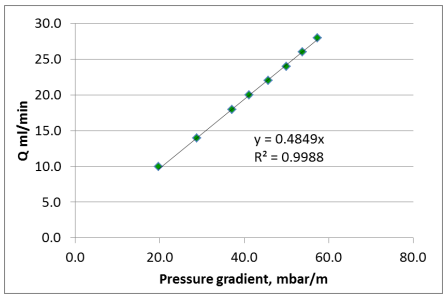

Figure C.1: Sample 1: injection rate vs. pressure gradient.

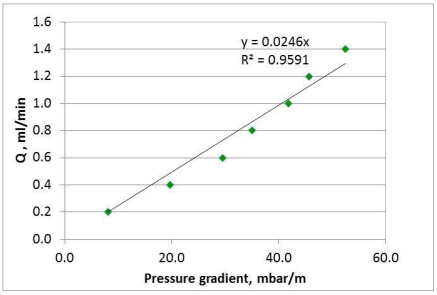

Figure C.2: Sample 2: injection rate vs. pressure gradient.

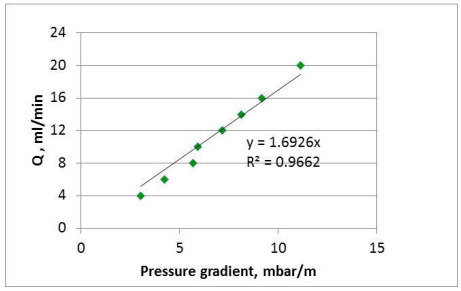

Figure C.3: Sample 3: injection rate vs. pressure gradient.

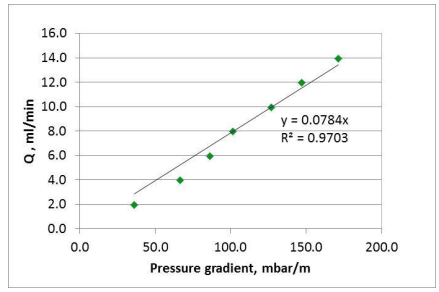

Figure C.4: Sample 4: injection rate vs. pressure gradient.

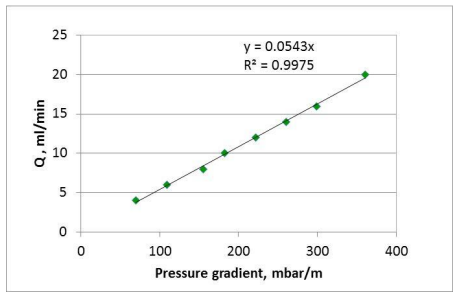

Figure C.5: Sample 5: injection rate vs. pressure gradient.

C.2. PERCOLATION HEIGHT

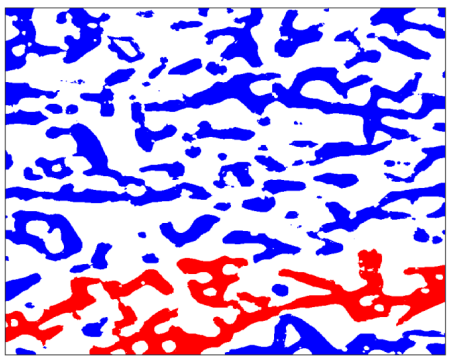

Figure C.6: Sample 1: percolation threshold. This is the height at which the fluid forms a continuous path across the patch in a specific direction; shown in red.

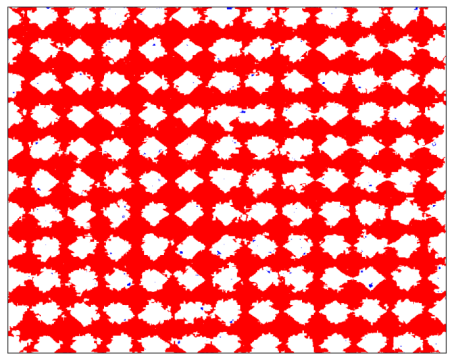

Figure C.7: Sample 2: percolation threshold. This is the height at which the fluid forms a continuous path across the patch in a specific direction; shown in red.

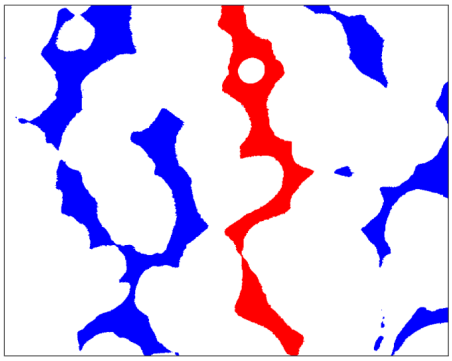

Figure C.8: Sample 3: percolation threshold. This is the height at which the fluid forms a continuous path across the patch in a specific direction; shown in red.

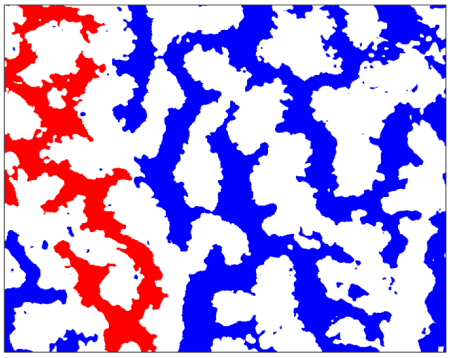

Figure C.9: Sample 4: percolation threshold. This is the height at which the fluid forms a continuous path across the patch in a specific direction; shown in red.

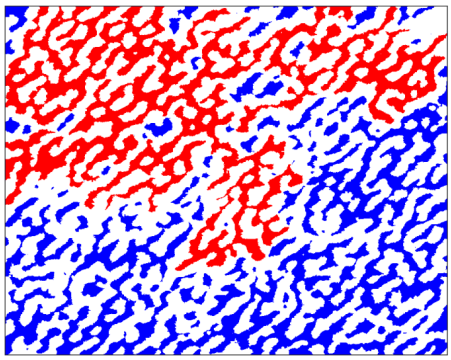

Figure C.10: Sample 5: percolation threshold. This is the height at which the fluid forms a continuous path across the patch in a specific direction; shown in red.

D

DESATURATION EXPERIMENTS

WATER is injected at 0.5 ml/min, in horizontal flow, until no further change in saturation is observed. The rate is increased and an image is taken when two conditions are satisfied: first, no further change in saturation is observed, and, second, the pressure is stable for at least 15 min. Successive images are taken with incremental increases in the injection rate until low residual saturation is achieved.

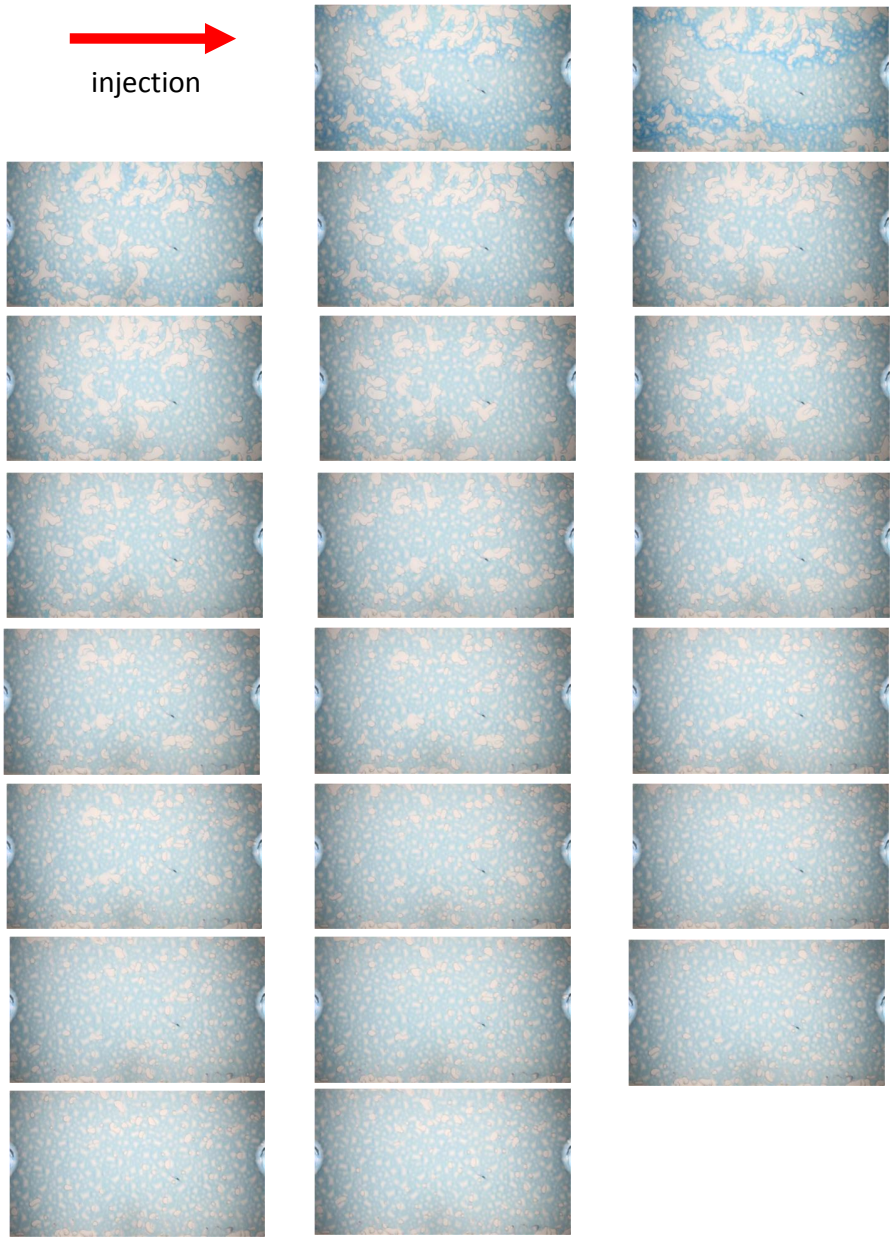

Figure D.1: Sample 1: unprocessed images of the desaturation experiment. Image sequence is left to right.

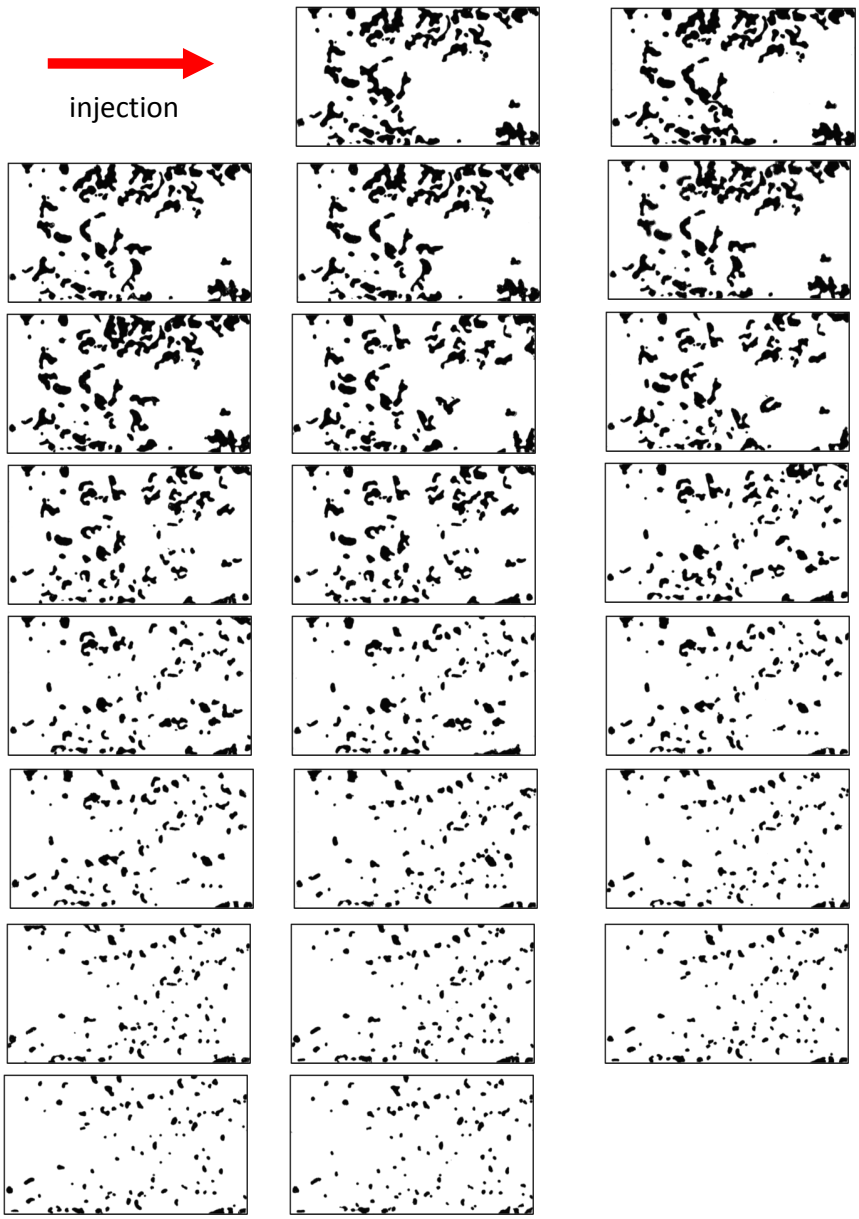

Figure D.2: Sample 1: processed images of the desaturation experiment. Image sequence is left to right.

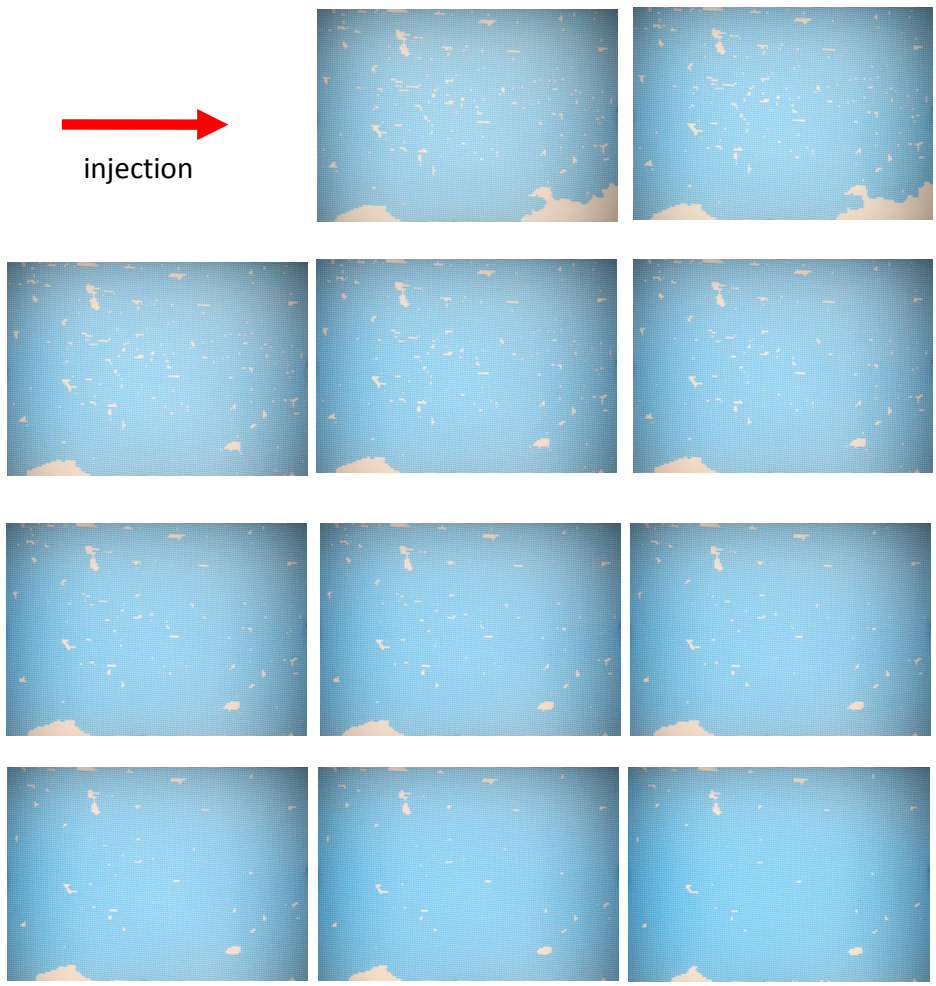

Figure D.3: Sample 2: unprocessed images of the desaturation experiment. Image sequence is left to right.

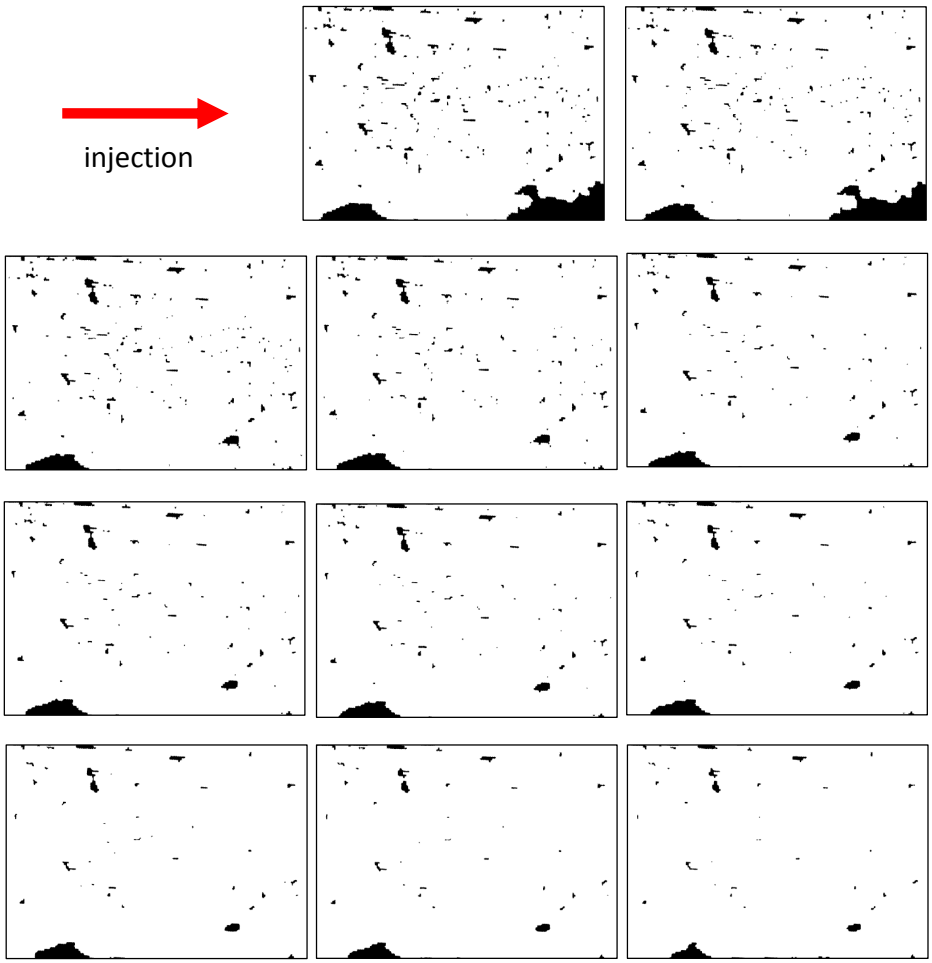

Figure D.4: Sample 2: processed images of the desaturation experiment. Image sequence is left to right.

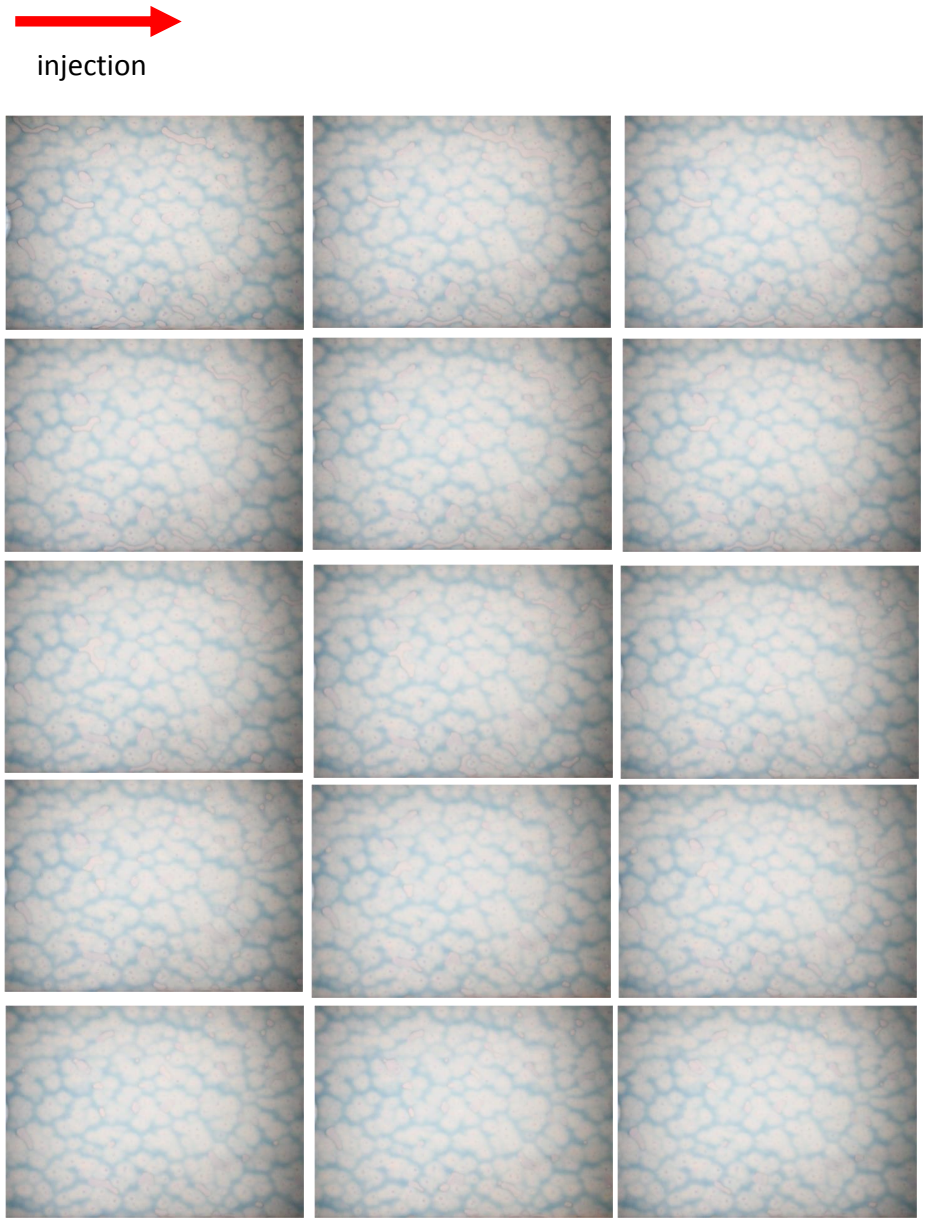

Figure D.5: Sample 3: unprocessed images of the desaturation experiment. Image sequence is left to right.

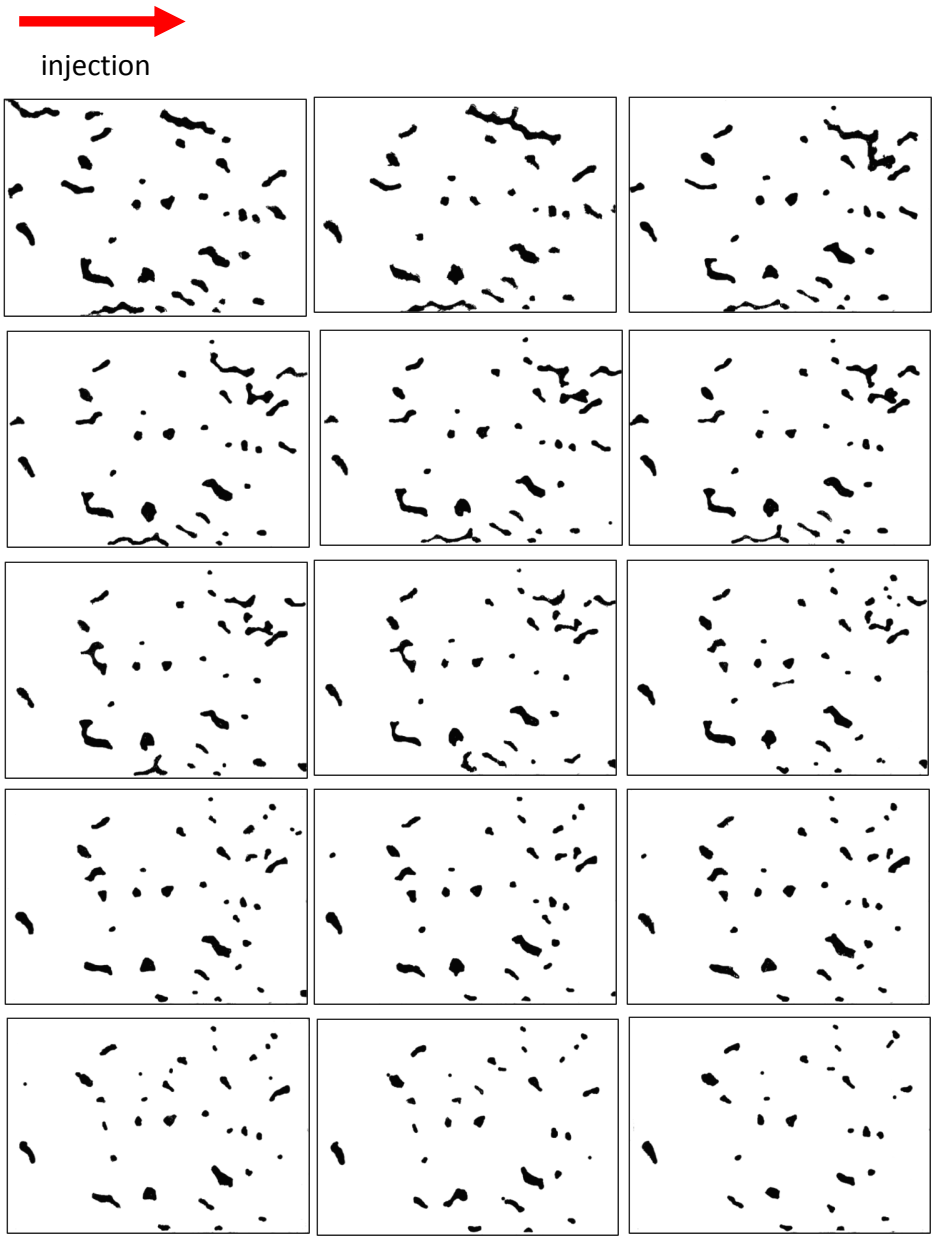

Figure D.6: Sample 3: processed images of the desaturation experiment. Image sequence is left to right.

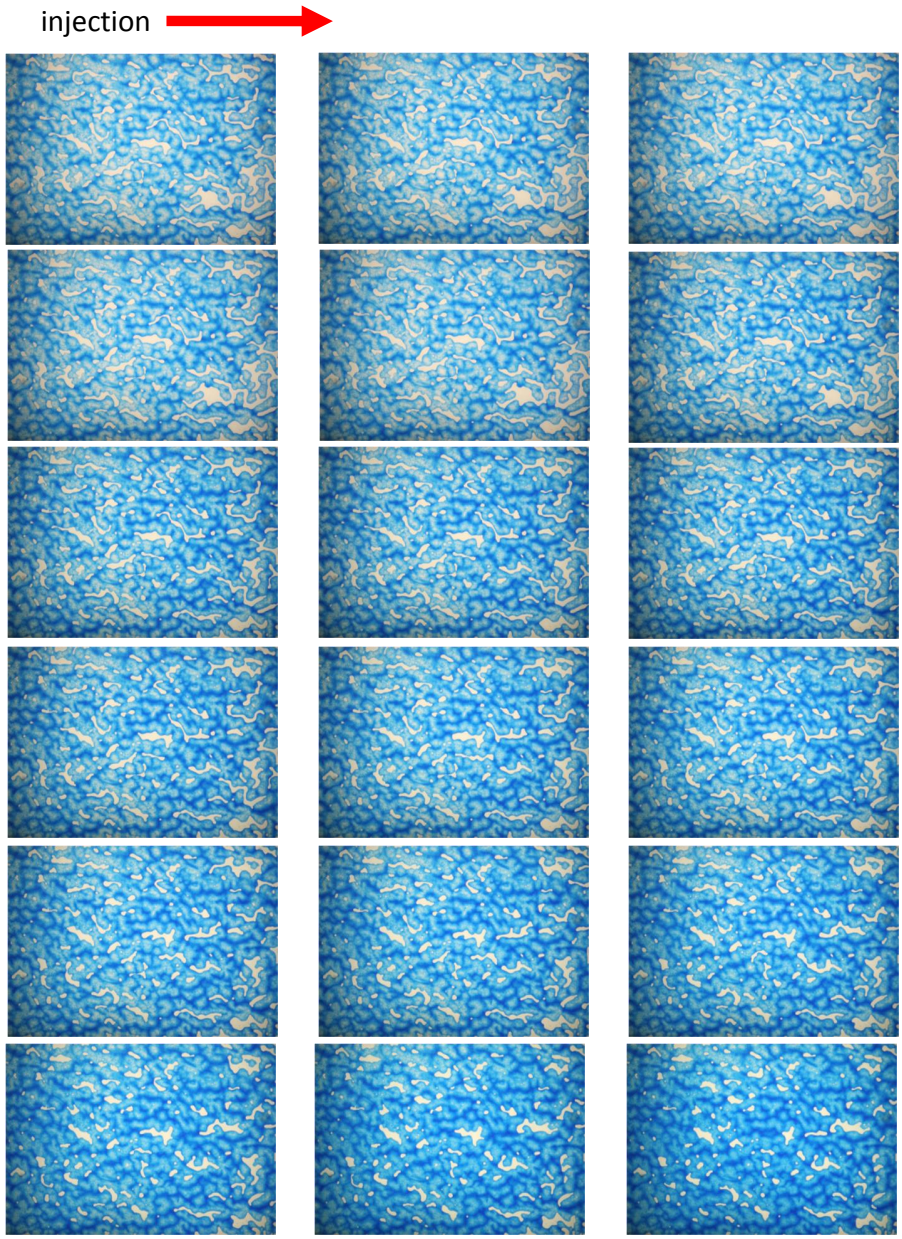

Figure D.7: Sample 4: unprocessed images of the desaturation experiment. Image sequence is left to right.

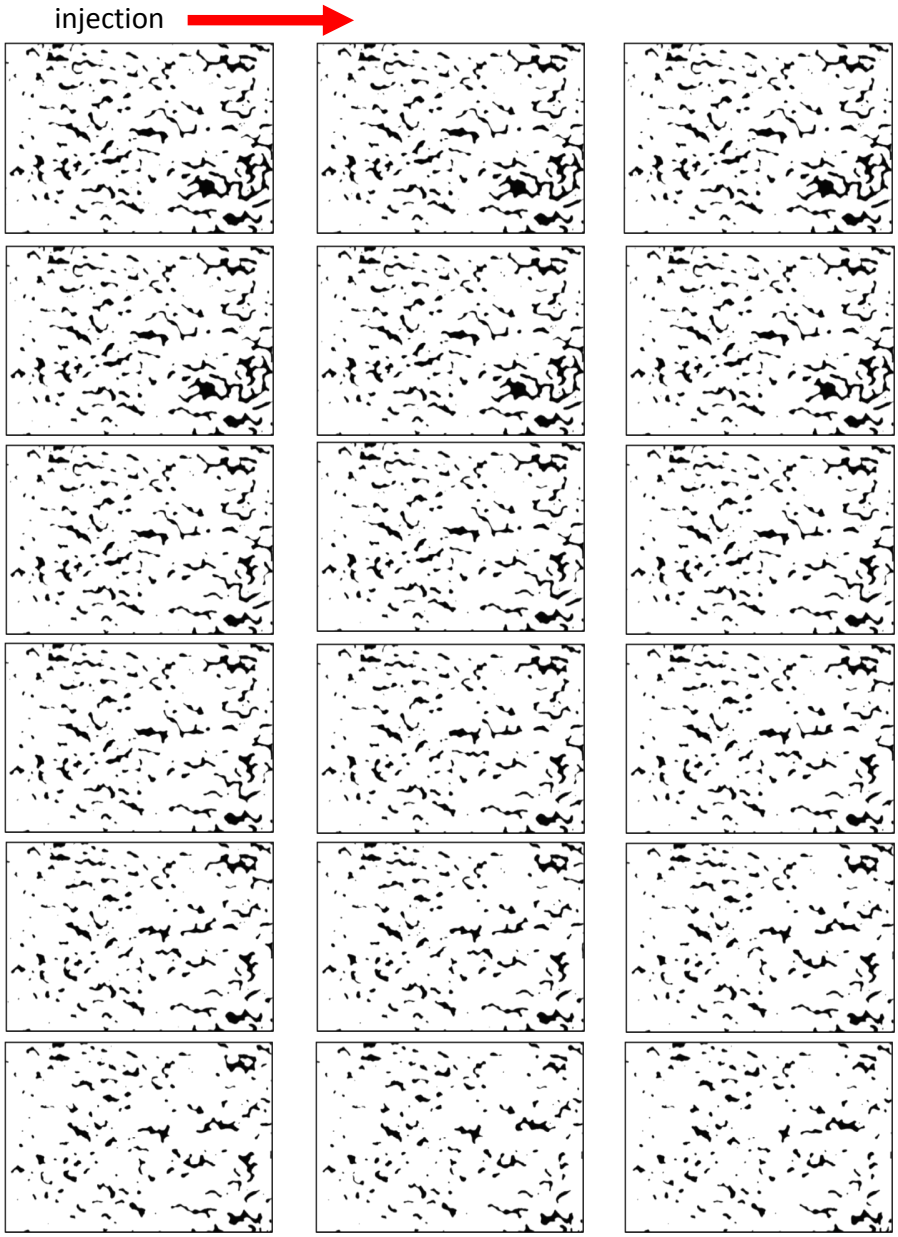

Figure D.8: Sample 4: processed images of the desaturation experiment. Image sequence is left to right.

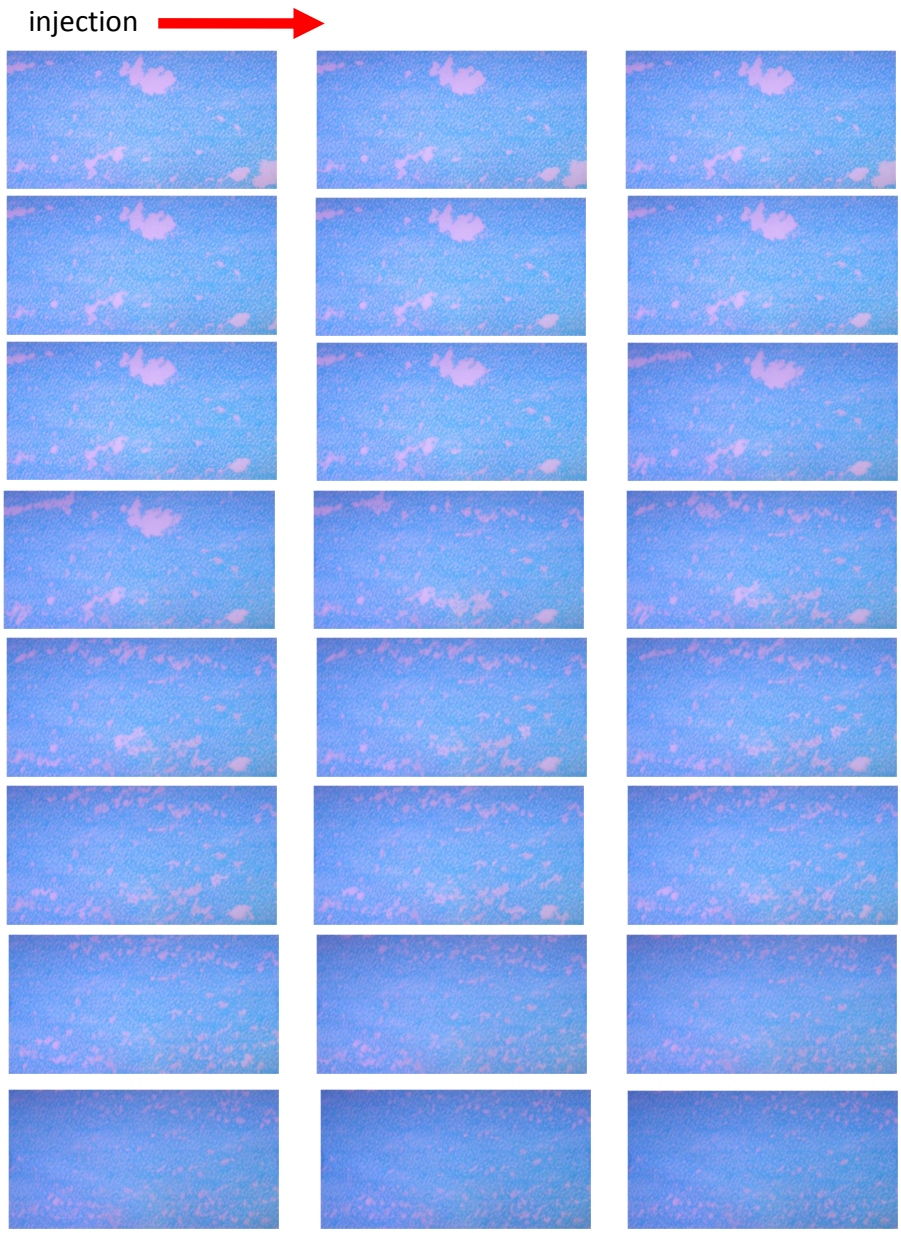

Figure D.9: Sample 5: unprocessed images of the desaturation experiment. Image sequence is left to right.

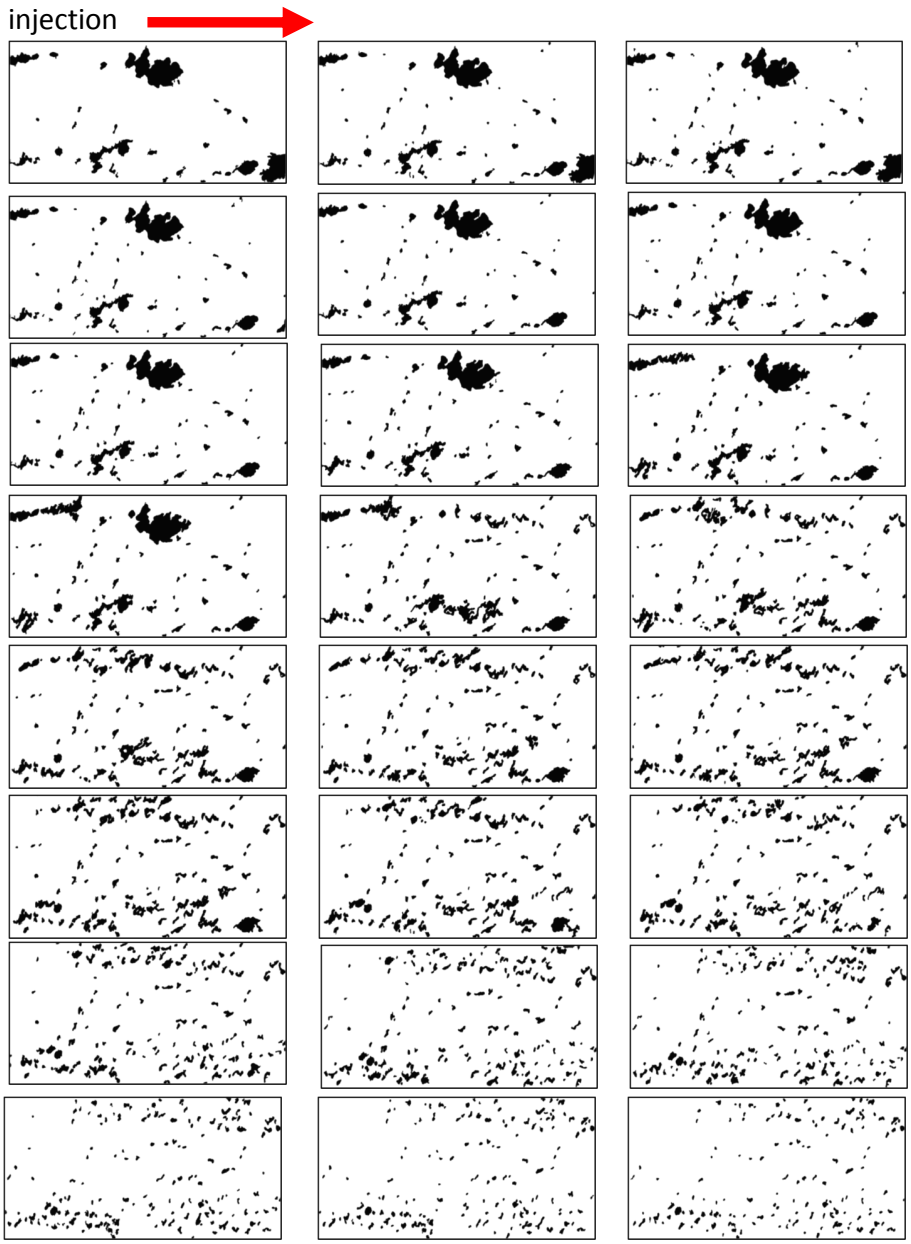

Figure D.10: Sample 5: processed images of the desaturation experiment. Image sequence is left to right.

E

TIME FOR COARSENING OF FOAM IN A FRACTURE

Consider for simplicity a single disk-shaped bubble of radius R between parallel plates, surrounded by a lamella and plateau borders along the plates. The curvature in the plane of the disk is $(1/R)$. For simplicity we neglect variations in the gap h between the plates. The rate of molar gas transfer through the lamella is given by

$$W = k_s \Delta c A \tag{E.1}$$

where W is the molar transfer rate, K_s is the mass transfer coefficient, Δc is the molar concentration difference in the gas on opposite sides of the lamella, and A is the lamella surface area ($\sim 2\pi Rh$) (Cussler, 2009). Δc can be related to the ideal gas law:

$$\Delta c = \frac{\Delta p}{R_{ID} T} \tag{E.2}$$

where Δp is the pressure difference across the lamella, R_{ID} is the ideal-gas constant, and T is the absolute temperature. Δp can be calculated based on the capillary pressure difference across a cylindrical bubble between parallel plates:

$$\Delta p = \frac{\gamma}{R} \tag{E.3}$$

where γ is the surface tension and R is the radius. A mass balance on the bubble yields the following expression:

$$\frac{dV}{dt} = 2\pi hR\frac{dR}{dt} = -\frac{W}{c} \tag{E.4}$$

$$\frac{dR^2}{dt} = \frac{-2k_s\gamma}{cR_{ID}T} \tag{E.5}$$

The solution of this question for a bubble initially with a radius R_0 is

$$R_0{}^2 - R^2 = \frac{-2k_s\gamma}{P} t \tag{E.6}$$

where P is the pressure which we assume for simplicity to be constant, R is the bubble radius at time t until the bubble disappears. K_s is 3.8×10^{-4} m/s for nitrogen gas with the surfactant solution we used (Farajzadeh et al., 2011), γ is 0.03 N/m and we take $P \approx 1.5\text{x}10^{-4}$ Pa (cf. Figure 3.11). An isolated bubble initially of 200 μm radius disappears by the diffusion of gas into its surroundings in 4 to 5 mins. This is only a rough estimate of diffusion time in our fracture but it is greater than the bubble residence time (typically 2-3 mins) in our fracture. This estimate applies to diffusion through a lamella in a dry foam. Diffusion through a comparatively thick liquid lens would be much slower, which explains the survival of the tiny bubbles in Figure 3.15, for instance.

We also observed the time for a small bubble to disappear by gas diffusion through lamellae in our model fracture. One cannot observe diffusion in rapidly flowing bubbles; therefore, we stopped the injection and waited for the bubble movement to stop. We started to record time and capture images. Figure E.1 shows a sequence of images illustrating bubble disappearance by gas diffusion. The bubbles eventually occupy entire pores by diffusion, as expected. We color some bubbles in red to highlight their disappearance by diffusion. The length of the big bubble, which disappears completely in 10 mins, is 270 μm. Its small neighbor disappears in 2 to 3 mins. This bubble resides in a pore throat between much larger bubbles in the pore bodies. Therefore, curvature in the direction perpendicular to the glass plates (from variation in aperture) may have increased the pressure difference and diffusion rate. Diffusive coarsening between similar-size bubbles in pore bodies would be expected to be slower.

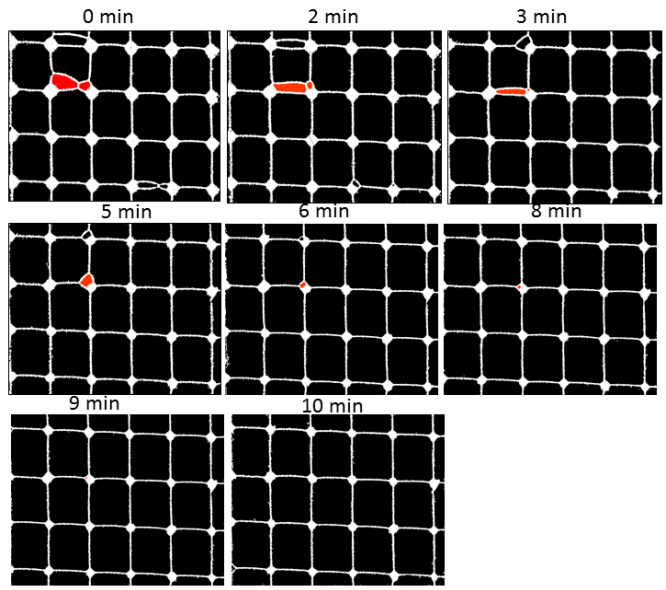

Figure E.1: A sequence of images that shows the time required for a bubble to disappear by gas diffusion. Image size is 0.44×0.35 cm; black is gas and white is water. A bubble of interest, highlighted in red, disappears in about 10 mins.

F

EFFECT OF GAS FRACTIONAL FLOW AND TOTAL-SUPERFICIAL VELOCITY ON FOAM TEXTURE IN A RANDOM ROUGH SAMPLE

THIS appendix shows the effect of increasing f_g on foam texture in a random-rough sample. This test was done on Sample 4. The images were captured in region 4 at roughly the same location. We observed the same behavior as seen in Sample 2; bubbles become larger as f_g increases (Figure F.1).

In Sample 4, we find that as u_t increases pressure gradinet increases; however, the average bubble size does not change greatly at fixed f_g (Figure F.2). It is thought that average bubble size is unchanging in the low-quality foam regime in 3D porous media (Rossen, 1996; Alvarez et al., 2001). Bubbles are thought to be as large as pores in that regime. The near-invariance of bubble size in (Figure F.2) is consistent with these findings, but bubbles are smaller than pores. It is possible that bubbles reflect a characteristic size for snap-off in the throats rather than the pore-body size. The error bar on the average bubble size represents the standard deviation of bubble-size distribution.

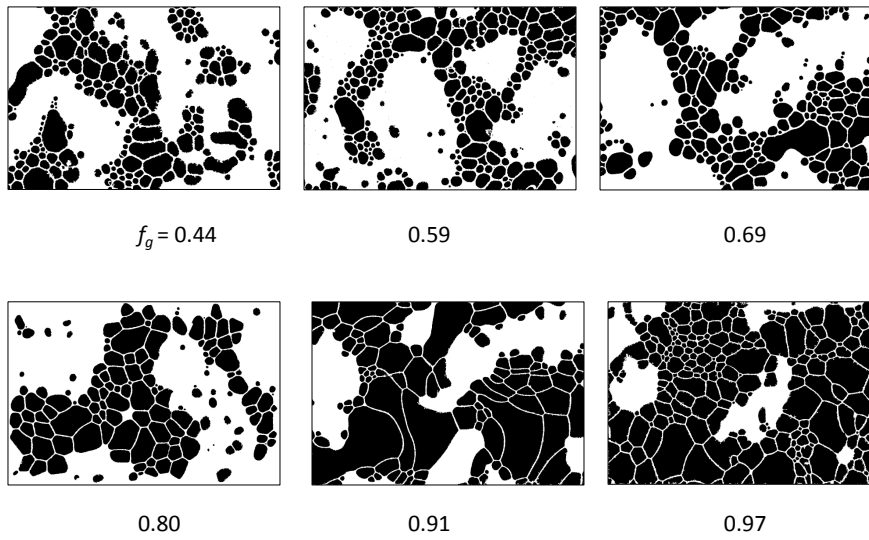

F

Figure F.1: Foam texture vs. f_g, (white is water and black is gas). Images were captured during stabilized pressure gradient 360 mm from the injection port). Image size is 2.4×1.8 cm.

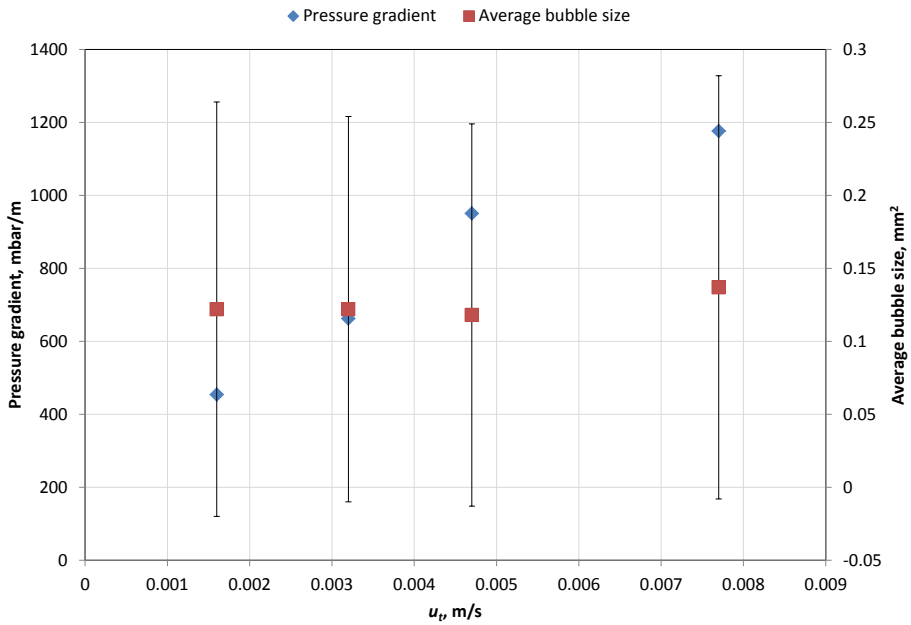

Figure F.2: Pressure gradient and average bubble size vs u_t at $f_g \approx 0.60$.

REFERENCES

Aguilera, R. (1995). *Naturally fractured reservoirs*. PennWell Books, Tulsa, Oklahoma, USA, 2nd edition.

Aguilera, R. (1999). Recovery factors and reserves in naturally fractured reservoirs. *Journal of Canadian Petroleum Technology*, 38(07):p. 15–18.

Al Adasani, A. and Bai, B. (2011). Analysis of eor projects and updated screening criteria. *Journal of Petroleum Science and Engineering*, 79(1):10–24.

Allan, J. and Sun, S. Q. (2003). Controls on recovery factor in fractured reservoirs: lessons learned from 100 fractured fields. In *Society of Petroleum Engineers*. Paper SPE-84590-MS presented at the SPE Annual Technical Conference and Exhibition, 5-8 October, Denver, Colorado, https://doi.org/10.2118/84590-MS.

AlQuaimi, B. I. and Rossen, W. R. (2017a). Capillary desaturation curve for residual nonwetting phase in natural fractures. *Submitted to Societry of Petroleum Engineers Journal*.

AlQuaimi, B. I. and Rossen, W. R. (2017b). Characterizing foam flow in fractures for enhanced oil recovery. In *European Symposium on Improved Oil Recovery*. Paper presented at IOR 2017-19th European Symposium on Improved Oil Recovery, Stavanger, Norway, doi:10.3997/2214-4609.201700336.

AlQuaimi, B. I. and Rossen, W. R. (2017c). New capillary number definition for displacement of residual nonwetting phase in natural fractures. *Geophysical Research Letters*, 44(11):5368–5373.

AlQuaimi, B. I. and Rossen, W. R. (2017d). Study of foam generation and propagation in fully characterized physical-model fracture. *Submitted to Colloids and Surfaces A: Physicochemical and Engineering Aspects*.

Alvarez, J. M., Rivas, H. J., and Rossen, W. R. (2001). Unified model for steady-state foam behavior at high and low foam qualities. *SPE journal*, 06(03):325–333.

Awan, A. R., Teigland, R., and Kleppe, J. (2006). Eor survey in the north sea. In *Society of Petroleum Engineers*. Paper SPE-99546-MS presented at the SPE/DOE Symposium on Improved Oil Recovery, 22-26 April, Tulsa, Oklahoma, USA, https://doi.org/10.2118/99546-MS.

Babadagli, T. et al. (2001). Selection of proper eor method for efficient matrix recovery in naturally fractured reservoirs. In *Society of Petroleum Engineers*. Paper SPE-69564-MS presented at SPE Latin American and Caribbean Petroleum Engineering Conference, 25-28 March, Buenos Aires, Argentina, https://doi.org/10.2118/69564-MS.

Barton, N. and Choubey, V. (1977). The shear strength of rock joints in theory and practice. *Rock mechanics*, 10(1):1–54.

Bernard, G. C., Holm, L., and Harvey, C. P. (1980). Use of surfactant to reduce co2 mobility in oil displacement. *Society of Petroleum Engineers Journal*, 20(04):281–292.

Bernard, G. G. and Holm, L. W. (1964). Effect of foam on permeability of porous media to gas. *SPE journal*, 4(3):267–274.

Bertotti, G., Immenhauser, A., and Koppen, J. K. J. T.-v. (2005). Stratigraphic and regional distribution of fractures in barremian–aptian carbonate rocks of eastern oman: outcrop data and their extrapolation to interior oman hydrocarbon reservoirs. *International Journal of Earth Sciences*, 94(3):447–461.

Bikerman, J. J. (2013). *Foams*, volume 10. Springer Science & Business Media.

Bird, R. B. (2002). Transport phenomena. *Applied Mechanics Reviews*, 55(1):R1–R4.

Blaker, T., Celius, H., Lie, T., Martinsen, H., Rasmussen, L., and Vassenden, F. (2002). Foam for gas mobility control in the snorre field: the fawag project. *SPE Reservoir Evaluation & Engineering*, 05(04).

Bond, D. C. and Holbrook, O. C. (1958). Gas drive oil recovery process. US Patent 2,866,507.

Bourbiaux, B., Fourno, A., Nguyen, Q.-L., Norrant, F., Robin, M., Rosenberg, E., and Argillier, J.-F. (2016). Experimental and numerical assessment of chemical enhanced oil recovery in oil-wet naturally fractured reservoirs. *SPE Journal*, 21(3).

Bourbiaux, B., Rosenberg, E., Robin, M., Chabert, M., Chevallier, E., and Gautier, S. (2017). Computed-tomography-scan monitoring of foam-based chemical-enhanced-oil-recovery processes in fractured carbonate cores. *SPE Journal*, 22(03).

British Petroleum, B. P. (2016). Bp statistical review of world energy.

Brown, S. R. (1987). Fluid flow through rock joints: the effect of surface roughness. *Journal of Geophysical Research: Solid Earth*, 92(B2):1337–1347.

Brown, S. R., Kranz, R. L., and Bonner, B. P. (1986). Correlation between the surfaces of natural rock joints. *Geophysical Research Letters*, 13(13):1430–1433.

Brown, S. R. and Scholz, C. H. (1985). Broad bandwidth study of the topography of natural rock surfaces. *J. geophys. Res*, 90(B14):12575–82.

Buchgraber, M., Castanier, L. M., and Kovscek, A. R. (2012). Microvisual investigation of foam flow in ideal fractures: role of fracture aperture and surface roughness. In *Society of Petroleum Engineers*. Paper SPE-159430-MS presented at SPE Annual Technical Conference and Exhibition, 8-10 October, San Antonio, Texas, https://doi.org/10.2118/159430-MS.

Chatzis, I. and Morrow, N. R. (1984). Correlation of capillary number relationships for sandstone. *SPE Journal*, 24(05).

Chatzis, I., Morrow, N. R., and Lim, H. T. (1983). Magnitude and detailed structure of residual oil saturation. *Soc. Pet. Eng. J.*, 23(2):311–326.

Chen, C. Y., Horne, R. N., and Fourar, M. (2004a). Experimental study of liquid-gas flow structure effects on relative permeabilities in a fracture. *Water Resources Research*, 40(8):W08301.

Chen, C. Y., Li, K., Horne, R. N., et al. (2004b). Experimental study of phase transformation effects on relative permeabilities in fractures. In *Society of Petroleum Engineers*. Paper SPE-90233-MS presented at the SPE Annual Technical Conference and Exhibition, 26-29 September, Houston, Texas, https://doi.org/10.2118/90233-MS.

Cosentino, L., Coury, Y., Daniel, J., Manceau, E., Ravenne, C., Van Lingen, P., Cole, J., Sengul, M., et al. (2001). Integrated study of a fractured middle east reservoir with stratiform super-k intervals-part 2: Upscaling and dual media simulation. In *Society of Petroleum Engineers*. Society of Petroleum Engineers, Paper SPE-SPE-68184-MS presented at SPE Middle East Oil Show, 17-20 March, Manama, Bahrain, https://doi.org/10.2118/68184-MS.

Cussler, E. L. (2009). *Diffusion: mass transfer in fluid systems*. Cambridge university press.

Dominguez, G. (1992). *Carbonate reservoir characterization: a geologic-engineering analysis*, volume 30. Elsevier, Lafayette, LA, U.S.A.

Eson, R. and Cooke, R. (1989). A comprehensive analysis of steam foam diverters and application methods. In *Society of Petroleum Engineers*. Paper SPE-18785-MS presented at SPE California Regional Meeting, 5-7 April, Bakersfield, California, https://doi.org/10.2118/18785-MS.

Ettinger, R., Radke, C., et al. (1992). Influence of texture on steady foam flow in berea sandstone. *SPE reservoir engineering*, 7(01):83–90.

Farajzadeh, R., Muruganathan, R., Rossen, W., and Krastev, R. (2011). Effect of gas type on foam film permeability and its implications for foam flow in porous media. *Advances in colloid and interface science*, 168(1):71–78.

Fernø, M. A., Gauteplass, J., Pancharoen, M., Haugen, s., Graue, A., Kovscek, A. R., and Hirasaki, G. (2016). Experimental study of foam generation, sweep efficiency, and flow in a fracture network. *SPE journal*, 21(4):1140.

Fjelde, I., Zuta, J., and Duyilemi, O. V. (2008). Oil recovery from matrix during co2-foam flooding of fractured carbonate oil reservoirs. In *Europec/EAGE Conference and Exhibition, 9-12 June 2008, Rome*. Society of Petroleum Engineers.

Fourar, M., Bories, S., and Lenormand, R. (1992). Experimental study of two-phase flow in rough fractures. *Proceedings, seventeenth workshop on geothermal reservoir engineering. Stanford University, Stanford, California*, pages 215–218.

Fried, A. N. (1961). *The foam-drive process for increasing the recovery of oil*. US Department of the Interior, Bureau of Mines.

Friedmann, F., Hughes, T., Smith, M., Hild, G., Wilson, A., and Davies, S. (1997). Development and testing of a new foam-gel technology to improve conformance of the rangely co2 flood. In *Society of Petroleum Engineers*. Paper SPE-38837-MS presented at SPE Annual Technical Conference and Exhibition, 5-8 October, San Antonio, Texas, https://doi.org/10.2118/38837-MS.

Gauteplass, J., Chaudhary, K., Kovscek, A. R., and Fernø, M. A. (2015). Pore-level foam generation and flow for mobility control in fractured systems. *Colloids and Surfaces A: Physicochemical and Engineering Aspects*, 468:184–192.

Hakami, E. and Larsson, E. (1996). Aperture measurements and flow experiments on a single natural fracture. In *International Journal of Rock Mechanics and Mining Sciences & Geomechanics Abstracts*, volume 33, pages 395–404. Elsevier.

Haugen, s., Fernø, M. A., Graue, A., and Bertin, H. J. (2012). Experimental study of foam flow in fractured oil-wet limestone for enhanced oil recovery. *SPE Reservoir Evaluation & Engineering*, 15(02):218–228.

Haugen, s., Mani, N., Svenningsen, S., Brattekås, B., Graue, A., Ersland, G., and Fernø, M. A. (2014). Miscible and immiscible foam injection for mobility control and eor in fractured oil-wet carbonate rocks. *Transport in porous media*, 104(1):109–131.

Hermansen, H., Thomas, L., Sylte, J., and Aasboe, B. (1997). Twenty five years of ekofisk reservoir management. In *Society of Petroleum Engineers*. Paper SPE-38927 presented at the SPE Annual Technical Conference and Exhibition, 5-8 October, San Antonio, Texas, https://doi.org/10.2118/38927-MS.

Hirasaki, G. and Lawson, J. (1985). Mechanisms of foam flow in porous media: apparent viscosity in smooth capillaries. *Society of Petroleum Engineers Journal*, 25(02):176–190.

Holm, L. (1970). Foam injection test in the siggins field, illinois. *Journal of Petroleum Technology*, 22(12):1,499–1,506.

Holm, L. W. (1968). The mechanism of gas and liquid flow through porous media in the presence of foam. *SPE journal*, 8(4):359–369.

Hughes, R. G. and Blunt, M. J. (2001). Network modeling of multiphase flow in fractures. *Advances in Water Resources*, 24(3–4):409–421.

Huh, D. G. and Handy, L. L. (1989). Comparison of steady and unsteady-state flow of gas and foaming solution in porous media. *SPE Reservoir Engineering*, 4(1):77–84.

Izadi, M., Shadizadeh, S. R., and Moradi, S. (2012). Experimentally measurements of relative permeability in fractured core. *International Journal of Science & Emerging Technologies*, 3(2).

Jakobsson, N. and Christian, T. (1994). Historical performance of gas injection of ekofisk. In *Society of Petroleum Engineers*. Paper SPE-28933-MS presented at the SPE Annual Technical Conference and Exhibition, 25-28 September, New Orleans, Louisiana,https://doi.org/10.2118/28933-MS.

Johns, R. A., Steude, J. S., Castanier, L. M., and Roberts, P. V. (1993). Nondestructive measurements of fracture aperture in crystalline rock cores using x ray computed tomography. *Journal of Geophysical Research: Solid Earth*, 98(B2):1889–1900.

Kalra, S. and Wu, X. (2014). Co2 injection for enhanced gas recovery. In *Society of Petroleum Engineers*. Paper SPE-169578-MS presented at SPE Western North American and Rocky Mountain Joint Meeting, 17-18 April, Denver, Colorado, https://doi.org/10.2118/169578-MS.

Kam, S., Frenier, W., Davies, S., and Rossen, W. (2007). Experimental study of high-temperature foam for acid diversion. *Journal of Petroleum Science and Engineering*, 58(1):138–160.

Kamal, M. and Marsden Jr, S. (1973). Displacement of a micellar slug foam in unconsolidated porous media. In *Society of Petroleum Engineers*. Paper SPE-4584-MS presented at Fall Meeting of the Society of Petroleum Engineers of AIME, 30, September-3 October, Las Vegas, Nevada, https://doi.org/10.2118/4584-MS.

Kantzas, A., Chatzis, I., and Dullien, F. (1988). Enhanced oil recovery by inert gas injection. In *Society of Petroleum Engineers*. Paper SPE-17379-MS presented at SPE Enhanced Oil Recovery Symposium, 16-21 April, Tulsa, Oklahoma, https://doi.org/10.2118/17379-MS.

Karpyn, Z., Grader, A., and Halleck, P. (2007). Visualization of fluid occupancy in a rough fracture using micro-tomography. *Journal of colloid and interface science*, 307(1):181–187.

Khatib, Z., Hirasaki, G., and Falls, A. (1988). Effects of capillary pressure on coalescence and phase mobilities in foams flowing through porous media. *SPE reservoir engineering*, 3(03):919–926.

Kim, J., Dong, Y., and Rossen, W. R. (2005). Steady-state flow behavior of co2 foam. *SPE journal*, 10(04):405–415.

Kovscek, A., Tretheway, D., Persoff, P., and Radke, C. (1995). Foam flow through a transparent rough-walled rock fracture. *Journal of Petroleum Science and Engineering*, 13(2):75–86.

Lake, L. W., Johns, R., Rossen, W., and Pope, G. (1986). *Fundamentals of enhanced oil recovery*. Society of Petroleum Engineers.

Lang, P., Paluszny, A., and Zimmerman, R. (2015). Hydraulic sealing due to pressure solution contact zone growth in siliciclastic rock fractures. *Journal of Geophysical Research: Solid Earth*, 120(6):4080–4101.

Lang, P. S., Paluszny, A., and Zimmerman, R. W. (2016). Evolution of fracture normal stiffness due to pressure dissolution and precipitation. *International Journal of Rock Mechanics and Mining Sciences*, 88:12–22.

Larson, R. G., Davis, H. T., and Scriven, L. E. (1981). Displacement of residual nonwetting fluid from porous media. *Chemical Engineering Science*, 36(1):75–85.

Lenormand, R., Zarcone, C., and Sarr, A. (1983). Mechanisms of the displacement of one fluid by another in a network of capillary ducts. *Journal of Fluid Mechanics*, 135:337–353.

Lian, P. and Cheng, L. (2012). The characteristics of relative permeability curves in naturally fractured carbonate reservoirs. *Journal of Canadian Petroleum Technology*, 51(02):137–142.

Malik, Q. M. and Islam, M. (2000). Co2 injection in the weyburn field of canada: optimization of enhanced oil recovery and greenhouse gas storage with horizontal wells. In *Society of Petroleum Engineers*. Paper SPE-59327-MS presented at SPE/DOE Improved Oil Recovery Symposium, 3-5 April, Tulsa, Oklahoma, https://doi.org/10.2118/59327-MS.

Maloney, D. and Doggett, K. (1997). Multiphase flow in fractures. *SCA-9730*.

Manrique, E. J., Muci, V. E., and Gurfinkel, M. E. (2007). Eor field experiences in carbonate reservoirs in the united states. *SPE Reservoir Evaluation & Engineering*, 10(6).

Mayer, A. S. and Miller, C. T. (1992). The influence of porous medium characteristics and measurement scale on pore-scale distributions of residual nonaqueous-phase liquids. *Journal of Contaminant Hydrology*, 11(3):189–213.

Minne, J. and Gartner, J. (1979). Fracture detection in the middle east. In *Society of Petroleum Engineers*. Paper SPE-7773-MS presented at Middle East Technical Conference and Exhibition, 25-28 February, Bahrain, https://doi.org/10.2118/7773-MS.

Montgomery, S. L. and Morgan, C. D. (1998). Bluebell field, uinta basin: Reservoir characterization for improved well completion and oil recovery. *AAPG bulletin*, 82(6):1113–1132.

Moore, T. and Slobod, R. (1955). Displacement of oil by water-effect of wettability, rate, and viscosity on recovery. In *Society of Petroleum Engineers*. Paper SPE-502-G presented at Fall Meeting of the Petroleum Branch of AIME, 2-5 October, New Orleans, Louisiana, https://doi.org/10.2118/502-G.

Morrow, N. R., Brower, K. R., Ma, S., and Buckley, J. S. (1990). Fluid flow in healed tectonic fractures. *Journal of Petroleum Technology*, 42(10):1,310–1,318.

Narr, W., Schechter, D. W., and Thompson, L. B. (2006). *Naturally fractured reservoir characterization*. Richardson, TX: Society of Petroleum Engineers.

Nasr-El-Din, H. A., Chesson, J. B., Cawiezel, K. E., and De Vine, C. S. (2006). Field success in carbonate acid diversion, utilizing laboratory data generated by parallel flow testing. In *Society of Petroleum Engineers*. Paper SPE-102828-MS presented at SPE Annual Technical Conference and Exhibition, 24-27 September, San Antonio, Texas, USA, https://doi.org/10.2118/102828-MS.

Nelson, R. (2001). *Geologic analysis of naturally fractured reservoirs*. Gulf Professional Publishing, Woburn, MA, USA, 2nd edition.

Nonnekes, L. E., Cox, S. J., and Rossen, W. R. (2015). Effect of gas diffusion on mobility of foam for enhanced oil recovery. *Transport in Porous Media*, 106(3):669–689.

Ocampo-Florez, A., Restrepo, A., Rendon, N., Coronado, J., Correa, J. A., Ramirez, D. A., Torres, M., Sanabria, R., and Lopera, S. H. (2014). Foams prove effectiveness for gas injection conformance and sweep efficiency improvement in a low porosity fractured reservoir–field pilots. In *Society of Petroleum Engineers*. Paper IPTC-17950-MS presented at International Petroleum Technology Conference, 10-12 December, Kuala Lumpur, Malaysia, https://doi.org/10.2523/IPTC-17950-MS.

Odling, N. (1994). Natural fracture profiles, fractal dimension and joint roughness coefficients. *Rock mechanics and rock engineering*, 27(3):135–153.

Odling, N. E. and Roden, J. E. (1997). Contaminant transport in fractured rocks with significant matrix permeability, using natural fracture geometries. *Journal of contaminant hydrology*, 27(3):263–283.

Olsson, R. and Barton, N. (2001). An improved model for hydromechanical coupling during shearing of rock joints. *International Journal of Rock Mechanics and Mining Sciences*, 38(3):317–329.

Oron, A. P. and Berkowitz, B. (1998). Flow in rock fractures: The local cubic law assumption reexamined. *Water Resources Research*, 34(11):2811–2825.

Osterloh, W. and Jante, M. (1992). Effects of gas and liquid velocity on steady-state foam flow at high temperature. In *Society of Petroleum Engineers*. Paper SPE-24179-MS presented at SPE/DOE Enhanced Oil Recovery Symposium, 22-24 April, Tulsa, Oklahoma, https://doi.org/10.2118/24179-MS.

Ozkaya, S. I. (2007). Detection of fracture corridors from openhole logs in horizontal wells. In *Society of Petroleum Engineers*. Paper SPE-110942-MS presented at SPE Saudi Arabia Section Technical Symposium, 7-8 May, Dhahran, Saudi Arabia, https://doi.org/10.2118/110942-MS.

Patzek, T. W. (1996). Field applications of steam foam for mobility improvement and profile control. *SPE Reservoir Engineering*, 11(02):79–86.

Persoff, P. and Pruess, K. (1995). Two-phase flow visualization and relative permeability measurement in natural rough-walled rock fractures. *Water Resources Research*, 31(5):1175–1186.

Phelps, R. E. and Strauss, J. P. (2002). Capturing reservoir behavior by simulating vertical fracture and super-k zones in the ghawar field. *SPE Reservoir Evaluation & Engineering*, 5(04):333–340.

Pieters, D. and Graves, R. (1994). Fracture relative permeability: linear or non-linear function of saturation. In *Society of Petroleum Engineers*. Paper SPE-28701-MS presented at International Petroleum Conference and Exhibition of Mexico, 10-13 October, Veracruz, Mexico, https://doi.org/10.2118/28701-MS.

Pope, G. A. (1980). The application of fractional flow theory to enhanced oil recovery. *Society of Petroleum Engineers Journal*, 20(03):191–205.

Pruess, K. and Tsang, Y. W. (1990). On two-phase relative permeability and capillary pressure of rough-walled rock fractures. *Water Resources Research*, 26(9):1915–1926.

Pyrak-Nolte, L. J., Cook, N. G., and Nolte, D. D. (1988). Fluid percolation through single fractures. *Geophysical Research Letters*, 15(11):1247–1250.

Qian, J., Chen, Z., Zhan, H., and Guan, H. (2011). Experimental study of the effect of roughness and reynolds number on fluid flow in rough-walled single fractures: a check of local cubic law. *Hydrological Processes*, 25(4):614–622.

Rabbani, A., Jamshidi, S., and Salehi, S. (2014). An automated simple algorithm for realistic pore network extraction from micro-tomography images. *Journal of Petroleum Science and Engineering*, 123:164–171.

Ramspott, L., Ballou, L., Carlson, R., Montan, D., Butkovich, T., Duncan, J., Patrick, W., Wilder, D., Brough, W., and Mayr, M. (1979). Technical concept for test of geologic storage of spent reactor fuel in the climax granite, nevada test site. Report UCID–18197; TRN: 79:015546 United StatesTRN: 79:015546Mon Feb 04 15:44:52 EST 2008NTIS, PC A04/MF A01LLNL; SCA: 050900; PA: ERA-04:045988; EDB-79:092686; NNS-85:000189; SN: 85000189English.

Ransohoff, T. and Radke, C. (1988). Mechanisms of foam generation in glass-bead packs. *SPE reservoir engineering*, 3(02):573–585.

Rao, D. (2001). Gas injection eor-a new meaning in the new millennium. *Journal of Canadian Petroleum Technology*, 40(02).

Raza, S. and Marsden, S. (1965). The flow of foam: I. rheology and streaming potential. In *Society of Petroleum Engineers*. Paper SPE-1205-MS presented at Fall Meeting of the Society of Petroleum Engineers of AIME, 3-6 October, Denver, Colorado, https://doi.org/10.2118/1205-MS.

Reed, R. L. and Healy, R. N. (1977). Some physicochemical aspects of microemulsion flooding: a review. *Improved Oil Recovery by Surfactant and Polymer Flooding*, pages 383–437.

Rodríguez, F., Ortega, G., Sánchez, J., Jiménez, O., et al. (2001). Reservoir management issues in the cantarell nitrogen injection project. In *Society of Petroleum Engineers*. Paper OTC-13178-MS presented at Offshore Technology Conference, 30 April-3 May, Houston, 3-6 October, Texas, https://doi.org/10.4043/13178-MS.

Romm, E. (1966). Flow characteristics of fractured rocks. *Nedra, Moscow*, 283.

Rossen, W. and Kumar, A. T. (1992). Single-and two-phase flow in natural fractures. In *Society of Petroleum Engineers*. Paper SPE-24915-MS presented at SPE Annual Technical Conference and Exhibition, 4-7 October, Washington, D.C., https://doi.org/10.2118/24915-MS.

Rossen, W. and Wang, M. (1999). Modeling foams for acid diversion. *SPE journal*, 4(2):92–100.

Rossen, W. R. (1996). Foams in enhanced oil recovery. *Surfactant Science Series*, pages 413–464.

Rossen, W. R. (2003). A critical review of roof snap-off as a mechanism of steady-state foam generation in homogeneous porous media. *Colloids and Surfaces A: Physicochemical and Engineering Aspects*, 225(1):1–24.

Sanchez Bujanos, J. L., Abundes, A., Valeriano, A., Morales, J., Rodriguez Torres, A., et al. (2005). Nitrogen injection in the cantarell complex: results after four years of operation. In *Society of Petroleum Engineers*. Paper SPE-97385-MS presented at SPE Latin American and Caribbean Petroleum Engineering Conference, 20-23 June, Rio de Janeiro, Brazil, https://doi.org/10.2118/97385-MS.

Schechter, D. S., McDonald, P., Sheffield, T., Baker, R., et al. (1996). Reservoir characterization and co2 pilot design in the naturally fractured spraberry trend area. In *Society of Petroleum Engineers*. Paper SPE-35469-MS presented at Permian Basin Oil and Gas Recovery Conference, 27-29 March, Midland, Texas, https://doi.org/10.2118/35469-MS.

Schrauf, T. and Evans, D. (1986). Laboratory studies of gas flow through a single natural fracture. *Water Resources Research*, 22(7):1038–1050.

Sheng, J. (2010). *Modern chemical enhanced oil recovery: theory and practice*. Gulf Professional Publishing.

Sheng, J. J. (2015). Enhanced oil recovery in shale reservoirs by gas injection. *Journal of Natural Gas Science and Engineering*, 22:252–259.

Skoreyko, F. A., Villavicencio, A. P., Rodriguez Prada, H., and Nguyen, Q. P. (2011). Development of a new foam eor model from laboratory and field data of the naturally

fractured cantarell field. In *Society of Petroleum Engineers*. Paper SPE-145718-MS presented at SPE Reservoir Characterisation and Simulation Conference and Exhibition, 9-11 October, Abu Dhabi, UAE, https://doi.org/10.2118/145718-MS.

Skoreyko, F. A., Villavicencio, A. P., Rodriguez Prada, H., and Nguyen, Q. P. (2012). Understanding foam flow with a new foam eor model developed from laboratory and field data of the naturally fractured cantarell field. In *Society of Petroleum Engineers*. Paper SPE-153942-MS presented at SPE Improved Oil Recovery Symposium, 14-18 April, Oklahoma, USA, https://doi.org/10.2118/153942-MS.

Steinsbø, M., Brattekås, B., Ersland, G., Bø, K., Opdal, I., Tunli, R., Graue, A., and Fernø, M. (2015). Foam as mobility control for integrated co2-eor in fractured carbonates. In *IOR 2015-18th European Symposium on Improved Oil Recovery*. EAGE.

Svorstol, I., Blaker, T., Arneson, S., Holt, T., Vassenden, F., and Surguchev, L. (1995a). Foam pilot evaluations for the snorre field, part 1: Project and laboratory results. In *IOR 1995-8th European Symposium on Improved Oil Recovery*.

Svorstol, I., Blaker, T., Arneson, S., Holt, T., Vassenden, F., and Surguchev, L. (1995b). Foam pilot evaluations for the snorre field, part 2: Numerical simulations and economical evaluations. In *IOR 1995-8th European Symposium on Improved Oil Recovery*.

Szafranski, R., Lawson, J., Hirasaki, G., Miller, C., Akiya, N., King, S., Jackson, R., Meinardus, H., and Londergan, J. (1998). Surfactant/foam process for improved efficiency of aquifer remediation. *Structure, Dynamics and Properties of Disperse Colloidal Systems*, 111:162–167.

Taber, J. J. (1981). Research on enhanced oil recovery: past, present and future. *Surface phenomena in enhanced oil recovery*, pages 13–52.

Tiwari, S. and Kumar, M. S. (2001). Nitrogen injection for simultaneous exploitation of gas cap. In *Society of Petroleum Engineers*. Paper SPE-68169-MS presented at SPE Middle East Oil Show, 17-20 March, Manama, Bahrain, https://doi.org/10.2118/68169-MS.

Tsang, Y. (1984). The effect of tortuosity on fluid flow through a single fracture. *Water Resources Research*, 20(9):1209–1215.

Tsang, Y. (1992). Usage of "equivalent apertures" for rock fractures as derived from hydraulic and tracer tests. *Water Resources Research*, 28(5):1451–1455.

Turta, A. T. and Singhal, A. K. (2002). Field foam applications in enhanced oil recovery projects: screening and design aspects. *Journal of Canadian Petroleum Technology*, 41(10).

van Golf-Racht, T. D. (1982). *Fundamentals of fractured reservoir engineering*, volume 12. Elsevier.

Wang, J. and Narasimhan, T. N. (1985). Hydrologic mechanisms governing fluid flow in a partially saturated, fractured, porous medium. *Water Resources Research*, 21(12):1861–1874.

Witherspoon, P. A., Wang, J. S., Iwai, K., and Gale, J. E. (1980). Validity of cubic law for fluid flow in a deformable rock fracture. *Water resources research*, 16(6):1016–1024.

Wu, Y.-S. (2015). *Multiphase Fluid Flow in Porous and Fractured Reservoirs*. Gulf Professional Publishing, Waltham, MA, USA.

Yan, W., Miller, C. A., and Hirasaki, G. J. (2006). Foam sweep in fractures for enhanced oil recovery. *Colloids and Surfaces A: Physicochemical and Engineering Aspects*, 282:348–359.

Yeganeh, M., Hegner, J., Lewandowski, E., Mohan, A., Lake, L. W., Cherney, D., Jusufi, A., and Jaishankar, A. (2016). Capillary desaturation curve fundamentals. In *Society of Petroleum Engineers*. Paper SPE-179574-MS presented at SPE Improved Oil Recovery Conference, 11-13 April, Tulsa, Oklahoma, USA, https://doi.org/10.2118/179574-MS.

Zimmerman, R. W. and Bodvarsson, G. S. (1996). Hydraulic conductivity of rock fractures. *Transport in porous media*, 23(1):1–30.

LIST OF PUBLICATIONS

Journal Publications

1. **AlQuaimi, B. I.**, Rossen, W. R. (2017), *New capillary number definition for displacement of residual nonwetting phase in natural fractures.Geophys. Res. Lett.*, 44 (11), 5368–5373.

2. **AlQuaimi, B. I.**, Rossen, W. R. (2017), *Capillary Desaturation Curve for Residual Nonwetting Phase in Natural Fractures*. Accepted for publication in the *SPE Journal*.

3. **AlQuaimi, B. I.**, Rossen, W. R. (2017), *Study of foam generation and propagation in a fully characterized physical-model fracture*. Under review at the *Journal of Petroleum Science and Engineering*.

4. **AlQuaimi, B. I.**, Rossen, W. R. (2017), *Characterizing Foam Flow in Fractures for Enhanced Oil Recovery*. Under review at the *Journal of Petroleum Science and Engineering*.

5. **AlQuaimi, B. I.**, Rossen, W. R. (2017), *Foam Generation and Rheology in a Variety of Model Fractures*. Under review at the *Journal of Energy & Fuels*.

Conference Proceedings

1. **AlQuaimi, B. I.**, Rossen, W. R. (2017), *Study of foam generation and propagation in fully characterized physical-model fracture*. Proc. 9th International Conference on Porous Media & Annual Meeting, Rotterdam, The Netherlands..

2. **AlQuaimi, B. I.**, Rossen, W. R. (2017), *Characterizing Foam Flow in Fractures for Enhanced Oil Recovery*. Proc. EAGE IOR 2017-19th European Symposium on Improved Oil Recovery, Stavanger, Norway.

3. **AlQuaimi, B. I.**, Rossen, W. R. (2016), *Experimental Capillary Desaturation Curve for Residual Nonwetting Phase in Natural Fractures*. Proc. 8th International Conference on Porous Media & Annual Meeting, Cincinnati, Ohio, USA.

4. **AlQuaimi, B. I.**, Aminian, K., Ameri, S. (2011), *Interpretation of Well Test Data from Two Hydraulically Communicating Reservoirs*. Proc. SPE-160900-MS, SPE Saudi Arabia Section Technical Symposium and Exhibition, Al-Khobar, Saudi Arabia.

5. **AlQuaimi, B. I.**, Ansah, J., Al-Shehab, M. A., & Al-Ajmi, F. A. (2010), *Field-Wide Interference Test For Understanding The Hydraulic Communication Between Two Stacked Reservoirs*. Proc. OTC-20571-MS, Offshore Technology Conference, Houston, Texas, USA.

6. Ansah, J., Al-Shehab, M. A., Al-Bani, F. A., **AlQuaimi, B. I.**, & Jacob, S. (2009), *Two-Zone Commingled Production Using Intelligent Well Completion Coupled With ESP Through a Hydraulic Disconnect Tool*. Proc. SPE-120303-MS, SPE Middle East Oil and Gas Show and Conference, Manama, Bahrain.

SUMMARY

Naturally fractured reservoirs (NFRs) are found in many countries around the globe, in almost every lithology. These reservoirs can be carbonates, sandstones, or shale, in the case of unconventional or basement reservoirs. NFRs have been explored and exploited globally for groundwater, geothermal energy, hydrocarbon production, coalbed-methane production, and nuclear-waste sequestration. They have unique characteristics in their flow behavior. Short-circuiting is encountered in these reservoirs during fluid-displacement processes. This unfavourable behavior leads to considerable unrecovered hydrocarbons. Injection of gas into these reservoirs to enhance oil recovery without mobility control can greatly reduce the efficiency of the enhanced oil recovery process. Foam greatly reduces the mobility of gas in non-fractured porous media and improves sweep efficiency. However, the knowledge of foam in fractured porous media is far less complete [Chapter 1].

In this dissertation, we contribute to the knowledge of trapping and mobilization and of foam flow in fractures. We study the mobilization of the nonwetting phase in fractures. Our goal is to understand the desaturation process in fractures and whether or not the conventional capillary number is suitable to describe the process. We propose a new definition of capillary number for fractures defined based on a force balance on a trapped ganglion in a fracture. We identify three geometric parameters to describe features governing mobilization. Five distinctive model fractures made of roughened glass plates are used to test the new capillary number. We conduct desaturation experiments to quantify the relationship between the mobilization of ganglia and pressure gradient. We find that the new definition of capillary number shows its suitability to describe the mobilization of the trapped nonwetting phase in fractures [Chapter 2].

We study foam generation and mobilization in a 40×10 cm model fracture, since these processes are crucial for the success of foam-injection processes. In this model fracture, foam is generated mainly by capillary snap-off: fracture-wall roughness plays a major role in foam generation. In most cases, bubbles smaller than the pores are generated and propagate through the fracture. This depends in part on the geometry of the pore throats. Slit-shaped throats can give bubbles that are smaller than pore bodies. Snap-off is less dominant at a high fractional flow of gas (f_g). Lamella division is observed at high f_g at two different total superficial velocities. The size of the bubbles is not always similar to the size of the pore, as is thought to be true in 3D porous media, because bubbles reside in the apparatus for a time that is much shorter than that required for diffusion to eliminate small bubbles. Diffusion eliminates small bubbles in our model fracture much more slowly than in non-fractured 3D porous media. We find that pressure gradient correlates inversely with the average size of the bubbles [Chapter 3].

We also study foam rheology by varying superficial velocities of gas and surfactant solution. We carry out this part of the study using both horizontal and vertical flow to investigate the gravity effect. We find in our model fracture the same two foam flow regimes central to the understanding of foam in 3D porous media: a low-quality regime where pressure gradient is independent of the liquid velocity and a high-quality regime where the pressure gradient is independent of the gas velocity. Direct observation of the bubble size, bubble trapping and mobilization, and foam stability as functions of superficial velocities allows comparison with our understanding of the mechanisms behind the two flow regimes in 3D porous media. Additionally, foam is shear-thins in both regimes. But in other important respects the mechanisms thought to be behind the two flow regimes in 3D media do not appear in our model fracture. Foam is not at the limit of stability in the high-quality regime. Mobility in the high-quality regime instead reflects reduced and fluctuating foam generation at high foam quality. We observe gas slugs due to fluctuating foam generation followed by fine-textured foam. The time elapsed between the gas slugs and the size of the slugs depends on both the gas fractional flow and total superficial velocity u_t. The pressure-gradient data correlate well with the propagation of gas slugs downstream and hence confirms this finding of fluctuating foam generation at a high fractional flow of gas. Finally, for this model fracture the investigation of vertical flow shows the same findings as with horizontal flow, with a lower pressure gradient [Chapter 4].

We investigate foam-generation mechanisms in five fully characterized model fractures with different apertures and correlation lengths of the aperture distribution. Fractures encountered in the field differ in their aperture, roughness scale, correlation length of the roughness, etc. We also study the rheology of the in-situ-generated foam by varying the superficial velocities of the gas and surfactant solution. We compare the measured pressure gradient against the fracture attributes, aperture and the correlation length of the aperture. We also compare foam texture as a function of position within the fracture as the generated foam propagates through the fracture. We find that gas mobility is considerably reduced as a result of in-situ foam generation in our model fractures. Foam is generated predominantly by capillary snap-off and lamella division. Two of the five fracture samples show only lamella division, because the throat geometry is less favourable for snap-off. The other three samples show both snap-off and lamella division at different f_g and u_t. Very small pressure gradients, with oscillations, are recorded for the samples with very large apertures. In these cases no foam-quality scans could be conducted. The measured mobility reduction depends on the fracture attributes. Fracture-wall roughness, represented by both the hydraulic aperture and the correlation length of the aperture, plays an important role in foam generation and mobility. Two model fractures show the same two foam-flow regimes central to the understanding of foam in non-fractured porous media. When the roughness scale is fixed, a significant reduction in pressure gradient is measured together with increasing hydraulic aperture. Foam bubbles become larger as the aperture increases [Chapter 5].

SAMENVATTING

Natuurlijk gebarsten reservoirs (NGRs) zijn aanwezig in vele landen over de hele wereld, in bij elke lithologie. De reservoirs kunnen carbonaten, zandstenen of schalie zijn in het geval van niet-conventionele of sokkel (Engels: basement) reservoirs. NGRs worden geëxploreerd en geëxploiteerd wereldwijd voor grondwater, aardwarmte, koolwaterstoffen productie, methaanextractie van kolenlagen, en nucleair-afval opslag. Ze hebben unieke karakteristieken in hun doorstromingen eigenschappen. Kortsluiting wordt aangetroffen in deze reservoir tijdens vloeistof verplaatsing processen. Dit ongunstig gedrag leidt tot significant volume aan achtergebleven koolwaterstoffen. Injectie van gas in deze reservoirs als verbeterde oliewinningsmethode (Engels: Enhanced Oil Recoverable (EOR)) zonder mobiliteitscontrole kan leiden tot groot verlies in efficiency van EOR processen. Schuim verlaagt de mobiliteit van gas in ongebarsten poreus media en verbetert de "sweep" efficiëntie. Echter, de kennis van schuim in gebarsten poreus media is veel minder compleet [hoofdstuk 1].

In dit proefschrift, dragen wij bij aan de kennis over insluiten, mobilisatie, en schuim stroming in barsten. Wij bestuderen de mobilisatie van niet-bevochtende fase (Engels: non-wetting phase) in barsten. Ons doel is om de de-saturatie processen te begrijpen in barsten en of het conventioneel capillair getal passend is om het proces te beschrijven. Wij stellen voor om een nieuwe definitie van het capillair getal in barsten te definiëren, gebaseerd op de krachten balans van ingesloten ganglia in barsten. We identificeren die geometrische parameters om de aspecten te beschrijven die mobilisatie regeren. Vijf karakteristieke model-barsten gemaakt van ruwe glazen platen zijn gebruikt om het nieuwe capillaire nummer te testen. We voeren de-saturatie experimenten uit om de relatie tussen mobilisatie van ganglia en drukgradiënt te kwantificeren. Wij hebben gevonden dat de nieuwe definitie van capillaire nummer geschikt is om mobilisatie van ingesloten niet-bevochtende fase in barsten te beschrijven [hoofdstuk 2].

Wij bestuderen schuim generatie en mobilisatie in een 40×10-cm model-barst, aangezien deze processen cruciaal zijn voor het succes van schuim-injectie processen. In de model-barst vindt schuim generatie vooral plaats door capillaire afknapping: barst-muur grofheid speelt een belangrijke rol in schuim generatie. In de meeste gevallen, worden belletjes kleiner dan de poriën gegenereerd en plaatsen zich voort door de barst. Dit hangt voor een gedeelte af van de geometrie van de porie hals. Spleetvormige halzen kunnen belletjes genereren die kleiner zijn dan de porie lichamen. Afknapping is minder dominant bij hoge fractionele stroming van gas (f_g). Lamellen divisie is geobserveerd bij hoge f_g bij twee verschillende totale werkzame snelheden. Het formaat van de belletjes is niet altijd vergelijkbaar met het formaat van de porie, zoals wordt verondersteld in 3D poreuze media. Dit komt doordat de belletjes in dit toestel aanwezig zijn voor een veel kortere tijd dan nodig is om kleine belletjes te verwijderen aan de hand van diffusie. In ons model-

barst verwijdert diffusie kleine belletjes veel langzamer dan in ongebarsten 3D poreus media. Wij hebben gevonden dat de drukgradiënt invers gecorreleerd is met de gemiddelde belletje grootte [hoofdstuk 3].

Wij bestuderen ook schuim reologie bij verschillende werkende snelheden van gas en oppervlakte-actieve stoffen (Engels: surfactants) oplossingen. Wij voeren deze studie uit aan de hand van horizontale en bij verticale stroming om de zwaartekracht effect te bestuderen. Wij vinden in ons model-barst de zelfde twee schuim-stroming regimes, hetgeen wat centraal staat in ons begrip van schuim in 3D poreus media: lage kwaliteit regime waar drukgradiënt onafhankelijk is van vloeistof snelheid en hoge kwaliteit regime waar de drukgradiënt onafhankelijk is van de gas snelheid. Directe waarneming van de bubbel grootte, bubbel insluiting en mobilisatie, en schuim stabiliteit als een functie van werkende snelheden stelt ons in staat om een vergelijking te maken met onze opvatting van de mechanisme achter de twee stromingsregimes in 3D poreus media. Bovendien, schuim is afschuif-verdunnend in beide regimes. Maar in andere belangrijke opzichten zijn de mechanismen waarvan verondersteld wordt dat ze achter de twee stroming regimes in 3D media zijn, niet aanwezig zijn ons model-barst. Schuim is niet op het limiet van stabiliteit in de hoge-kwaliteit regime. Echter, mobiliteit in de hoge-kwaliteit regime reflecteert de verminderde en fluctuerende schuim generatie. Wij observeren gas slugs vanwege de fluctuerend schuim generatie, gevolgd door schuim met een fijn textuur. De tijd tussen de gas slugs en het formaat van de slugs hangt af van de gas fractionele stroming en de totale werkende snelheid ut. De drukgradiënt data correleert goed met de propagatie van gas slugs stroomafwaarts en bevestigt daarmee de vinding dat fluctuerende schuim generatie bij hoge fractionele stroming van gas. Ten slotte, onderzoek van verticale stroming door de model-barst toont de zelfde vindingen als met horizontale stroming, met lagere drukgradiënt [hoofdstuk 4].

Wij onderzoeken schuim generatie mechanismen in vijf karakteristieke model-barsten met verschillende openingen en correlatie lengtes van de opening distributie. Barsten waargenomen in het veld verschillen in hun opening, grofheid, correlatie lengte van de grofheid, etc. Wij bestuderen ook de reologie van de in-situ gegenereerde schuim door de werkende snelheden van het gas en surfactant oplossing te variëren. Wij vergelijken de waargenomen drukgradiënt met de barst eigenschappen, opening en correlatie lengtes van de opening. Wij vergelijken ook de schuim textuur als een functie van positie binnen de barst wanneer de gegeneerde schuim zich voortbeweegt door de barst. Wij observeren dat gas mobiliteit aanzienlijk wordt verlaagd door in-situ schuim generatie in ons model-barsten. Schuim is vooral gegenereerd door capillaire afknapping en lamellen divisie. Twee van de vijf barst monsters vertonen alleen lamellen divisie, omdat de porie hals geometrie minder gunstig is voor afknapping. De andere drie monsters vertonen afknapping alsmede lamellen divisie bij verschillende f_g en u_t. Ontzettend lage drukgradiënten, met oscillaties, zijn waargenomen bij de monsters met ontzettend grote openingen. In deze gevallen kon geen schuim-kwaliteit scans (Engels: foam-quality scans) worden uitgevoerd. De waargenomen mobiliteit reducties hangen af van de barst eigenschappen. Barst-muur grofheid, vertegenwoordigd door hydraulische opening en de correlatie lengtes van de opening spelen een belangrijke rol in schuim generatie en

mobiliteit. Twee model-barsten tonen de zelfde twee schuim-stroming regimes, hetgeen dat centraal staat in ons opvatting van schuim in ongebarsten poreus media. Wanneer de grofheid schaal constant wordt gehouden, wordt een significante verlaging van de drukgradiënt waargenomen met grotere hydraulische opening. Schuim belletjes worden groter met grotere opening [hoofdstuk 5].

ACKNOWLEDGEMENTS

First, I thank my God for giving me all the necessary strength to accomplish the many things that I have completed in life.

This dissertation is mainly sponsored by Saudi Aramco, which generously provided me with a full scholarship to pursue my PhD studies at Delft University of Technology. I would like to thank all Saudi Aramco's individuals who had trust in me and took part in making this scholarship happens. I would particularly like to express my sincere thanks to Fahad A. AlAjmi, for his encouragement to me to perform my PhD research. I would also like to sincerely thank the generous support from the joint industry project on foam for enhanced oil recovery at Delft University of Technology, for the additional funds to acquire extra laboratory equipment to conduct more experiments.

I feel very honoured and privileged to have an advisor such as Prof. Bill Rossen. I have been fortunate to carry out my PhD research under his supervision. Throughout the course of this project, Prof. Rossen has taught me how to be an independent researcher and how to intelligently tackle research questions. Prof. Rossen managed to bring my motivation high again during the challenging times of the project. His pleasant personality made the working environment so fascinating. I have learned so much from you about technical writing and on how to respond to reviewers. Many thanks for the careful review and for your insights on this thesis. Prof. Rossen: please accept my deep gratitude and appreciation for all the things I learned from you during the past four years. I would like to thank you for your unwavering support, advice, guidance, patience and comments.

I am also thankful to the examination committee members: Martin Ferno, Denis Voskov, Auke Barnhoorn, Henri Bertin, Giovanni Bertotti and Pacelli Zitha for participating in my PhD defense, carefully reviewing my work and providing valuable comments.

Special thanks and appreciation go to Janice Rossen for her encouragement and constructive feedback . I am so pleased to have met you and constantly share my progress with you. I would like to thank you for your advice and heartfelt compassion when I arrived in The Netherlands. I am sincerely grateful to you for your ideas about finishing the dissertation and for the brainstorming session about the dissertation cover. Thanks again for your kindness, your inspiring emails and your outstanding organization of the group dinners. I am honored to have a life-long friendship with your family.

I am sincerely grateful to Sian Jones, "The Bubbles Queen" as we like to call you, for so many things I leaned from you about foam experiments. You have been really so supportive and helpful to all the PhD students. We were unhappy to see you leaving Delft,

but we are confident that you will have a successful career at DTU. I learned from you tricks about image analysis, laboratory equipment, and experimental pitfalls. I would like to thank you for the discussions that I had with you about my experimental results and about my manuscript.

None of the experimental work conducted during my PhD would have been possible without the excellent and continuous support from the lab technicians. I would especially like to thank Marc Friebel “my brother from another mother”, as you like to call me. Marc helped so much to build my experimental setup and came up with many wonderful ideas and things to try in the laboratory. I owe you thanks and appreciation for your assistance, friendship and kindness.

Special thanks and appreciation go to Aramco Overseas Company (AOC) for their support throughout my stay in the Netherlands. I would particularly like to thank Mr. Fahad AbdulKareem for extending a warm welcome to the students in the Netherlands and for engaging the students in the company’s social activities. I also thank Mrs. Aggie Cooper, my career advisor from AOC, for her pleasant personality and prompt assistance. Aggie: you have been so instrumental and professional in dealing with my requests. There have been some occasions where I needed immediate help and you have been always there to help.

My sincere thanks and deep appreciation go Abdulaziz AlBugrishi (my brother-in-law) for his assistance during these four years and for being my legal representative in Saudi Arabia. You have been so helpful to me and I relied on you to finish many things. Abu Saleh: you have made me so relieved that I have someone home to finish stuff that required my presence. You are more than a brother and I thank you again for your eagerness to help me.

I want to candidly thank all my friends and colleagues in the petroleum engineering section. Many friends have helped me a lot to enjoy my stay in Delft. I greatly value their friendship and I deeply appreciate their assistance. First, I would like to thank Siavash Kahrobaei for his endless assistance. Siavash: you have helped me a lot with MatLab® and Latex. It was the first time I used Latex and you made it really easy for me to finish my dissertation. I am glad that I met you in Delft and it is an honour for me to become your friend. I would also like to thank Eduardo De Barros for the tips on MatLab® and for your pleasant personality. I am thankful to Nikita for the unique attitude and special personality. Nikita: I would like to thank you for your friendship and your kindness. Special thanks go to “mi hermano” as I like to call you Rafael. Thank you for your nice personality and your caring attitude. Many thanks and appreciation go to Ahmed Hussain for helping me out during my first visit to Delft in 2013 and for frequent help in translating some Dutch letters. My thanks also go to Mark, Rodrigo, Jiakun , Jinyu, Durgesh, Matei, Mojtaba, Martijn, Swej, Negar, Roozbeh, Amin Fatemi, Jakolien, Mohsen, Longlong, Brandon, Yang and Matteo.

I would also like to thank my Saudi friends in Delft. I truly enjoyed your company and

I am fortunate to have met you. My thanks go to Abdulrahman Alshuhail, Sulaiman AlJedaie, Raid AlSaadan Ahmad AlAyesh, Ali AlFaraj, Ahmad Alwoshel, Naif Alghamdi, Hussain AlHammad, Fahad Alsayyari, Abdulaziz AlMutawa, Abdullah Alattas, Abdullah Baubaid, Abdullah Aljuffri, Omar AlAbdulgader, Feras Alshehri, Majid Aljamed, Abdulmohsen Almansour, and Mohammed Almarzouq. Some of you have left Delft already and I wish all the best of luck to the ones who are still pursuing their degrees.

My deep appreciation also goes also to my Saudi friends who kept in touch with my during my studies. The friends who wished me all the best and kept asking about my return to Saudi Arabia. You kept me connected and your kindness has reached me while I was thousands of miles away. I would like to thank you for your friendship and your best wishes. The thanks go to, with no specific order, Bader AlMutairi, Naif AlRiyhan, Majed AlQuaimi, Mubarak AlJuwair, Waleed AlKathran, Abdulaleh AlAli, Abdullah AlHabah, Saud AlHoti, Hasan AlQahtani, Zayed Alrayyes and Amer Abuhasson.

I would also like to express my gratitude to my Mam for her most genuine love, compassion, kindness and sacrifice. I am so thankful to you and I do not think thanking you is sufficient for your life-long support. You have been supporting my studies since my primary school through to my PhD. I am so grateful to you and I hope one day I can make you proud of me. Special thanks go also to my Dad for all the things that he offered me in my life. My most heartfelt thanks go also to Amal, Bandary, Manal, Mashel, Hayat, Hanan, Asayel and Shahad for their love and for believing in me.

Last, but not least, my most heartfelt appreciation goes to my lovely wife Haya for her true love, sacrifice, support, understanding, encouragement, and helping me get through the tough and stressful times during my PhD study. I remember it was not easy for you to adapt to the new lifestyle when we first came to the Netherlands. However, you took the challenge and enjoyed being in The Netherlands thereafter. We learned a lot about the Dutch culture, we visited many places, and we experienced living in such a different climate than Saudi Arabia and the United States. We established beautiful feelings towards The Netherlands and the Dutch people. We engraved a lot of nice memories on our hearts which will last forever. I should also praise my daughter Bailasan for learning English at the British School and some Dutch. Bailasan learned so quickly and made a lot of friends from all over the world. This experience has broadened her horizon considerably and should make a positive impact on her personality. Bailasan: your good friends Lisa, Treasure, Sofia, Louis, Gracia, and Audry miss you so much and wish you luck. I am proud of you and I am confident you will make me even prouder in the future. We were also glad to have our son Ibrahim during the third year of my PhD. The experience went very well and we are grateful to all the people that supported us during that time.

Bander AlQuaimi
Delft
August, 2017

ABOUT THE AUTHOR

Bander AlQuaimi was born on October 26, 1979 in Riyadh, Saudi Arabia. He is a Saudi Aramco reservoir engineer on a special program to become a specialist in naturally fractured carbonate reservoir development and management. He is a certified petroleum engineering professional by the Society of Petroleum Engineers. Bander was a member of a task force to bring 1.2 Million b/d of Arab light crude to Aramco's portfolio. Bander is knowledgeable in developing new assets, and in addition he has expertise in designing production and injection strategies to maximize oil fields' ultimate recovery. Bander has worked in reservoir simulation, production engineering, reservoir characterization and modelling, and reservoir management. He was rcognized as an outstanding graduate student based on his academic achievements at West Virginia University. He was also recognized with excellence in action within Aramco's Exploration and Producing professionals. He was awarded two scholarships to pursue an MSc and PhD. Bander's PhD research invloves foam flow in fractures for enhanced oil recovery. He authored and coauthered several publications on naturally fractured reservoirs. Bander holds a BSc and MSc in petroleum engineering from King Saud University and West Virginia University, respectively.